

# Colloidal Crystallization under Confinement

Inaugural-Dissertation  
zur Erlangung des Doktorgrades  
der Mathematisch-Naturwissenschaftlichen Fakultät  
der Heinrich-Heine-Universität Düsseldorf

vorgelegt von  
**Erdal Celal Oğuz**  
aus Istanbul

Dezember 2012

Aus dem Institut für Theoretische Physik II: Weiche Materie  
der Heinrich-Heine-Universität Düsseldorf.

Gedruckt mit der Genehmigung  
der Mathematisch-Naturwissenschaftlichen Fakultät  
der Heinrich-Heine-Universität Düsseldorf

Referent: Prof. Dr. Hartmut Löwen  
Koreferent: Prof. Dr. René Messina

Tag der mündlichen Prüfung: 25.01.2013

©Erdal Celal Oğuz 2012  
All Rights Reserved.

The author has enjoyed fruitful collaborations with other scientist during his PhD thesis. The work described in this thesis has been published in a number of peer-reviewed papers, which constitute the following self-contained chapters:

- **Chapter 1:** E. C. Oğuz, R. Messina, H. Löwen, *Helicity in cylindrically confined Yukawa systems*, Europhys. Lett. **94**, (2011) 164511
- **Chapter 2:** A. Reinmüller, E. C. Oğuz, R. Messina, H. Löwen, H. J. Schöpe, T. Palberg, *Colloidal crystallization in the quasi-two-dimensional induced by electrolyte gradients*, J. Chem. Phys. **136**, (2012) 164505

This chapter contains experiments as well as Brownian Dynamics computer simulations. Experiments represented in this chapter have been performed by A. Reinmüller, H. J. Schöpe, and T. Palberg. The author gratefully acknowledges their contributions to this publication. This project has been mainly coordinated by A. Reinmüller.

- **Chapter 3:** E. C. Oğuz, R. Messina, H. Löwen, *Multilayered crystals of macroions under slit-confinement*, J. Phys.: Condens. Matter **21**, (2009) 424110

This chapter have been partly investigated during the diploma studies of the author. Some parts are contained in the diploma thesis of the author at the University of Düsseldorf.

- **Chapter 4:** E. C. Oğuz, A. Reinmüller, H. J. Schöpe, T. Palberg, R. Messina, H. Löwen, *Crystalline multilayers of charged colloids in soft confinement: experiment vs. theory*, J. Phys.: Condens. Matter **24**, (2012) 464123

This chapter contains experiments as well as lattice sum calculations. Experiments represented in this chapter have been performed by A. Reinmüller, H. J. Schöpe, and T. Palberg. The author gratefully acknowledges their contributions to this publication. This project has been mainly coordinated by the author of this thesis.

- **Chapter 5:** E. C. Oğuz, M. Marechal, F. Ramiro-Manzano, I. Rodriguez, R. Messina, F. J. Meseguer, H. Löwen, *Packing confined hard spheres denser with adaptive prism phases*, Phys. Rev. Lett. **109**, (2012) 218301

This chapter contains experiments, Monte Carlo computer simulations as well as theoretical approaches. Experiments represented in this chapter have been performed by F. Ramiro-Manzano, I. Rodriguez, and F. J. Meseguer. Monte Carlo simulations have been performed by M. Marechal. The author gratefully acknowledges their contributions to this publication. This project has been mainly coordinated by the author of this thesis.

The author was also involved in the following publications, which are not part of this thesis:

- E. C. Oğuz, R. Messina, H. Löwen, *Crystalline multilayers of the confined Yukawa system*, Europhys. Lett. **86**, (2009) 28002
- H. Löwen, E. C. Oğuz, L. Assoud, R. Messina, *Colloidal crystallization between two and three dimensions*, Adv. Chem. Phys. **148**, (2012) 225
- I. Williams, E. C. Oğuz, P. Bartlett, H. Löwen, C. P. Royall, *Direct measurements of the osmotic pressure in quasi-hard-discs under adaptive confinement*, in preparation
- E. C. Oğuz, J. Bewerunge, S. Egelhaaf, R. Messina, H. Löwen, *Gravity mediated multilayering*, in preparation
- E. C. Oğuz, W. Nosenko, A. V. Ivlev, G. E. Morfill, R. Messina, H. Löwen, *Buckling instabilities in dusty plasmas*, in preparation



---

## Summary

This thesis at hand deals with crystalline phases of colloidal particles under confinement. In particular, we mainly investigate the equilibrium structures of confined colloidal crystals, and present recently obtained results in five self-contained chapters. These five chapters, and thus the thesis, can be divided into three parts, each characterized by the type of the confinement.

In the first part, containing the Chapter 1, we applied a hard cylindrical confinement to a model system of point-like particles interacting via a Yukawa pair potential. We investigate the ground state stability phase diagram of the crystalline Yukawa system by using lattice sum minimizations. The cylindrical confinement displays the origin of the quasi-one-dimensionality; By continuously increasing the cylinder radius from zero to a finite value, we open the way to an intermediate regime between one and three dimensions. In this regime, we obtain chiral and achiral helical structures, which help a lot to understand the nature of e.g., biomolecules such as DNA.

In the second part (Chapter 2), we combine real-space experiments (by Reinmüller *et al*) and Brownian Dynamics computer simulations in order to study the driven crystallization of charged particles in two-dimensional flow fields in aqueous solvents. These flow fields occur due to electrolyte gradients caused by cation exchange resin fragments. Colloidal macroparticles follow the flow. Consequently, the crystallization takes place at these fragments, acting as seed particles. Regarding the experimental situation, the point-like Yukawa particles in simulations are exposed to an attractive, long-ranged circular trapping potential to mimic the solvent flow. Good agreement is achieved between experiments and simulations. As a result, we obtain mono- and polydomain crystals with corresponding grain boundaries, depending on the shape of the seed.

The third part of this thesis comprises the Chapters 3,4, and 5. Here, the confinement is given by a hard slit, i.e., two parallelly aligned hard flat walls. This special confinement gives rise to a quasi-two-dimensional system, which interpolates between two and three dimensions. Three different pair interactions are considered in three different chapters, all involving the quasi-two-dimensionality: In Chapter 3, we investigate the zero-temperature crystalline phase diagram of unscreened Coulomb particles embedded in a parabolic soft potential (in addition to the hard slit). By energetic considerations using lattice sum minimization methods, we figure out stable mono-, bi-, and multilayers. In Chapter 4, we analyze crystalline multilayers of charged colloids confined between two glass plates. Here, we combine experiments (by Reinmüller *et al*) and lattice sum minimizations. Charged colloids are modelled with a Yukawa potential, whereas the wall-particle repulsion is assumed to be of hyperbolic cosine form in accordance to the linear screening theory. We obtain complex phases (e.g., the vertically aligned triangular layers  $hcp_{\perp}$  equivalent to  $hcp(110)$ ), which are not present in three-dimensional bulk. Chapter 5 addresses the packing problem of confined hard spheres. By combining experiments (by Ramiro-Manzano *et al*), Monte Carlo computer simulations (by Marechal), and

theory (using a recently reported penalty method), we investigate the dense packed crystalline structures in a hard slit. We achieve an excellent agreement between the three approaches, and recover the novel adaptive phases, which brings new opportunities and insights into the field of the packing problems.

---

## Zusammenfassung

Die vorliegende Arbeit beschäftigt sich mit kristallinen Phasen kolloidaler Teilchen unter eingeschränkten Geometrien sowie in externen Feldern. Wir präsentieren unsere kürzlich erlangene Resultate in fünf in sich abgeschlossenen Kapiteln. Diese Arbeit besteht aus drei Teilen, in denen sich die fünf Kapitel wiederfinden.

Im ersten Teil dieser Arbeit (Kapitel 1) untersuchen wir ein in einem harten zylindrischen Behälter eingeschlossenes, aus Punktteilchen bestehendes Modellsystem. Die Teilchen wechselwirken sich untereinander mit einem Yukawa-Potential. Die zylindrische Einschränkung ermöglicht dem System, kontinuierlich von einer Dimension in drei Dimensionen zu übergehen. Dieses "Zwischenregime" wird in dieser Arbeit als quasi-eindimensionales System bezeichnet. Desweiteren stellen wir das Phasendiagramm der kristallinen Yukawa-Teilchen im Grundzustand auf. Zu diesem Zweck minimieren wir numerisch die vorhandenen Gittersummen, und erhalten als resultierende Strukturen chirale sowie achirale Helices.

Der zweite Teil der vorliegenden Arbeit (Kapitel 2) handelt von getriebener Kristallisation geladener Teilchen in zweidimensionalen Flussfeldern. Die physikalische Fragestellung dieses Kapitels wird anhand von Kolloidexperimenten (durchgeführt von Reinmüller *et al*) sowie Brownscher Dynamik Simulationen untersucht. Fragmente des Kationenaustauschers in wässrigen Lösungen verursachen Elektrolytgradienten in ihrer unmittelbaren Umgebung, so dass sich ein radiales und nach innen gerichtetes Flussfeld einsetzt, welches die Kolloide mitzieht. Diese Fragmente dienen als Kristallisationskeime. Denn aufgrund der erhöhten Kolloiddichte an diesen Keimen findet anschliessend die Kristallisation statt. In Computersimulationen analysieren wir diese Effekte, indem wir die o.g. Flussfelder durch ein anziehendes und langreichweitiges externes Potential modellieren. Unsere beider Ergebnisse zeigen deutliche Übereinstimmung: abhängig von der Form des Keims entstehen Polykristalle mit zugehörigen Korngrenzen sowie auch Einkristalle.

Im dritten und letzten Teil der Arbeit, bestehend aus Kapiteln 3,4, und 5, untersuchen wir eine harte Schlitzgeometrie. Diese besteht aus zwei harten, zueinander parallel ausgerichteten, ebenen Wänden. Diese spezielle Einschränkung führt zu einem quasi-zweidimensionalen System, welches den kontinuierlichen Übergang von zwei zu drei Dimensionen ermöglicht, und vice versa. In dieser speziellen Geometrie erforschen wir das Phasenverhalten dreier Teilchensorten, die sich hauptsächlich in Paarwechselwirkungspotentialen unterscheiden: im Kapitel 3 werden sich im Schlitz befindliche unabgeschirmte Coulomb-Teilchen (z.B. Elektronen) zusätzlich einem parabolischen Potentialfeld ausgesetzt. Anhand Gittersummenberechnungen im Grundzustand erhalten wir strukturelle Informationen über die stabilen Kristalle. Im Kapitel 4 untersuchen wir kristalline Multilagen geladener Kolloide zwischen zwei Glasplatten. Dieses Projekt besteht aus Experimenten (durchgeführt von Reinmüller *et al*) und theoretischen Gittersummenberechnungen. Im theoretischen Modell wird die Teilchen-Teilchen-Wechselwirkung mit einer Yukawa-Abstoßung beschrieben. Gemäß der linearen Abschirmungstheorie kann die durch die Ladung der Wände verursachte Wand-Teilchen-Wechselwirkung innerhalb der Wände mit

einer effektiven Abstoßung beschrieben werden, die eine Kosinus-Hyperbolicus-Form annimmt. Wir erzielen gute Übereinstimmung, und erhalten komplexe Phasen wie z.B. die  $\text{hcp}\perp$  Phase (diese Struktur entspricht der 110-Schnittebene des hcp-Gitters), die in drei dimensional Systemen so nicht existieren. Im Kapitel 5 handelt es von der dichtesten Packung harter Kugeln in der Schlitzgeometrie. Wir kombinieren Kolloidexperiment (durchgeführt von Ramiro-Manzano *et al*), Monte Carlo Computersimulationen (durchgeführt von Marechal), und Theorie, um die dichtest gepackte kristalline Strukturen zu studieren. In all den drei unterschiedlichen Vorgehensweisen entdecken wir gemeinsam neue sog. adaptive Phasen, die Herangehens- bzw. Betrachtungsweisen an die Packungsproblematik revolutionieren könnten.

---

## Acknowledgments

It is probably the most complicated part of this thesis. Not only because of the vast number of people, who I would like to thank, also, because this part represents the end of a certain life period. I spend many years in this lab, which I enjoyed so much. I would like to thank heartily all the people, who made my time here very pleasant.

Specially, I am very grateful to have Hartmut Löwen and Réne Messina as my 'teachers' and advisors. I've learnt so many things in the last years from you. It is incredible for me to imagine that the time I came to the lab, and now, reveals such huge differences with respect to my scientific skills. Also on a personal level, I've always enjoyed your presence. It was an honor for me to be in this lab. Thank you for all discussions, comments, ideas, etc, which all contributed to the success of this work. It was and still is a great pleasure for me!

I would like to express my thanks to all members of the lab. There is no need to say that I deeply enjoyed the stay here with all of you. To be honest, you (incl. the former members I knew) are the best group I've ever seen in a scientific community. You made the atmosphere in the lab very lovely. And you've been always ready to help. For all the help I needed for non-scientific stuff, I thank you very much Jo and Brigitte. It was a pleasure to know you. I owe very special thanks to my good friends Aleks, Andreas (der Erste), and Lahcen, not only due to endless constructive discussions and comments on a scientific level, also because of your friendship, which will definitely hold a lifetime. Dear Tobi, I really enjoyed your presence in the office, although our working times were a bit different. I further thank to Michael, Matthieu and Cristian for very fruitful discussions. Also, I would like to express my special thanks to Michael, Cristian, Tobi, and Aleks for careful reading of parts of this thesis, and all the others, who I cannot name here, for my pleasant stay in the lab.

I was in a fortunate position to join numerous collaborations with scientist from other universities and institutions. I enjoyed every discussion, and every common work. I would like to express my thanks to Alexander, HaJo, Thomas, Alexei, Fernando, Ian, Paddy, Jörg and others.

I also acknowledge the financial support from SFB TR6, and ERC, which made this work possible.

Finally, I want to thank my family for all of their endless support in good times as in bad. *Sevgili ailem; Kısa ve öz söylemek gerekirse, verdiğiniz her türlü destek için sonsuz teşekkürlerimi sunarım.*



# Contents

Summary	vii
Zusammenfassung	ix
Acknowledgments	xi
Introduction	1
<b>1 Helicity in cylindrically confined Yukawa systems</b>	<b>7</b>
<b>2 Colloidal crystallization in 2D induced by electrolyte gradients</b>	<b>17</b>
2.1 Introduction . . . . .	17
2.2 Experimental section . . . . .	19
2.2.1 Experiment . . . . .	19
2.2.2 Analysis of crystal growth . . . . .	22
2.3 Simulations . . . . .	24
2.4 Discussion . . . . .	27
2.4.1 Crystal growth . . . . .	27
2.4.2 Gradient-induced particle transport . . . . .	28
2.5 Conclusion . . . . .	32
<b>3 Multilayered crystals of macroions under slit-confinement</b>	<b>35</b>
3.1 Introduction . . . . .	35
3.2 The Model . . . . .	37
3.3 Mono- and bilayer phase behavior . . . . .	39
3.3.1 Phase diagram . . . . .	39
3.3.2 From monolayer to trilayer - An analytic approach . . . . .	41
3.4 Multilayers . . . . .	43
3.5 Conclusions . . . . .	46
<b>4 Crystalline multilayers of charged colloids in soft confinement: experiment vs. theory</b>	<b>47</b>
4.1 Introduction . . . . .	47
4.2 Experiments . . . . .	49

---

4.2.1	Principles . . . . .	49
4.2.2	Observations . . . . .	52
4.3	Theory . . . . .	55
4.3.1	The model . . . . .	55
4.3.2	Lattice Sum Minimization . . . . .	56
4.3.3	Matching the model parameters to the experiments . . . . .	56
4.3.4	Ground state phase diagrams and comparison to experiments .	57
4.4	Discussion . . . . .	59
4.5	Conclusions . . . . .	61
<b>5</b>	<b>Packing confined hard spheres denser with adaptive prism phases</b>	<b>63</b>
	<b>Appendix</b>	<b>73</b>
	<b>Bibliography</b>	<b>77</b>

# Introduction

At given conditions, matter in nature can be classified into phases like *gas*, *liquid*, and *solid*<sup>1</sup>, where throughout each phase, the essential properties of a material, e.g., density or refraction index, is homogeneous. This thesis at hand deals with the crystalline phase behavior of *confined colloidal* particles.

The title of this thesis may raise many questions about colloids, crystallization, and confinement. Each topic is individually addressed in the following.

Colloids are probably among the most prominent objects belonging to the Soft Condensed Matter (a subfield of the Condensed Matter physics), and have drawn a lot of attention in the last decades. By taking into account that Soft Matter contains a vast number of diverse systems such as (just to name only a few) polymers, gels, colloids, emulsions, proteins, and biomembranes, the enormous importance of this field becomes clear. Not only a wealth of everyday realizations like paint, ink, food, pharmaceuticals, etc. [1], can be counted to the strengths of this field, also the fact that Soft Matter stimulates fruitful interdisciplinary interactions between scientists from physics, chemistry, and biology.

The studies in this work are based on the concept of effective interactions, which represent an indispensable tool for understanding the nature of colloids. Colloidal suspensions comprise mesoscopic solid particles with typical sizes ranging from few nanometers to few tens of micrometers. Being suspended in a molecular fluid solvent [2], they undergo Brownian motion due to collisions with the solvent constituents. There are different time and length scales, which stem from the presence of microscopic and 'fast' solvent particles, on the one hand, and mesoscopic and 'slow' colloids, on the other hand. Therefore, a coarse graining is necessary to predict the macroscopic properties of colloidal suspensions from the microscopic interactions. As a consequence, effective interactions can be derived in order to bridge from microscopic to mesoscopic systems.

Crystals made up of colloids, termed shortly as *colloidal crystals*, appear in various forms in nature as in many suspensions of viruses (e.g., tobacco and Tipula viruses [3,4]) and in opals reflecting crystalline ordering [5]. Furthermore, they can be synthetically produced at a low-cost level, e.g., using silica [5], giving rise to numerous studies. Colloidal crystals possess physical properties different from 'nor-

---

<sup>1</sup>Please note that in addition to these classical states of matter, further ones also exist like e.g., *plasma*, *superconducting phase*, and *Bose-Einstein condensate*.

mal' crystals, whose repeating units are atoms or molecules. While the interaction energies between colloids are almost comparable to the ones in atomic systems, the mesoscopic length scale involved in colloidal crystals is much greater than typical atomic and molecular distances (i.e.,  $< \text{nm}$ ) and therefore leads to relatively low energy densities [6]. Consequently, colloidal crystals are supposed to be very *soft*, i.e., they feature relatively low elastic and/or shear moduli (up to ten to twelve orders of magnitude smaller than those known from atomic systems). Furthermore, colloidal crystals can diffract the visible light due to their mesoscopic size. Bragg reflections easily occur for the mean distances involved in colloidal crystals. For these reasons, colloidal crystals are widely used to study e.g., crystallization phenomena.

In this spirit, colloidal systems serve as excellent model systems for the study of physical problems such as crystallization. Given the fact that colloids are highly susceptible to external fields, their phase behavior can be controlled externally. Moreover, the interactions between colloids in aqueous suspension can be easily tuned such that, for example, sterically stabilized colloids (whose surfaces are polymer-coated) represent realization of a hard-sphere system [7], while charged stabilized colloids are mainly governed by a Yukawa-like pair interaction [8,9]. The latter displays an effective pair interaction based on the electrostatic repulsion in colloidal suspensions and is essentially given by the Derjaguin-Landau-Verwey-Overbeek (DLVO) pair interaction involving the linear Poisson-Boltzmann theory [10–12]. Importantly, individual colloidal particles can be comfortably visualized in space and time e.g., by video microscopy [13]. Hence, colloidal systems enables studies at a single-particle level by providing real-space access to e.g., crystallization phenomena in contrast to atomic systems.

Crystallization is a central topic of tremendous importance in the condensed matter physics offering giant possibilities for many applications [14]. Yet the fundamental understanding of crystallization represents still a challenge, numerous experiments, extensive computer simulations as well as theories helped a lot to obtain a deeper insight into the nature of crystallization in the last decades.

For numerous industrial applications such as semiconductors, sensors, optical elements, and nanomaterials, a quantitative understanding of non-equilibrium processes as crystal growth and nucleation is indispensable. Crystalline structures can be achieved through many technical methods like epitaxial growth, and chemical vapor deposition. An important step towards understanding the crystal growth from a metastable liquid is delivered by the classical nucleation theory [15] providing the homogeneous nucleation. Homogeneous nucleation involves the creation of a crystal nuclei of a critical minimum size in the liquid phase, which initiates the crystal formation. Heterogeneous nucleation — widely seen as the counter part of homogeneous nucleation — however, requires pre-existing seeds as e.g., impurities and walls to proceed the crystal nucleation at these positions. Although, both homogeneous and heterogeneous nucleation in colloidal suspensions are extensively studied in terms of experiments and computer simulations in recent decades, the crystallization process remains still a challenging task in the condensed matter physics: as scientists

delivered widely accepted theories for the freezing/melting in two-dimensional (**2D**) bulk, the nature of crystallization in three spatial dimensions (**3D**) is far from being completely understood.

The particular interest of this thesis concerns the static crystallization under confinement. Therefore, the concept of confinement should be clarified and its importance should be emphasized at this point: Geometrical restrictions to a system like slit-pores or slit-like cavities can be regarded, in general, as confinement. But also, energetic contributions from outside of the system — external potential fields — are subject to confinement. In nature, confined systems often appear. Well known examples are complex biological environments such as cells, which are confined by elastic membranes. Strictly speaking, every colloidal system must be confined as there always exists either natural boundaries or external fields such as gravity in real systems. In absence of an external potential, one speaks of confinement when the finite size effects play a not negligible role on the phase behavior.

The confinement affects the phase behavior in a way such that it can drastically differ from the bulk behavior [16,17]. More precisely, phase transitions such as crystallization can be strongly shifted in confining geometries [16]. A very prominent example is the confined water, whose freezing transition can be shifted below the natural freezing point in bulk [18,19]. Not only the structural, but also dynamical behavior of e.g., hard-sphere fluid is altered with respect to the bulk [20]. More generally, confinement may induce drastic changes in physical properties of a fluid such as viscosity, relaxation times, and flow profiles. Also non-equilibrium phenomena can be affected by the confinement: Recent computer simulations of hard-sphere systems indicate a speed up of the crystal growth in the presence of a flat wall [21]. In case of templated surfaces, the structure as well as the orientation can even be controlled, giving rise to tailored crystals.

The crystallization process under confinement as well as in bulk critically depends on the dimension of the system. Turning the attention to bulk systems, crystallization phenomena in different dimensions are briefly summarized in the following. In one dimension (**1D**), a crystalline phase does not exist at all for systems bearing fluctuations (i.e., for finite temperature  $T$ ). Even in 2D, long-wavelength fluctuations destroy the long-ranged translational order (see [22,23]) so that 2D crystals ( $T \neq 0$ ) can only exhibit quasi-long-ranged translational order. Strictly speaking, perfect positional order can only exist at zero temperature in 2D [24]. However, for 2D freezing and melting, important theories have been developed, whereas for 3D a comparable understanding of the underlying physical mechanisms for liquid-solid transition represents still a challenge. In case of 2D melting, a crystal-based theory (i.e., crystal  $\rightarrow$  liquid) has been developed by Kosterlitz, Thouless, Halperin, Nelson, and Young (KTHNY), see [25–27]. Experiments have been performed in order to confirm the predictions of this theory [28,29]. Furthermore, the liquid-based (i.e., liquid  $\rightarrow$  crystal) density functional theory, a mean-field approach from statistical physics, has been proven to be useful to study the freezing transition in 2D [30]. In all cases, two distinct phases, liquid and solid, need to be distinguished

from each other. Phenomenological criteria for freezing/melting have been made like the *Lindemann* criterion for melting [31] and the *Hansen-Verlet* criterion for freezing [32].

Due to the fact that hard spheres involve no energy scale, their bulk phase diagram is completely independent on  $T$ , but it is dictated by the volume fraction  $\phi$ . In this case, the crystallization is *entropy driven*. The reduction of the configurational entropy due to a crystal formation is overcompensated by an increase of the entropy due to a larger free volume in a crystal lattice. Therefore, a 3D hard-sphere system exhibits a first-order fluid-solid transition. It freezes at  $\phi_f \approx 0.54$  [2]. Beyond this freezing point, the face-centered-cubic (fcc) crystal becomes stable. Furthermore, the melting density is given as  $\phi_m \approx 0.49$ . Between  $\phi_m$  and  $\phi_f$ , the fluid and fcc crystal coexist. It is noteworthy that there is a natural upper limit of  $\phi$  as the hard spheres cannot overlap and, thus, the mutual densest packing of spheres is obtained at *packing* fraction  $\phi \approx 0.74$  in 3D.

In case of an effective Yukawa pair interaction, the inverse Debye screening length  $\kappa$  represents another control parameter. Hence, the stability phase diagram naturally becomes also a function of  $\kappa$ . For  $\kappa = 0$ , one recovers the *one-component plasma*, where the pair interactions are governed by the long-ranged Coulomb interactions. As a function of  $\kappa$ , the Yukawa system features three phases: liquid, fcc as well as body-centered cubic (bcc) crystals [33, 34] in 3D bulk.

In 2D, both hard *disks* and soft Yukawa particles exhibit fluid-crystal transitions into the triangular (hexagonal) lattice. For Wigner crystals (point-like electrons, with interact via unscreened Coulomb potential), the stable lattice in 2D is also the triangular one [35]. More structured interaction potentials involving at least two length scales can lead to more complex solids such as quasicrystals [36].

The particular interest of this thesis concerns the static crystallization under confinement. Here, two classes of confinement are provided: topographical confinement consisting of 'hard' geometrical containers (**HC**), and energetic confinement involving 'soft' external potential fields (**SC**). While bulk phase behavior of soft Yukawa (**YUK**) and Coulomb (**COU**) particles as well as of hard-sphere (**HS**) systems have been elaborately studied in the last decades (as briefly reported above), their crystalline phase behavior under both soft and hard confinement has still many open questions, and therefore, it is subject of this thesis.

In the present work, two different hard confinements are addressed: First, an infinitely long cylindrical cavity is applied to study the crystalline phases of Yukawa particles in the ground state ( $T = 0$ , see Chapter 1). Upon a continuous increase of the cylinder radius from zero to a finite value, one can interpolate the regime between 1D and 3D bulk. This regime is referred to as quasi-one-dimension (**Q1D**). Second, the further important hard confinement at consideration is the hard-slit, which consists of two parallelly aligned hard flat walls (see Chapters 3, 4, and 5). This realization represents a quasi-two-dimensional (**Q2D**) system, which defines the crossover from 2D to 3D in this thesis.

Soft confinements have been studied in Chapters 2, 3, and 4. This thesis considers

three types of energetic confinements: First, an attractive trap potential is applied to study the driven nucleation process of Yukawa colloids around seed particles in 2D, see Chapter 2. Second, Yukawa particles confined between two charged plates clearly show how complex the crystalline phase structures can become in Q2D (cf. Chapter 4). The charged plates, and thus a strong repulsion between the particles and the walls, denotes here the origin of an effective soft confining potential. Moreover, Coulomb particles confined in a hard slit are further exposed to a soft harmonic confinement (Chapter 3). This mixture of hard and soft confinement yield similar multilayered phases as for Yukawa particles in Chapter 4.

The 'intermediate' dimensionality Q1D (Q2D), caused by the cylindrical (slit) confinement, is tremendous for understanding the basic questions such as melting in the crossover regime from 1D (2D) to 3D. Recent experiments analyzed the melting process of hard-sphere-like particles in Q2D by using a slit geometry [37]. By interpolating the regime between 2D and 3D, different melting processes have been noticed, which develop i) from grain boundaries (as in 3D) or ii) from both the grain boundaries and within the crystalline domain (as in 2D). In addition, an understanding of freezing phenomena in the aforementioned intermediate dimensions (especially Q2D) is essential for applications like optical fibers [38] and micro-sieves [39].

Last but not least, a few words should be said about the techniques used in this thesis. This thesis combines real-space experiments with polystyrene spheres (Chapters 2, 4, 5), Monte Carlo and Brownian Dynamics computer simulations (Chapters 2, 5), and theory (Chapters 1, 3, 2, 4, 5). On a technical basis, the involved theoretical approaches contain analytical calculation of crystal growth (Chapter 2, Appendix 5) as well as analytical and numerical investigations with *penalty* (Chapter 5) and *lattice summation* (Chapters 1, 3, 4, Appendix 5) methods. Detailed descriptions are provided in the corresponding Chapters.

In brief conclusion, this thesis mainly deals with structural investigations of crystalline phases of colloidal particles in different dimensions. In a general manner, it can be roughly divided into three parts: In the first part, containing the Chapter 1, a Q1D Yukawa system is analyzed, which is realized with a cylindrical confinement. The zero-temperature crystalline phase diagram is investigated in detail. The second part, comprising the Chapter 2, concerns a pure 2D system, in which the driven crystallization of Yukawa particles is studied extensively. The third part, comprising the Chapters 3, 4, and 5, is dedicated to Q2D systems, where the phase behavior of particles with Coulomb, Yukawa, and hard-core pair interaction potentials are investigated.



# Chapter 1

## Helicity in cylindrically confined Yukawa systems <sup>1</sup>

*By lattice sum minimization, we predict the ground state of particles interacting via a Yukawa potential which are confined in a quasi-one-dimensional cylindrical tube. As a function of screening strength and particle density, the zero-temperature phase diagram exhibits a cascade of stable crystals with both helical and non-helical structures. These quasi one-dimensional crystals can be confirmed in experiments on confined charged colloidal suspensions, trapped dusty plasmas or ions in nanotubes.*

Understanding the origin of helical structures in nature is of basic importance given the fact that many biomolecules (such as DNA [40]) and inner cell structures are helical. More specifically, if particles are confined to narrow cylinders under high pressure they will spontaneously assemble into helical structures [41–44]. This has been rationalized by considering a simple model of hard spheres in cylindrical tubes where the close-packed configuration have been analyzed and indeed show helical structures [45]. Furthermore, dipolar colloidal particles [46] and thermoresponsive microspheres [44] have been shown to self-organize into chiral aggregates and  $C_{60}$  molecules [47–49] as well as polymers [50–52] confined to nanotubes exhibit spiral-like structures. Understanding the details of this pattern formation bears a high technological potential as photonic band gap fibers can be formed in cylindrical geometry [53, 54] and colloidal nanowires with novel electrical properties may be fabricated out of helical structures. Moreover, helical colloidal clusters itself can further serve as "super"-molecules [46] which in solution self-assemble into fascinating novel liquid crystalline phases [55].

In this chapter, we consider charged particles in hard cylindrical confinement

---

<sup>1</sup>This chapter was published in a very similar form by E. C. Oğuz, R. Messina, H. Löwen, Europhys. Lett. **94**, (2011) 164511.

interacting via a Yukawa pair potential. Thereby we generalize the hard-sphere model studied previously in Ref. [45] towards finite screening lengths. By lattice-sum minimization we obtain the ground state (at zero temperature) and predict a cascade of different helical and non-helical structures as a function of screening strength and particle density. In contrast to the hard-sphere case, some phases disappear at small screening and reentrant transitions show up. Our model is realized for charged colloidal suspensions under cylindrical confinement (cf. [56–65]), for trapped dusty plasmas [66, 67] and for charged supramolecular aggregates or molecular ions in nanotubes [68–70]. We also remark that microspheres explored in [44] are governed by soft interactions such that our work here might be relevant for the findings in Ref. [44].

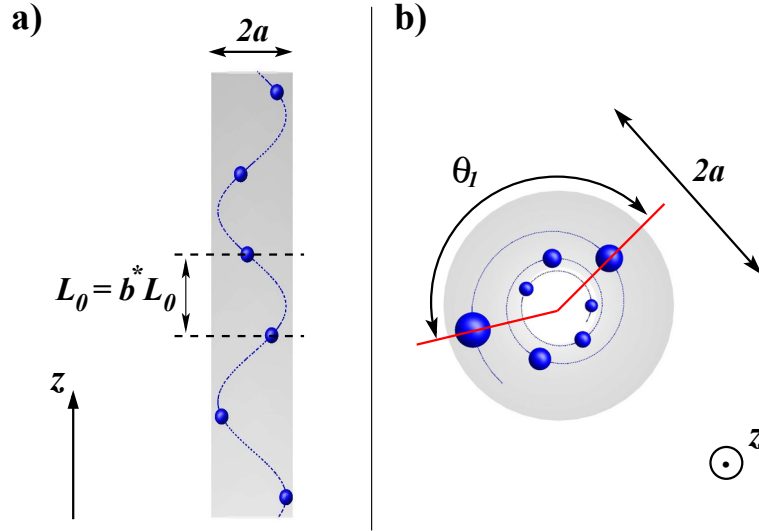


Figure 1.1: Schematic illustration of cylindrically confined particles in side (a) and top (b) view. The cylinder is shadowed and has a radius of  $2a$ . A helical phase structure is sketched. In (a) the dashed lines indicate the primitive cell of height  $L_0$ . Here, we have  $n = 1$  such that the order parameter  $b^*$  equals 1. In the top view (b), the torsion angle  $\theta_1$  between two primitive cells is shown.

In our model, we consider point-like particles interacting *via* the Yukawa pair-potential

$$V(r) = V_0 \frac{e^{-\kappa r}}{\kappa r}, \quad (1.1)$$

where  $r$  is the interparticle distance,  $1/\kappa$  the screening length, and  $V_0$  denotes an energy amplitude.  $N$  particles are confined inside a hard cylindrical tube of radius  $a$  and length  $L$  along the  $z$ -direction. At zero-temperature, for a given reduced line density  $\eta = Na/L$ , the system will minimize its total potential energy per length  $L$

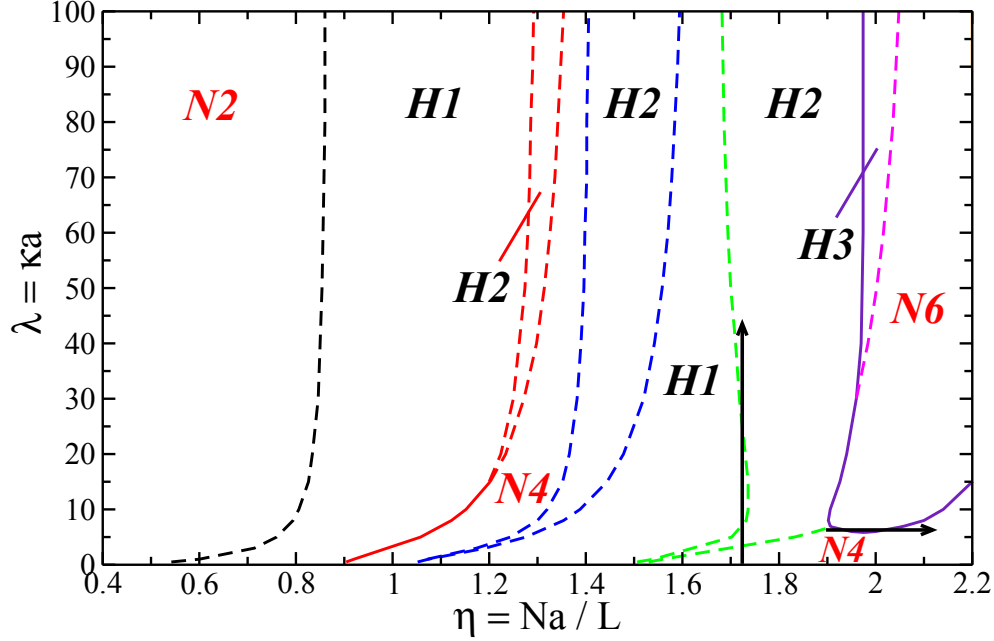


Figure 1.2: Zero-temperature phase diagram of a Yukawa system confined to a hard cylinder. As a function of screening strength  $\lambda$  and reduced density  $\eta$ , we obtain helical ( $H1$ ,  $H2$ ,  $H3$ ) as well as non-helical phases ( $N2$ ,  $N4$ ,  $N6$ ). For  $\lambda \rightarrow 0$ , the stability domain of  $H2$  shrinks to 0, while  $H3$  ( $N6$ ) already vanishes for  $\lambda \lesssim 30$  ( $\lambda \lesssim 7$ ). The dashed (full) lines indicate a 2nd (1st) order phase transition. The two arrows indicate the reentrant transitions of  $H2$  and  $N4$ .

and the resulting optimal structure will only depend on the reduced inverse screening length  $\lambda = \kappa a$ . By varying  $\lambda$ , one interpolates between the unscreened Coulomb limit ( $\lambda \rightarrow 0$ ) and the hard-sphere limit<sup>2</sup> ( $\lambda \rightarrow \infty$ ) where the interaction is getting discontinuous.

At zero-temperature and at given density  $\eta$  and reduced screening length  $\lambda$ , we have performed lattice sum minimizations for a broad set of candidate structures including helical ones. A candidate possesses a unit cell containing  $n \leq 6$  particles inside a cylindrical cavity which is then periodically replicated along the  $z$ -direction by a joint translation about  $L_0$  along the  $z$ -axis (see fig. 1.1a) and rotation about a torsion angle  $\theta$  around the  $z$ -axis. We restrict ourselves to  $0 \leq \theta \leq \pi$  selecting one special chirality (note that opposite chirality leads to the same energy). Thus, a most general unit cell with  $n = 6$  can contain multiple primitive cells with  $n = 1, 2, 3$ , resulting in the same phase structure. However, the corresponding torsion angles

<sup>2</sup>Note that in our model we have point-like particles. Nevertheless, at infinite screening ( $\lambda \rightarrow \infty$ ), by taking an effective hard-core diameter corresponding to the smallest lattice constant, one expects to recover the phase behavior of hard spheres.

might differ. To distinguish between them we denote the  $n$ -dependence of the torsion angle explicitly and refer them as  $\theta_n$  in general (cf. see fig. 1.1b). There are two classes of structures, namely *non-helical* ones which by definition are torsion-free, i.e. they can be generated with a vanishing torsion angle  $\theta_n = 0$ , or *helical* ones which necessarily involve a nonvanishing one. Nevertheless, some special non-helical structures with  $\theta_n = 0$  can also be generated with a finite torsion angle albeit with a different  $n$ .

The minimization of the total potential energy per particle is performed with respect to the positions of the  $n$  particles in the unit cell and the torsion angle while  $L_0 = na/\eta$  is prescribed by the fixed line density  $\eta$ . First we classify the resulting structures into helical and non-helical ones. Next, in case a helical structure is degenerated with respect to different  $n$ , we select from all the possible structures the one with the smallest  $n$ . For the non-helical structures, we select the structure with the smallest  $n$  as well, which also satisfies a vanishing torsion angle. To characterize the height distribution of the particles in the unit cell, we assign, for each structure, a dimensionless order parameter  $b^* = n \min_{i \neq j} \{|z_i - z_j|/L_0\}$ , which describes the smallest (reduced) interparticle distances among all distinct particle pairs  $(i, j)$  along the  $z$ -direction.

We explore the stability phase diagram in the regime  $\lambda = 0.5, \dots, 100$  for  $0 < \eta \leq 2.2$ . The results are shown in fig. 1.2. Three helical structures  $H1, H2, H3$  are stable which are labelled according to their (minimal) number of particles per unit cell while  $H$  stands for "helical". Besides three stable non-helical structures  $N2, N4, N6$  set in. All these non-helical structures  $Nn$  (with  $n = 2, 4, 6$ ) can also be generated by a nonvanishing torsion angle  $\theta_n$  with smaller unit cell number  $n = 1, 2, 3$  as compared to that corresponding to the torsion-free generation. Details are summarized in Tab. 1.1 where also the corresponding values of the order parameters  $b^*$  and  $\theta_6$  are given. For instance, for the  $H1$  structure,  $b^* = 1$  while for  $H2$  and  $H3$ ,  $0 < b^* < 1$ . The non-helical phase  $N2$  has a zigzag arrangement which can also be considered as a helix with  $\theta_1 = \pi$  and  $b^* = 1$ . For the non-helical phase  $N2$  ( $N4$ ), each two (three) particles in the same unit cell possess the same  $z$ -coordinate. Furthermore, the non-helical "doublets" ("triplets") of  $N4$  ( $N6$ ) are generated with a torsion angle  $\theta_6 = \pi/2$  ( $\theta_6 = 0$ ) with  $b^* = 0$ . In case of  $N6$   $\theta_6$  can also be chosen as  $2\pi/3$ , which yields the same phase. In all phases, all particles are located on the cylindrical surface although this was not assumed a priori. At higher densities, this will no longer be true in general.

Let us now discuss in greater depth the ground state phase diagram in the  $\eta\lambda$ -plane (fig. 1.2). For large  $\lambda$ , we recover the stability sequence put forward for hard spheres in cylindrical confinement in Ref. [45], namely

$$\begin{aligned} N2 \rightarrow H1 \rightarrow H2 \rightarrow N4 \rightarrow H2 \rightarrow H1 \\ \rightarrow H2 \rightarrow H3 \rightarrow N6, \end{aligned} \quad (1.2)$$

for increasing density  $\eta$ . On the other hand, the opposite Coulomb limit  $\lambda \rightarrow 0$  corresponding to unscreened ions in a cylinder, has not been considered before.

Here we find the stability sequence

$$N2 \rightarrow H1 \rightarrow N4 \rightarrow H1 \rightarrow H2 \rightarrow N4, \quad (1.3)$$

i.e. the phases  $H3$  and  $N6$  vanish and the stability domain of  $H2$  shrinks to a single point at  $\eta = 1.50$ . This implies that non-helical phases are preferred for the Coulomb limit (relative to the hard sphere case). This general trend can be intuitively expected since the long-ranged Coulomb potential prefers more isotropic structures than the hard-sphere interaction which considers local packing constraints.

Interpolating between these two extremes at finite  $\lambda$ , the phase behavior is not just a simple interpolation but exhibits interesting reentrance effects, which are indicated by the vertical and the horizontal arrow in fig. 1.2. For increasing  $\lambda$ , the  $H2$  phase is reentrant at about  $1.68 < \eta < 1.74$ . Another reentrance effect occurs for the  $N4$  phase upon increasing  $\eta$  at fixed  $\lambda \approx 7$ . This is in line with the general observation that confinement effects (or external fields in general) yield reentrance [56].

We remark that the reentrance of solid phases resembles the isostructural solid-to-solid transition which occur in three-dimensional square-well [71, 72] and square-shoulder [73] systems. However, in the latter case, there is a true coexistence region between the two solids and a critical point shows up. Both features are absent here. Moreover, the pure Yukawa bulk system does not exhibit any reentrance in the density-temperature plane, hence reentrance is induced by confinement alone.

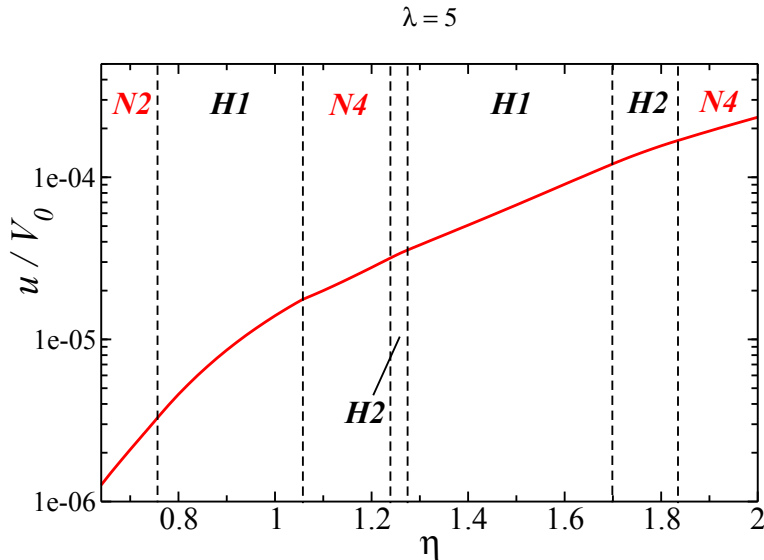
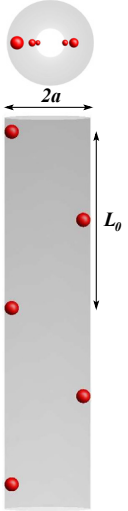
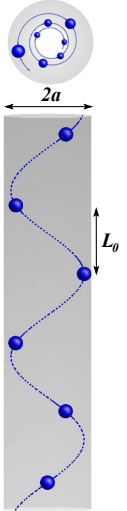
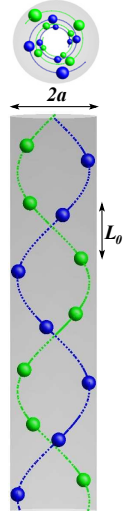
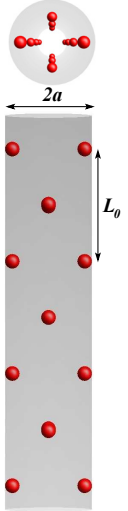
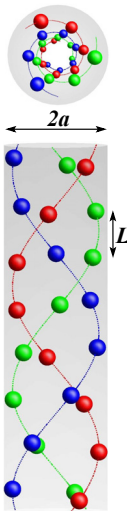
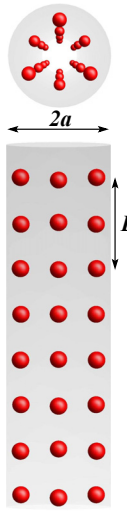


Figure 1.3: (Color online) The static potential energy per particle  $u$  as a function of  $\eta$  for  $\lambda = 5$ .

Table 1.1: Stable phase structures of the confined Yukawa system. The cylindrical confinement is illustrated by a gray tube of diameter  $2a$ . Two categories of stable phases are obtained: helical ( $H1$ ,  $H2$ ,  $H3$ ) and non-helical phases ( $N2$ ,  $N4$ ,  $N6$ ). The helical geometry of  $H1$ ,  $H2$ , and  $H3$  is indicated by the helical lines connecting periodically repeated particles of the unit cell. Different particles of the unit cell are connected by different helices and are shown in different colors. For each phase, we show a top (upper) and a side (lower) view. Furthermore, possible values of  $b^*$  and  $\theta_6$  for each structure are also given. We also show the height of each primitive cell of helical phases as well as the height and the torsion angle of the torsion-free unit cell of the non-helical ones. Additionally, we show  $\theta_3$  for  $N6$ , for clarity.

$N2$	$H1$	$H2$	$N4$	$H3$	$N6$
$\theta_6 = 0$ $\theta_2 = 0$ $b^* = 1$	$0 < \theta_6 \leq \pi$ $b^* = 1$	$\pi/3 < \theta_6 < 2\pi/3$ $0 < b^* < 1$	$\theta_6 = \pi/2$ $\theta_4 = 0$ $b^* = 0$	$\pi/2 < \theta_6 < 2\pi/3$ $0 < b^* < 1/3$	$\theta_6 = 0$ (or $\theta_6 = 2\pi/3$ ) $\theta_3 = \pi/3$ $b^* = 0$
					

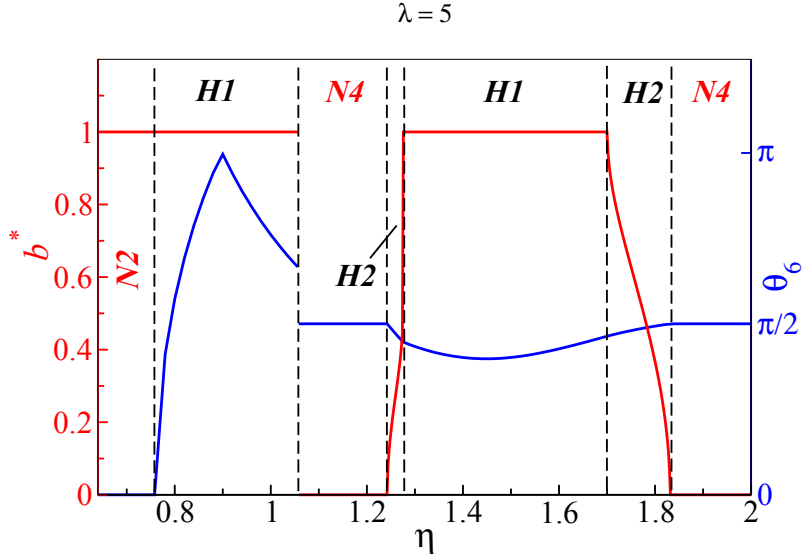


Figure 1.4: (Color online) Order parameters  $b^*$  (red line) and  $\theta_6$  (blue line) for  $\lambda = 5$  versus  $\eta$ .

We finally address the order of the various solid-solid transitions in fig. 1.2 which results from the behavior of the energy per particle across the phase transition lines. Both, first-order and second-order transitions do occur and are indicated by solid and broken transition lines in fig. 1.2. This is captured by monitoring the energy per particle  $u$  and the order parameters  $b^*$  and  $\theta_6$  of the stable phase. These observables are plotted in figs. 1.3, 1.4, 1.5, 1.6 as a function of  $\eta$  at two different  $\lambda$ . The cusps where  $\theta_6 = \pi$  in the regime of  $H1$  in the figs. 1.4, 1.6 are due to the fact that we restrict the torsion angle to the interval  $[0, \pi]$ . Hence, the cusps are not indicating a phase boundary. In fact the energy is smooth at the cusps (see fig. 1.4, 1.4). The continuously non-differentiable points of the energy functions will indicate the first-order transitions. These points are revealed by the discontinuous jumps in  $b^*$  and  $\theta_6$  as a function of  $\eta$  while a continuous behavior implies a second-order transition (see figs. 1.4, 1.6).

In summary, we investigated the crystalline stability phase diagram of the cylindrically confined Yukawa particles at zero-temperature. Our calculations yield several stable helical ( $H1$ ,  $H2$ ,  $H3$ ) as well as non-helical phase structures ( $N2$ ,  $N4$ ,  $N6$ ), where the integers denote the particles number in the corresponding unit cell. Within the density range considered here, we find that all particles are located on the surface of the cylinder. In the high screening regime, the stability cascade is given by eq. 1.2. In the plasma limit, on the other hand, the phases  $H3$  and  $N6$  are not stable anymore and the stability regime of the  $H2$  phase shrinks to zero. Furthermore, both first as well as second-order phase transitions and a rich reentrant

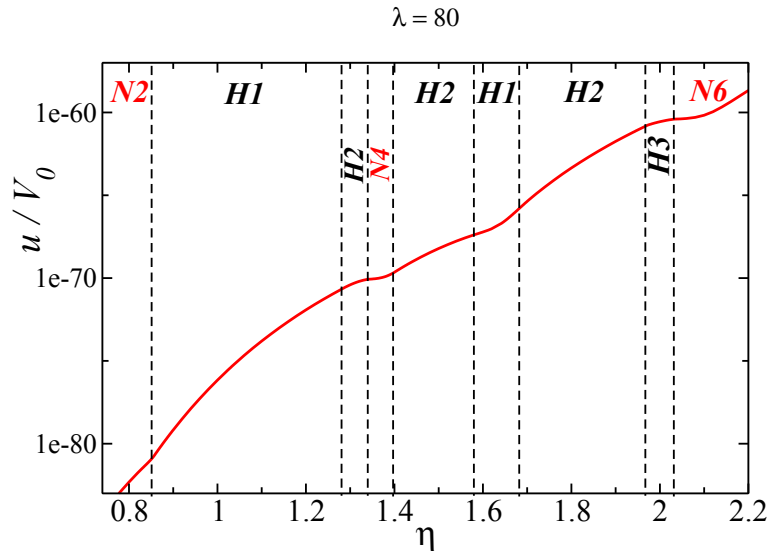


Figure 1.5: (Color online) Same as fig. 1.3 for  $\lambda = 80$ .

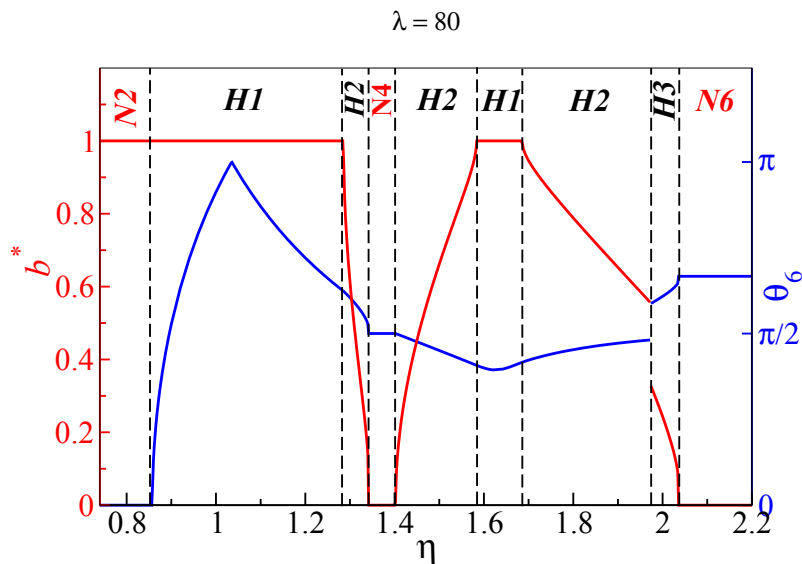


Figure 1.6: (Color online) Same as fig. 1.4 for  $\lambda = 80$ . For the  $N6$  phase,  $\theta_6$  is assumed to be  $2\pi/3$  here since the second order of the  $H3 \rightarrow N6$  becomes evident.

behavior is found.

Future work should include the consideration of higher reduced densities. For finite screening  $\lambda > 0$ , this will yield structures with particles inside the cylinder. We further remark that for  $\lambda = 0$  a homogeneously smeared opposite charge on the cylindrical surface will result in the same model as considered here since the inner

electric field vanishes.

Since there is no strict phase transition in one-dimensional systems with short-ranged interactions for  $T > 0$  [74,75], any finite temperature will smear out the solid-solid transitions found here leading to crossovers rather than strict discontinuities. The crossover behavior, however, can be very sharp in practice such that it is still useful to discriminate between phases.

In case we considered chiral structures in the present work, only one sign of chirality was presumed. However, in real biological systems, arrangements (e.g. helices) of two different signs of chirality could coincide, leading to a crossover between the both. Hence, this first-order transition will yield an interface region, which can be analyzed in a future work and the interface structure can be determined by given system parameters.

In order to study the stability of helical arrangements and non-helical crystals in a driven suspension, one could model a Poiseuille flow through the cylinder. The results could be compared to confined colloidal bilayers under shear [76]. Moreover, more complicated confining potentials like a combination of a parabolic potential [77] and a cylindrical hard void can be studied in the future.



# Chapter 2

## Colloidal crystallization in 2D induced by electrolyte gradients <sup>1</sup>

*We investigated driven crystal formation events in thin layers of sedimented colloidal particles under low salt conditions. Using optical microscopy, we observe particles in a thermodynamically stable colloidal fluid to move radially converging towards cation exchange resin fragments acting as seed particles. When the local particle concentration has become sufficiently large, subsequently crystallization occurs. Brownian dynamics simulations of a 2D system of purely repulsive point-like particles exposed to an attractive potential, yield strikingly similar scenarios and kinetics of accumulation and micro-structure formation. This offers the possibility of flexibly designing and manufacturing thin colloidal crystals at controlled positions and thus to obtain specific micro-structures not accessible by conventional approaches. We further demonstrate that particle motion is correlated with the existence of a gradient in electrolyte concentration due to the release of electrolyte by the seeds.*

### 2.1 Introduction

Many of the properties of crystalline solids are strongly influenced by the micro-structure of the sample. This micro-structure is controlled during crystallization by a complex interplay of crystal nucleation, growth and ripening. For bulk situations but also for crystal growth from substrates it is successfully modelled by classical theories and their adaptations to the particular boundary conditions [78–84]. This behaviour is known well for metals and other atomic substances, but is also observed in colloidal

---

<sup>1</sup>This chapter was published in a very similar form by A. Reinmüller, E. C. Oğuz, R. Messina, H. Löwen, H. J. Schöpe, T. Palberg, J. Chem. Phys. **136**, (2012) 164505.

model systems. Their crystallization has intensely been investigated [85–88] due to the advantages of space and time resolved measurements and tunability of the interparticle interaction [89]. Colloidal melts and crystals are particularly well suited to surpass the restrictions for structure, growth kinetics and morphology present in crystallization from an undercooled melt. Rather the crystallization scenario is flexibly altered by external influences. External fields [58, 90–93], like e. g. electric fields [94–97], optical fields [98, 99], shear forces [100], structured templates [101, 102] or specific confining geometries [58, 103], have been successfully applied to achieve particular micro-structures not available from undisturbed bulk samples.

Experiments were also conducted in confinement to narrow slit geometries. Theoretically, crystallization in strictly 2D systems may proceed via a two step process involving an intermediate hexatic phase rather than by a first order transition involving nucleation and growth [104–106] (Kosterlitz-Thouless-Halperin-Nelson-Young). Experimentally this possibility is still under discussion [90], mainly due to the fact that many experimental systems are not strictly 2D. In both situations, 2D and 3D, the main focus so far was on a control of the crystallite size [107], the competition between wall-crystal and bulk-crystal formation [108, 109] or crystal orientation [100, 110].

We here report preliminary experimental studies combined with Brownian Dynamics simulations aiming at a controlled *positioning* of heterogeneously nucleated crystals of predetermined size. We demonstrate experimentally, that positioning of crystals can be achieved by arbitrarily locating seed particles which release micro-ions. The charged colloidal spheres move in reaction to the formed lateral electrolyte concentration gradients and gravity to accumulate at the seeds and there subsequently crystallize. Starting from a thermodynamically stable colloidal fluid, the final crystallite size is determined by the strength and range of the electrolyte gradients. Furthermore, the particular seed size and shape determine whether single domain or multi-domain crystals emerge. The experiments reported are at present restricted to the study of crystal formation at single seeds of some ten  $\mu\text{m}$  size placed on the lower plate in a narrow slit geometry. Due to gravity and the use of large colloidal particles this results in monolayer colloidal fluids and crystals. Our method of micro-structure control should, however, be applicable also to 3D situations with many seeds and/or meta-stable colloidal shear melts, thus offering the potential to grow large microstructured polycrystalline solids with arbitrary crystallite patterns. While the underlying microscopic mechanism is not unequivocally identified from the crystallization experiments and subsequent additional investigations, the phenomenology of the crystal formation is well reproducible; as is the confirmation of the observed microstructures in simulations assuming a convergent solvent flow. In principle, this offers the future possibility to design extended multi-crystal microstructures based on given experimental flow direction and strength. The detailed correlation of these flow conditions to the experimental boundary conditions remains an open question at present. We therefore also present further experiments motivated by earlier findings on particle motion in electrolyte gradients both in the bulk

and close to a substrate [111–114].

The remainder of the paper is organized as follows. We first shortly introduce the employed colloidal particles, seed particles and the microscopic techniques in the experimental section. We then explain the analysis of the microscopically observed crystal growth by image processing and analysis techniques and present our results obtained on isolated seed particles. In the following simulation section we shortly present the employed techniques and then highlight our results on flow driven crystallization with respect to dependence of the microstructure on seed size and shape and the finite final crystallite size. The discussion section compares the obtained results and demonstrates the good qualitative agreement between experimental findings and simulation results. This section also presents the additional measures taken to explore the underlying mechanism and discusses their results in the light of previous experimental and theoretical work. It is demonstrated, that crystallization is unequivocally linked to the application of electrolyte gradients. The resulting flow conditions, however, seem to be crucially dependent on the background electrolyte concentration and the chosen cell geometry. This discussion part therefore poses the interesting challenge of clearly discriminating electrophoretic, chemiphoretic, osmotic and electro-osmotic contributions to flow generation in future experiments and their description in a combined model. Finally a short conclusion is given. The future perspective of crystal patterning is shortly touched. Further theoretical considerations can be found in the appendix. Further photographic material can be found online in the supplemental materials.

## 2.2 Experimental section

### 2.2.1 Experiment

In our experiments we used suspensions of negatively charged colloidal Polystyrene spheres (diameter  $2a = 5.19 \pm 0.08 \mu\text{m}$ , Batch No PS/Q-FB1036, Microparticles Berlin GmbH, Germany) in water. The suspension was prepared at a bulk volume fraction  $\phi \approx 8\%$  under strongly deionized conditions in a special tube circuit containing a mixed bed ion exchanger column [115]. Samples were observed in a home-built microscopy cell with parallel plate geometry which was connected to the conditioning circuit. Care was taken to seal the cell interior against contamination with airborne Carbon Dioxide and the ion concentration was monitored *in situ* using an integrated conductivity measurement cell. The distance between the opposing flat quartz glass windows was adjusted by piezo actuators. During conditioning the slit height was large to allow for fast and efficient homogenization and deionization of the sample. After reducing the ion concentration to significantly less than  $1 \mu\text{mol/l}$  the pump was stopped and the horizontal confining cell walls were adjusted to a typical distance of  $d \approx 15 \mu\text{m}$  for observations on colloidal monolayers crystallizing at small seed particles. The cell was placed on the stage of an inverted optical scien-

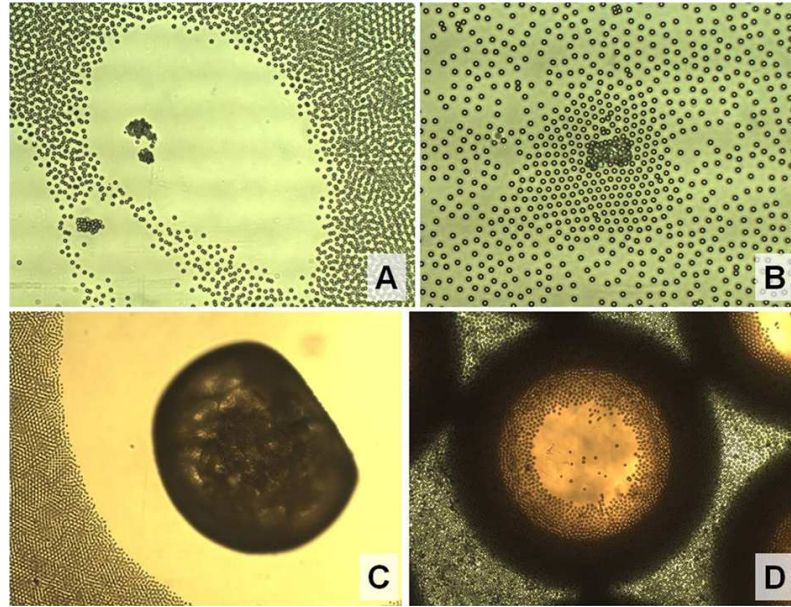


Figure 2.1: Voids free of particles in a bilayer system (a),  $565 \times 420 \mu m^2$ ) and particle accumulation in a monolayer system (b),  $360 \times 290 \mu m^2$ ) around isolated fragments of ion exchange resins. Similar influences of macroscopic ion exchange resin objects on sedimented colloidal particles were frequently observed: Void formation around anion exchange resin (“A-seed”, (c),  $1170 \times 880 \mu m^2$ ) and accumulation of mobile particles in the circular gap between a cation exchanger sphere and the quartz substrate (“C-seed”, (d),  $720 \times 540 \mu m^2$ ).

tific microscope (DM-IRBE, Leica, Germany) and observed through a 20x objective using a standard video camera. The employed seed particles were small pieces of ion exchange resin (Amberlite, Roth GmbH, Germany) which either were already present in the cell after escaping from the ion exchange column of the circuit or were deliberately added. Their position was directed by the flow conditions during conditioning, but the seeds remained stationary during measurements. For the experiments with large ( $700 \mu m$ ) seed particles larger cell heights or ion exchange resin seeds placed on a quartz substrate covered by a drop of suspension were employed.

Fluid monolayers settled under gravity formed within less than one minute after stopping the pump. Strong effective interactions between the small ion exchange resin fragments and the surrounding colloidal particles were observed: In some cases, voids free of particles formed (cf. Fig. 2.1(a)). In other cases, attraction of particles happened leading to accumulation and even to crystallization (cf. Fig. 2.1(b)), on which we focus in this report. Both effects occurred on timescales of about five minutes. Similar particle depletion and accumulation effects were frequently ob-

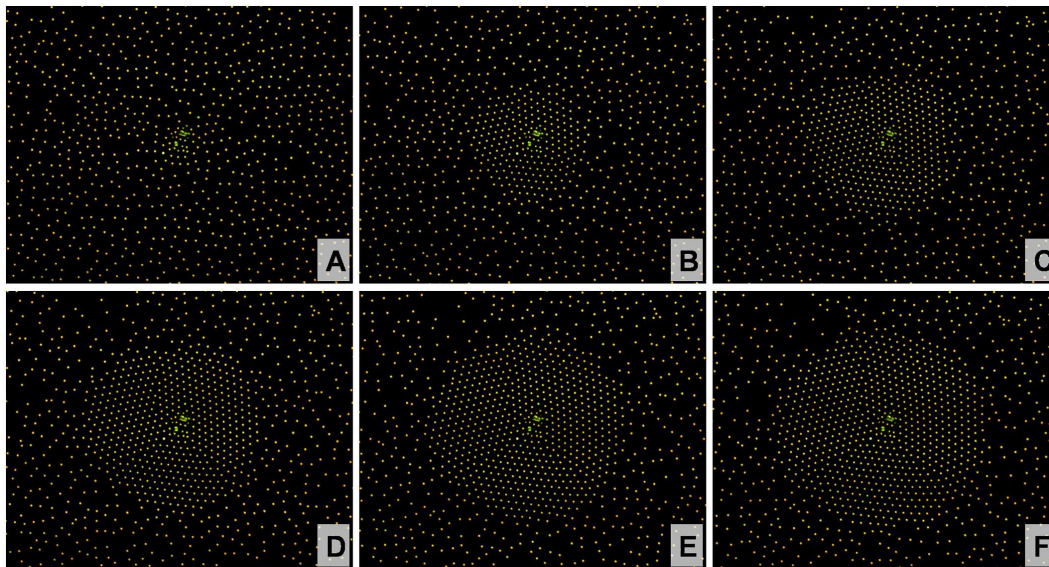


Figure 2.2: Growth of a three-domain monolayer crystal on a seed at  $t = 0s$  (A),  $t = 100s$  (B),  $t = 200s$  (C),  $t = 300s$  (D),  $t = 400s$  (E) and  $t = 500s$  (F); field of view:  $360 \times 290 \mu m^2$ .

served also at macroscopic anion (cf. Fig. 2.1(c)) exchange resin beads (A-seeds) and cation (cf. Fig. 2.1(d)) exchange resin beads (C-seeds). In particular for the case of cation exchanger, significant convection-like fluid flow leading to particle accumulation could be traced under suitable experimental geometries.

Fig. 2.2 shows a sequence of optical micrographs of the same crystal growing from a small seed particle at different times with time intervals of each 100s. The Airy-discs of the particles appear as bright circular dots on a dark background with strongly increased camera contrast in the phase contrast mode. The irregularly shaped seed in the image center consists of an ion exchange resin fragment of greenish appearance and immobile colloidal particles. In this example an almost circular monolayer crystal with triangular structure is formed. The three domains grow with a steadily decreasing radial growth velocity. Recording of frames was stopped when there were no significant changes in the system evident any more. Each new incoming particle arranged without a noticeable delay time into the crystal. Thus the crystal growth velocity was limited by the particle transport. Except for a few particles already attached to the seed all particles stayed mobile. At other seed particles, mono domain crystals but also crystals with more than one domain were observed. Typical crystal lattice constants were in the range  $d_{NN} \sim (8.0 \pm 0.5) \mu m$ , i.e.  $d_{NN} \sim 3a$ , and small crystal distortions were present. Some of the crystals were noticeably asymmetric, *i.e.* not perfectly circular (cf. Fig. 2.1B), and not well centered around the seed.

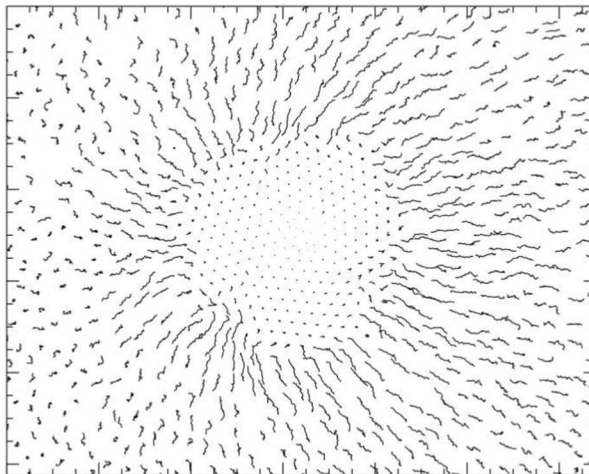


Figure 2.3: Particle trajectories of the same sequence from Fig. 2.2 between  $t = 120s$  and  $t = 180s$ . Initially a fast ceasing fluid flow was running from right to left as a result of positioning the confining walls.

Fig. 2.3 shows particle trajectories corresponding to Fig. 2.2 in the time interval beginning at  $t = 120s$  and ending at  $t = 180s$ . The trajectories display mainly a directed radial motion superimposed by random Brownian motion. A slight asymmetry in the field of trajectories is visible: Particles at the right margin display a more pronounced directed motion than particles at the left margin. This might be due to small local asymmetries in the confining geometry or the released electrolyte gradient or due to weak large-scale drift currents as a result of slow mechanical relaxation processes of the setup components. Significant initial fluid flow resulting from positioning the confining walls ceased within one minute.

Experimental observations were qualitatively well reproducible after homogenizing the suspension again by pumping or by fast vertical movements of the piezo actuators. Both induce strong solvent currents which shear melt existing crystalline structures. Without external disturbance crystals were stable as long as the experimental conditions were stable. However, the lattice constant shrank by some 10% over about one hour due to contamination with salt ions screening the inter-particle repulsion.

### 2.2.2 Analysis of crystal growth

For quantitative analysis of the crystallization process first a standard tracking algorithm [13] was applied on the image sequences. Using the gathered particle positions the six-fold bond order parameter

$$p_6 = \sqrt{\psi_6^* \psi_6} \geq 0.9 \quad (2.1)$$

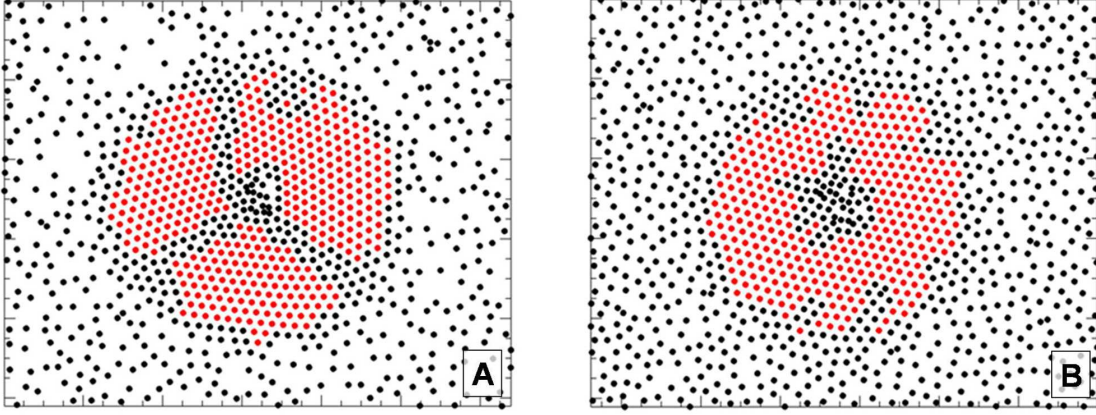


Figure 2.4: Analysis of the experimentally observed three domain crystal (a), cf. Fig. 2.2) and mono-domain crystal (b) each at  $t = 500s$ ; crystalline particles fulfilling the local criteria according to Eqs. 2.1 and 2.2 are drawn in red, all others in black. A few doublets of coagulated particles lead to local defects in the crystal. ( $360 \times 290 \mu m^2$ )

with  $\psi_6 = \frac{1}{6} \sum_{j=1}^6 e^{6i\theta_j}$  and  $\theta_j$  denoting the angle between a nearest neighbor bond and a fixed reference axis and the relative bond length deviation

$$b_6 = \frac{1}{6} \sum_{j=1}^6 \frac{|l_j - \bar{l}|}{\bar{l}} \leq 0.1 \quad (2.2)$$

with  $\bar{l}$  denoting the average bond length between a particle and its six nearest neighbors were used for identifying crystalline particles [116]. Both  $p_6$  and  $b_6$  were calculated for each particle individually. Fig. 2.4 shows the final state of two growth sequences each after 500s. Crystalline particles with respect to formulae 2.1 and 2.2 are plotted in red, all others in black. The poly-domain structure in Fig. 2.4(a) and the mono-domain structure in Fig. 2.4(b) are clearly visible. Further, from image analysis, also the average nearest neighbor distance of crystalline particles of  $d_{NN} = (7.6 \pm 0.3) \mu m$  in both cases was obtained.

The corresponding crystal sizes in terms of crystalline particle numbers  $N_c(t)$  and the effective crystal radii

$$R_c(t) = \sqrt{N_c(t)/\pi\rho_c} \quad (2.3)$$

as a function of time are shown in Figs. 2.5(a) and 2.5(b) respectively. Here  $\rho_c$  denotes the area particle number density of the crystal calculated out of the average nearest neighbor distance  $d_{NN}$ , that both did not change significantly during growth.

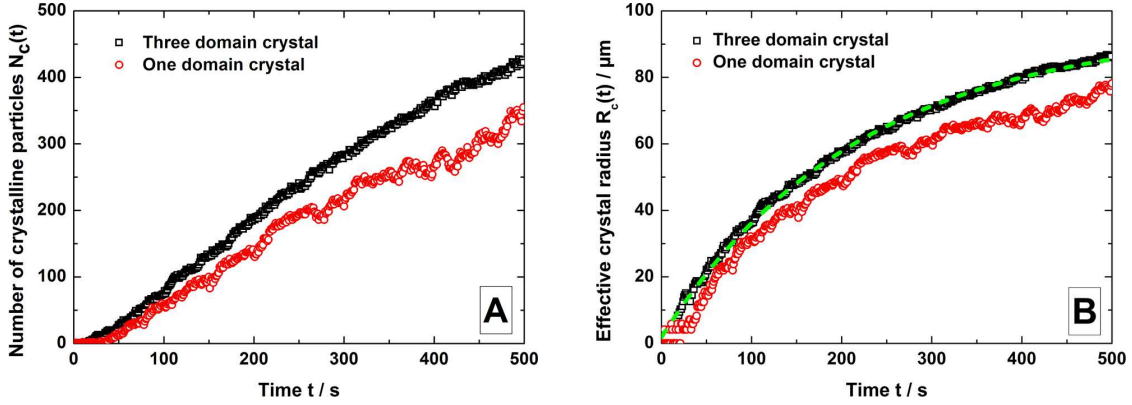


Figure 2.5: Experimentally observed crystal growth: Number of crystalline particles  $N_c(t)$  (a) and effective crystal radius  $R_c(t)$  (b) vs. time  $t$ ; black curves correspond to the three domain crystal (Fig. 2.4(a)) and red curves correspond to the mono domain crystal (Fig. 2.4(b)). The green dashed line in (B) is an exponentially saturating fit to the black curve.

Flattening of the curves indicate an exponentially decreasing growth velocity, which is explained in detail with a theoretical model in the Appendix A (cf. Eq. 5.14) :

$$R_c(t) = R_\infty - \bar{R}e^{-\lambda t}, \quad (2.4)$$

where  $\bar{R}$  is a fit parameter and  $\lambda$  the characteristic rate constant.  $R_\infty$  denotes the saturation radius, which is expected to set in for large times. An according fit function is drawn in green in Fig. 2.5(b).

For the crystallization events presented here the saturation radii amount to  $R_\infty \approx 95\mu\text{m}$  (three domain crystal) and  $R_\infty \approx 80\mu\text{m}$  (mono-domain crystal), and the characteristic time constants amount to ca.  $\lambda^{-1} \approx 215\text{s}$  and  $\lambda^{-1} \approx 200\text{s}$ , respectively. Those values may later serve for comparison with results of the theoretical modeling of the system.

## 2.3 Simulations

We performed Brownian dynamics simulations of purely repulsive point-like particles in two dimensions. We assume the particles to be confined in a disk and interact via a Yukawa pair potential [117, 118]

$$V(s) = V_0 \frac{e^{-\kappa s}}{\kappa s} \quad (2.5)$$

with  $s$  denoting the inter-particle separation and  $\kappa$  the inverse screening length. The strength of the potential energy is thereby set by the amplitude  $V_0$ . Motivated by the

experimentally observed convection-like currents leading to particle accumulation at large cation exchanger seeds, we model the effective attractive trap force in 2D by a stationary radial flow field of the form:

$$\mathbf{F}_0(\mathbf{r}) = \gamma \mathbf{u}(\mathbf{r}) = -\gamma \frac{A}{r^3} \mathbf{r}, \quad (2.6)$$

where  $\gamma$  is the Stokesian friction coefficient,  $\mathbf{u}$  the flow velocity at  $\mathbf{r}$  (relative to the origin with  $r = |\mathbf{r}|$ ), and  $A$  a positive flow amplitude. Herein, we physically assume that the convective flow is sufficiently weak that accumulated particles stay confined to the monolayer due to gravity. The inverse square distance dependency of the flow is justified by the incompressibility of the fluid  $\nabla \cdot \mathbf{u}(\mathbf{r}) = 0$  in three dimensions. The equation for the trajectory  $\mathbf{r}_i(t)$  of colloidal particle  $i$  obeying Brownian motion (neglecting hydrodynamic interactions) after a finite time step  $\delta t$  reads:

$$\mathbf{r}_i(t + \delta t) = \mathbf{r}_i(t) + \frac{D_0}{k_B T} \mathbf{F}_i(t) \delta t + \mathbf{u}(\mathbf{r}_i) \delta t + \delta \mathbf{W}_i, \quad (2.7)$$

where  $D_0 = k_B T / \gamma$  denotes the free diffusion constant,  $k_B T$  the thermal energy, and  $\mathbf{F}_i(t)$  is the total conservative force acting on particle  $i$  stemming from the pair interactions (i.e.  $V(s)$ ) and a repulsive particle-wall interaction due to an outer circular boundary. The latter is chosen to be a truncated and shifted 6-12 Lennard-Jones potential confining the particles within a disk of a large radius  $R = 900/\kappa$ . The third term on the right hand side of Eq. 2.7 is merely due to the flow field, see Eq. 2.6. Finally, the random displacement  $\delta \mathbf{W}_i$  is sampled from a Gaussian distribution with zero mean and variance  $2D_0 \delta t$  (for each Cartesian component) fixed by the fluctuation-dissipation relation.

In the simulations, the system consists of  $N = 5000$  particles with an initial overall fluid density  $\rho_f / \kappa^2 \approx 0.002$ . We achieved good qualitative agreement with the experimental findings for a flow amplitude of  $A\kappa / D_0 = 10^4$  and an interaction strength  $V_0 / k_B T = 5 \times 10^7$ . The time step is chosen as  $\delta t = 3 \times 10^{-5} \tau$  where  $\tau = 1 / (\kappa^2 D_0)$ . The crystal formation process strongly depends on the shape of the seed. Seeds were realized by placing an arbitrarily shaped area of suitable extension in the disk centre which acted for the particles as hard core repulsive area. The particles in the first layer are thus still mobile and may adjust their spacing according to their mutual interaction. Upon inspecting the experimental data (cf. Fig. 2.4), we have considered different typical shapes of impenetrable seeds. Thereby, differently shaped poly-crystals grow depending on the seed shape. Representative snapshots can be found in Fig. 2.6 for two different shapes of the seed. About the kite-like shaped seed in Fig. 2.6(a) we obtained a three-domain crystal with three grain boundaries. We further show a second example of a circular seed yielding a mono-domain crystal with one grain boundary (cf. Fig. 2.6(b)).

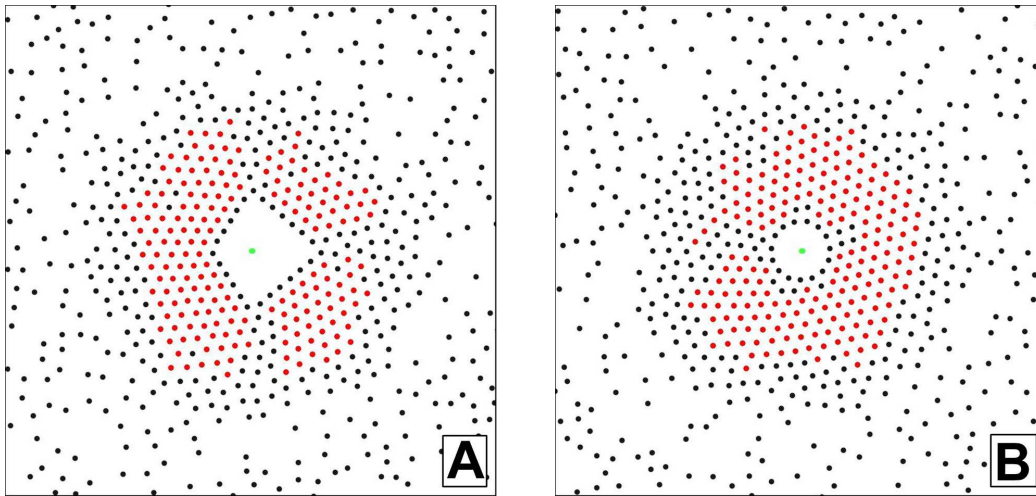


Figure 2.6: Simulation snapshots of a three-domain (a) and a mono domain crystal (b) each at  $t = 500\tau$ . The green dots in both illustrations indicate the origin of the system. The particle flow into the polygonal (a) and spherical (b) area is prohibited. Analogue to Fig. 2.4, the red particles are crystalline, the black ones not. Field of view:  $250 \times 250/\kappa^2$

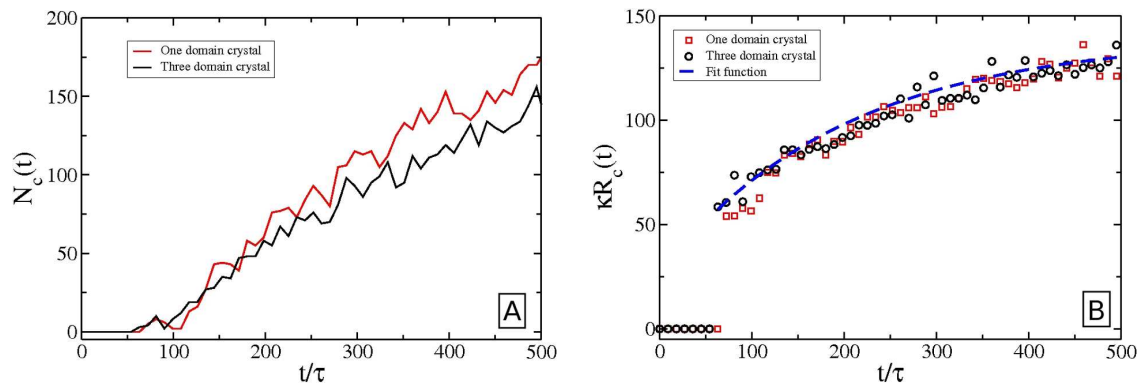


Figure 2.7: Simulated crystalline particle number  $N_c(t)$  (a) and effective crystal radii  $\kappa R_c(t)$  (b) of the three-domain (black curve/circles) and the mono domain (red curve/squares) crystals of Figs. 2.6(a) and 2.6(b) vs. the reduced time  $t/\tau$ . The blue dashed curve in (b) corresponds to an exponentially saturating fit curve with characteristic decay time  $\lambda\tau \approx 5 \times 10^{-3}$ .

The three-domain crystal as well as the mono domain crystal ceased to grow at  $\kappa R_\infty \approx 340$ . The three-domain crystal density accounts to  $\rho_c/\kappa^2 \approx 0.0027$  at saturation, whereas the density of the mono domain crystal is  $\rho_c/\kappa^2 \approx 0.003$ . The number of crystalline particles  $N_c(t)$  and the crystal radii  $R_c(t)$  from the simulation data are plotted in Fig. 2.7, from which we extract the characteristic decay time of the exponentially saturating crystal growth by fitting  $R_c(t)$ , see Fig. 2.7(b). In the considered time interval ( $0 < t/\tau < 500$ ) the characteristic time has been determined to be  $\lambda\tau \approx 5 \times 10^{-3}$ .

## 2.4 Discussion

### 2.4.1 Crystal growth

Our simulations agree qualitatively well with our experimental observations. The main equivalences are the formation of triangular monolayer crystals, the evolution of different micro-structures on different seeds as well as the exponentially saturating crystal growth. In addition they also clearly show that crystallization follows accumulation by the imposed flow.

The occurrence of only triangular crystal symmetry in both experiments and simulations is in agreement with a long range attraction that enforces an efficient packing with respect to potential energy due to the short range particle interactions. In many cases there are slight lattice distortions visible that might be correlated with the local attractive force, but on the other hand, those also might occur to reduce stress at domain boundaries. Significant radial variations of the lattice constant were not resolved.

Our observations indicate that no nucleation barrier is present in both simulation and experiment. Therefore the number of domains formed depends neither on thermodynamics nor on nucleation kinetics. Rather, the micro-structure crucially depends on the seed geometry. Hence we payed particular attention to this point in a large number of simulation runs. Point-like seeds geometrically allow perfect single-domain crystals that actually occurred in simulations. Seeds incommensurate with a triangular symmetry like squares or irregular forms induced poly-domain structures (cf. Fig. 2.6(a)) in the simulations. By contrast, the experimental seed geometries were rather irregular and not well specified. Therefore, so far no reliable relation between seed geometry and resulting morphology can be obtained experimentally. Seed materials providing the opportunity of specifically being shaped as an alternative to brittle ion exchange resins would here be of great advantage.

Further, the exponentially saturating crystal growth is evident in experiments as well as in simulations, where also saturation sets in for large times (cf. Figs. 2.5(b) and 2.7(b)). As theoretically clearly shown (see Appendix A) this behavior is also the result of a competition between the attractive, time independent, radially decaying force field and the inter-particle repulsion by already crystalline particles. The

evaluated saturation radii  $R_\infty$  of both experiments and simulations might be biased if too small particle numbers in the system are used. In this case crystallization stops when no further incoming particles are available. This effect does obviously not influence our experimental observations since the area particle number densities of the surrounding fluid ( $\rho_f \approx 0.007/\mu\text{m}^2$  and  $\rho_f \approx 0.009/\mu\text{m}^2$  for the three- and the mono-domain crystal respectively) do not change significantly during the crystallization processes. In our simulations, this artifact was avoided by using particle numbers significantly larger than that of the saturated crystal.

A quantitative comparison, however, is difficult since two important experimental parameters, namely the experimental inverse screening length  $\kappa$  and the interaction amplitude  $V_0$  in the narrow slit between the charged substrates, are principally unknown due to presence of substrate counter ions as well as salt ions set free by the seed. Further, the particle diffusion coefficient  $D_0$  in the surface plane of the substrate is difficult to estimate due to hydrodynamic particle-wall interactions as well as particle-particle interactions. Still, good qualitative agreement was obtained using physically sensible estimates of these values. Using the bulk values  $\kappa = (2.7 \pm 0.7)/\mu\text{m}$  obtained from conductivity measurements and  $D_{0,Bulk} = 0.085\mu\text{m}^2/\text{s}$  obtained from the Stokes-Einstein relation together with the experimental values  $\lambda$  and  $R_\infty$  extracted from the image sequences, we get  $\lambda\tau = (7, 5 \pm 2, 8) \times 10^{-3}$  and  $\kappa R_\infty = (260 \pm 70)$  for the three domain crystal and  $\lambda\tau = (8, 1 \pm 3, 0) \times 10^{-3}$  and  $\kappa R_\infty = (220 \pm 60)$  for the mono domain crystal. Despite the fact that these experimental values do not perfectly match the simulated values  $\lambda\tau \approx 5 \times 10^{-3}$  and  $\kappa R_\infty \approx 340$ , their orders of magnitude are equal.

Although the particle motion happens in quasi-2D, the attractive force field (cf. Eq. 2.6) was modelled assuming a velocity field  $|\mathbf{u}(\mathbf{r})| \propto 1/r^2$  rather than a field  $|\mathbf{u}(\mathbf{r})| \propto 1/r$ . This is justified since a convection-like solvent flow field will also under the given experimental conditions have vertical velocity components. For comparison also simulations using velocity fields  $|\mathbf{u}(\mathbf{r})| \propto 1/r$  were performed. These lead to similar accumulation and crystallisation scenarios, which, however, matched the experimental observations less quantitatively. Extremely long ranged attractions compared to typical interparticle distances occurred. In summary it can be said, that here reasonably good qualitative agreement between experiments and simulations is achieved by using an effective, pure 2D, long ranged attractive potential for the theoretical description instead of an explicit hydrodynamic model.

### 2.4.2 Gradient-induced particle transport

The crystallization experiments can be well reproduced using certain experimental boundary conditions, and, furthermore, the experiments can be qualitatively well modelled by referring only to the flow field. The details of the underlying mechanism are, however, still not fully understood. Their explicit discrimination and theoretical treatment is beyond the scope of the present paper and would require monitoring of micro-ion currents and solvent flow. As this question nevertheless is

extremely relevant for applications, we here give a preliminary collection of possibilities for particle transport. Based on additional experiments we can exclude several of these and suggest an ion gradient-induced particle transport as explanation of our observations.

Particle transport may, in principle, be caused by a direct seed-particle interaction, by a seed-induced gradient of some kind or by solvent flow. As in all our experiments with C-seeds, we observe an accumulation of colloidal particles in the sedimented layer(s), while at A-seeds, we regularly observed void formation, we may safely exclude thermal convection due to seed heating under illumination. This mechanism would change the amplitude of convective flow in dependence on seed material, but not its sign. Further, we observed the accumulation also under conditions of very low initial particle concentration. Particles as far away from the seed as a hundred microns were attracted or repelled immediately after stopping the mixing flow. By this observation, we can exclude a direct electrostatic attraction or repulsion, which is strongly screened over these distances even at very low particle and salt concentration ( $\kappa^{-1} \leq 1\mu m$ ). In addition, we also may exclude gradients in particle-particle interaction. Particles far away from the C-seed are non-interacting under these conditions. Accumulated particles are interacting with a strong repulsion. Therefore the direct particle-particle interaction would tend to push the accumulated particles outward. This argument also holds for the A-seeds, where the osmotic pressure in the bulk will tend to refill any void.

In all our experiments at large cell heights or without upper confining wall we observed the formation of annular currents. In particular, directly above large C-seeds we observed colloidal particles with a pronounced upward particle motion. For large seeds the currents often were too fast to allow for crystallization. As a general trend, the convection diminished with decreasing seed size. For cell heights below  $30\mu m$  (limiting the seed size to less than  $30\mu m$ ) convection was not demonstrable, as the presumably present current became too weak, to lift our large colloidal particles from their monolayer. A demonstration would be possible with much smaller particles not subject to gravitational settling. These would become traceable using image correlation velocimetry [119, 120], which is currently under development in our group.

Recently, Ibele et al. [114] reported similar particle depletion and/or accumulation effects, although without order formation. Using different chemicals in detail, they especially have observed the formation of both 'schools' and voids of colloidal tracer particles around seeds on a substrate. Based on analytical calculations by Anderson and Prieve [111–113] they identify as physical origin different concentration profiles of positive and negative ions released by the seeds.

To test the presence of ion concentration gradients we used pH-indicator liquids together with isolated pieces of resins. Significant characteristic color changes close to the resins were observed after minutes (c.f. Fig. 2.8). Both types of resin (Amberlite, Roth GmbH, Germany) release large amounts of their activator electrolytes. Those are hydrochloric acid (HCl) and sodium hydroxide (NaOH) for C-seeds and

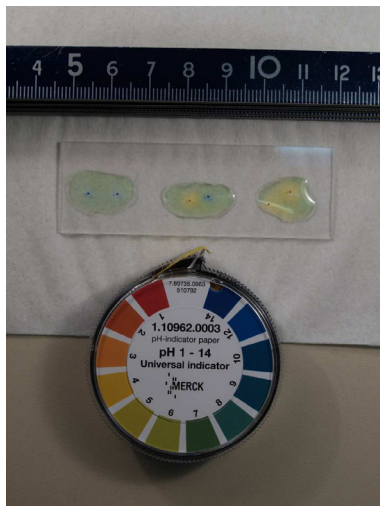


Figure 2.8: Color change of pH-indicator liquid close to isolated pieces of ion exchange resin on a glass microscopy slide: Acidic color change at cation exchange resins (yellow,  $pH \simeq 4$ ) and basic color change at anion exchange resins (blue,  $pH \geq 8$ ) occurred within ca. 5 minutes.

A-seeds, respectively. According to the observed color changes we find a change of electrolyte concentration of about 2-3 orders of magnitude over distances of a few  $mm$ .

According to Anderson et al. [111–113] a gradient of electrolyte concentration is inevitably coupled to the existence of local electric fields. This is due to the different micro-ionic diffusivities creating a space charge region of extension  $O(\kappa)$ , with the faster micro-ion drifting ahead and determining the field direction. The field strength is determined by the diffusivity difference and the local average concentration. Charged colloidal particles will react both to the gradient itself (drifting upward due to the entropy of mixing) and the field. Their electrophoretic reaction to the field depends on their charge sign and the field direction. In the case of HCl released by a C-seed,  $H^+$  has a significantly larger bulk diffusion coefficient than  $Cl^-$  ( $D(H^+) = 9.3 \times 10^{-5} cm^2/s$  and  $D(Cl^-) = 2.0 \times 10^{-5} cm^2/s$  at infinite dilution at  $25^\circ C$ ). Negatively charged particles in such a gradient, where the proton is ahead and the field is directed towards the large concentration region, will show an electrophoretic drift against the gradient. Both effects superimpose and the resulting so-called *diffusiophoretic* drift velocity and direction can be estimated analytically for  $\kappa a > 1$  or have to be calculated numerically for smaller values of  $\kappa a$  [111, 112].

The local fields will further interact with the electrical double layer (EDL) of the cell walls [114]. Again two points have to be considered. First, the imposed electrolyte gradient superimposes with the concentration profile of the wall-EDL. A lateral difference in osmotic pressure within the EDL results. This will induce an

osmotic flow of solvent volume elements of the EDL directed along the wall towards smaller electrolyte concentrations. Second, for a negatively charged wall, the EDL contains dominantly cationic species. Volume elements of the solvent within the EDL hence carry a space charge and will be accelerated by the local, gradient induced field. Similarly to the electro-osmotic effect of solvent flow along a charged wall under the influence of an *externally* applied field, this reaction of the solvent to the local gradient-induced fields results in a macroscopic flow along the cell wall. For the example of a C-seed lying on the quartz wall, the direction of the electro-osmotic flow is towards the seed. Both osmotic and electro-osmotic effects superimpose. Due to the incompressibility of the solvent an annular convection pattern has to evolve either with the formation of a centrosymmetric depletion zone or with an upward flow in the centre of the convergent flow. For the case of an A-seed osmotic and electro-osmotic effects will drive the solvent outward. For a C-seed both effects compete. According to our experimental observations, however, we find that the electro-osmotic term dominates at least for large C-seeds. The flow induced by C-seed released gradients or other kinds of gradients [114] may even become strong and fast enough to prevent order formation.

Combining our experimental observations with the theoretical considerations we unequivocally identify the presence of an electrolyte gradient to be the cause of the particle transport. The involved mechanism for large C-seeds is convective and thus dominated by the convergent electro-osmotic solvent flow. Crystallization is possible, once the local particle number density exceeds the salt concentration dependent freezing density and the local shear forces are small enough. We qualitatively sketch the field generating electrolyte gradients around a cation exchange resin particle in Fig. 2.9(a). Fig. 2.9(b) exemplarily shows the resulting laterally converging, electro-osmotically induced fluid flow for the case of a large C-seed. Due to mass conservation the geometry of this flow field enforces an upwards directed vertical flow in the convergence region, i.e. at the seed position. For suitable combinations of particle mass density and current strength, the sedimented colloidal particles are dragged along towards the resin fragment, but cannot follow the upward flow due to the presence of gravity.

For smaller seeds the cause of particle transport is also given by the presence of an electrolyte gradient. The involved mechanisms could, however, not be discriminated from the present experiments. We anticipate that a dominance of electro-osmotic currents is still present, but, in particular for an additional upper wall present and small cell heights also significantly altered flow patterns or even a suppression of convective flow could in principle occur. In that case the other mechanisms would gain importance. In principle, an attraction may even occur for the case of a small A-seed, when the inward diffusiophoretic particle motion exceeds an outward electro-osmotic solvent flow. Fortunately, for the qualitative comparison between experimental observations and simulations using an attractive potential the details of the actual mechanisms do not play a crucial role. Rather we have shown that whenever there is some kind of particle accumulation enhancing the local particle concentration

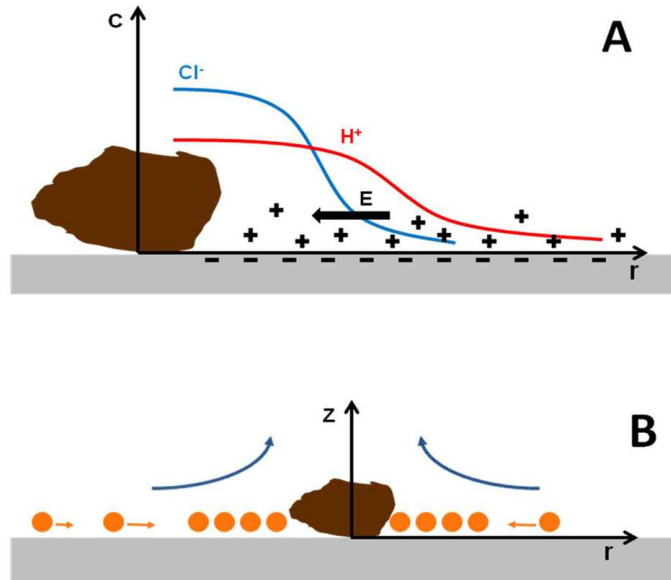


Figure 2.9: Qualitative sketch of the electro-osmotic mechanism: (a) Spatial concentration profiles of  $\text{H}^+$  ions (red curve) and  $\text{Cl}^-$  ions (blue curve) around a C-seed (brown) releasing  $\text{HCl}$ ; a balancing electric field  $E$  arises that drives the mobile counter ions (plus-signs) of the substrate (grey bar; immobile substrate surface charges are indicated by minus-signs). (b) Sketch of the electro-osmotically driven flow (blue arrows) inducing accumulation of colloidal particles (orange) next to the seed (brown).

beyond the threshold density, crystallization occurs.

## 2.5 Conclusion

In this report we investigated driven colloidal crystallization by complementary experimental and theoretical approaches. Quasi-2D transport, accumulation and crystal structure formation in a colloidal monolayer were experimentally induced using locally applied ion concentration gradient fields around cation exchange resin seed objects in slit confinement. Qualitatively equivalent results were obtained by Brownian dynamics simulations using a long-ranged trapping potential in 2D and competitive inter-particle repulsion. While we have presented strong evidence for a dominance of electro-osmotic currents in the case of large seeds, the detailed weighting of the different particle transport mechanisms possibly involved remains to be clarified in future experiments. For each given experimental boundary condition we actually expect a complex scenario which poses a number of interesting questions to theory and engineering.

The observed driven crystallization process has, to our knowledge, not been described in detail before. The pioneering work of Hachisu [121], who reported the very existence of crystals grown at ion exchange resin beads has, in fact, not been followed by further investigations to observe the crystal formation kinetics. Nor have there been attempts to study the involved transport mechanisms. Similar observations of crystal formation at sedimented ion exchange resin beads rather have occasionally been mistaken as equilibrium phenomena [122–124]. Hence our observations are innovative and may provide a novel, flexible method for designing and manipulating spatial distribution and morphology of thin colloidal crystals in fluid dispersion media. Conventional homogeneous and heterogeneous bulk crystallization provide no control of crystallite position and morphology, and fabrication of patterned substrates to induce a particular wall crystal growth pattern is (at least) tedious. Efficient modeling together with the experimental feasibility of flexibly manufacturing seeds, however, would provide the opportunity of designing specific crystalline material. It is conceivable that a printing process can be used to flexibly fabricate substrates e.g. by soft lithography or just by jet printing. Therefore it will be necessary to fabricate appropriate seed materials, e.g. a polymeric or gelling matrix that can flexibly be imprinted onto a substrate, where it releases appropriate ionic solutes slowly, and possibly even under external control. The simulations presented above on the other side reproduced the experimental findings for the given boundary conditions remarkably well. This shows in principle, that they will become very useful in designing appropriate seed distributions enforcing desired crystal microstructures. Apart from industrial relevance for the fabrication of textured iridescent coatings or photonic materials in general, we further anticipate possible uses of such combined approaches for fundamental studies, e.g. to obtain monodisperse grain sizes in polycrystalline materials or well defined multiple grain boundaries.



# Chapter 3

## Multilayered crystals of macroions under slit-confinement <sup>1</sup>

*The crystalline ground state of macroions confined between two neutral parallel plates in the presence of their homogeneously spread counterions is calculated by lattice-sum minimization of candidate phases involving up to six layers. For increasing macroion density, a cascade of solid-solid transitions is found involving various multilayered crystals. The cascade includes triangular monolayer and buckled bilayer as well as rhombic, squared and triangular phase structures.*

### 3.1 Introduction

Strong correlations in Coulomb systems lead to a variety of new effects which are absent for neutral particles, see e.g. Refs. [57, 125] for a review. Among those are nonlinear screening effects [8, 126–128], charge inversion [129], Coulomb criticality [130, 131], like-charge attraction for multivalent ions [56, 132–134] as well as exotic binary crystalline structures unknown for uncharged systems [135, 136].

By using charged colloidal suspensions [137] or dust particles in plasmas [138], it is possible to realize strongly asymmetric mixtures of oppositely charged particles. These systems consist of mesoscopic highly charged "macroions" and microscopic counterions with a low valency resulting in strong charge and size asymmetries. Since the charges of the macroions are high, strong Coulomb correlations are typical for macroions. Most of the physics can still be encapsulated by viewing these systems as strongly asymmetric and strongly coupled electrolytes. In recent years, it was

---

<sup>1</sup>This chapter was published in a very similar form by E. C. Oğuz, R. Messina, H. Löwen, J. Phys.: Condens. Matter **21**, (2009) 424110.

possible to confine macroions in sheets between two parallel plates [137, 139–142] and to observe the resulting lateral structure of the particles. The gross features can be understood in terms of an (effective) one-component system with a Yukawa pair interaction [9, 143–147]. In fact, the mono- and bilayer ground-state structures which were obtained from a Yukawa model [56] describe the experimentally found structures [103]. For multilayers beyond the bilayer regime, a rich variety of stable phases are found in experiments [148–150] as well as in simulations [151], which are all theoretically confirmed for a Yukawa system between two neutral walls [60]. This motivates a study about the influence of the wall-particle interaction on the phase behaviour of multilayered crystalline sheets in slit-like confinement [152].

In this chapter, we consider a model for macroions confined between two parallel neutral walls <sup>2</sup>. There is a direct Coulomb interaction between the point-like particles. The total system is charge-neutral and the counterions are kept at high temperature and are homogeneously spread between the plates resulting in an attraction acting on the macroions towards the middle of the plates. The system is realized for highly charged colloidal particles or dust particles in plasmas. Some early theoretical and simulational investigations on clusters of artificial atoms [154–156] and dusty plasmas [138, 157] as well as one-component plasmas [158–160], including all the parabolic potentials acting as confinement, reveals the existence of multilayers. We therefore include the regime beyond bilayers in our discussion. Lattice sum minimizations among a broad set of candidate structures are used to determine the structure which minimizes the potential energy per particle. For increasing macroion density, we find a cascade of solid-solid transitions which includes triangular monolayer, buckled bilayer and squared, rhombic and triangular bi-, tri-, tetra-, penta- and hexalayers <sup>3</sup>. Comparing the results to those involving a Yukawa interaction [60], we show that the topology of the phase diagram depends crucially on the particle-wall interaction. In fact, some complicated tetralayered structures which were found stable for the confined Yukawa model are unstable in the present model. The strong correlation between phase behaviour and wall-particle interactions suggests to tailor new crystalline structures (e.g. with desired filtering properties [162]) by a suitable surface treatment of the plates.

The paper is organized as follows: the model is introduced in section II. After discussing the structure of different crystalline multilayers, results for the cascade of solid-solid transition are presented in section III. Finally we conclude in section IV.

---

<sup>2</sup>Different from [153] we include here a neutralizing background of counterions

<sup>3</sup>For colloid-polymer films, see [161]

## 3.2 The Model

We consider  $N$  classical point-like particles of charge  $q$  (*macroions*) interacting via the unscreened Coulomb pair potential

$$V(r) = \frac{q^2}{\epsilon r}, \quad (3.1)$$

where  $r$  denotes the interparticle distance and  $\epsilon$  the (relative) dielectric constant of surrounding medium. The system is confined between two parallel hard walls of area  $A$  and separation  $L$ , see figure 3.1. The global charge neutrality of the system is ensured by counterions. The latter are taken into account by an homogeneous neutralizing background that is smeared out over the whole slit. We mention that we neglect the discrete nature of the counterions in this approach, as well as any local ion-counterion coupling.

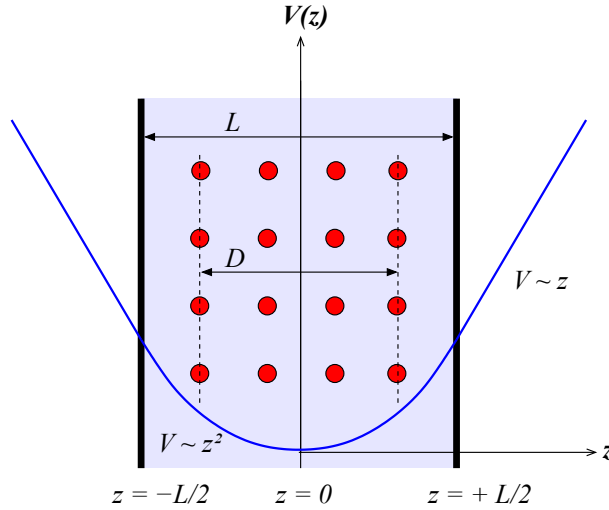


Figure 3.1: A schematic illustration of the model. The ions (e.g., charged colloids) are represented by filled circles. The counterions are smeared out between the two hard walls located at  $z = \pm L/2$ . This charge distribution generates a quadratic potential  $V(z) \sim z^2$  in between as shown. The separation between outermost layers (dashed lines) is denoted by  $D$ .

As a consequence of Gauss law, the electric field  $E_b$  (stemming from the neutralizing background) is linear in  $z$  inside the slit and constant outside the slit. More specifically, we have

$$E_b(z) = \begin{cases} -\frac{4\pi Nq}{\epsilon} \frac{z}{L} & \text{for } -L/2 \leq z \leq +L/2, \\ -\frac{2\pi Nq}{\epsilon} \frac{L}{|z|} & \text{else.} \end{cases} \quad (3.2)$$

We thereby implicitly neglect image charge effects [163], meaning that we assume that there is no dielectric contrast at the interfaces (at  $z = \pm L/2$ ). The resulting electrostatic potential  $\Phi_b$ , verifying the matching condition at  $z = \pm L/2$ , then reads

$$\Phi_b(z) = \begin{cases} \frac{2\pi\eta q}{\epsilon L^3} z^2 & \text{for } -L/2 \leq z \leq +L/2, \\ \frac{2\pi\eta q}{\epsilon L^2} |z| - \frac{\pi\eta q}{2\epsilon L} & \text{else,} \end{cases} \quad (3.3)$$

where the reduced density

$$\eta \equiv \frac{N}{A} L^2 \quad (3.4)$$

was introduced. Hence, the potential of interaction  $V_b(r)$  between a macroion and the counterion background is merely given by

$$V_b(z) = q\Phi_b(z). \quad (3.5)$$

We are now in a position to write the total potential energy per particle  $u$  as <sup>4</sup>

$$u = \frac{1}{2N} \sum_{i=1}^N \sum_{j=1}^N V(r_{ij}) + \frac{1}{N} \sum_{i=1}^N V_b(z_i). \quad (3.6)$$

In its appropriate rescaled form,  $u$  reads (within the slit)

$$u \frac{\epsilon L}{q^2} = \frac{1}{2N} \sum_{i=1}^N \sum_{j=1}^N \frac{1}{r_{ij}^*} + \frac{1}{N} \sum_{i=1}^N 2\pi\eta z_i^{*2}, \quad (3.7)$$

with  $r_{ij}^* \equiv r_{ij}/L$  and  $z_i^* = z_i/L$ , showing that at prescribed confinement width  $L$  the energy of the system depends only on  $\eta$ . Consequently the phase diagram at zero temperature is given as a function of  $\eta$ .

At each given density  $\eta$ , we have performed lattice sum minimizations for a broad set of candidates of crystalline lattices. In order to handle the long ranged Coulomb potential, we have used the Lekner summation method [164] for three-dimensional systems with two-dimensional periodicity [165], see also [166]. More explicitly, we consider in this work three-dimensional crystals with two-dimensional periodicity in  $x$ - and  $y$ -direction whose primitive cell is a parallelepiped containing  $n$  particles. This parallelepiped is spanned by the three lattice vectors  $\mathbf{a} = a(1, 0, 0)$ ,  $\mathbf{b} = a\gamma(\cos\theta, \sin\theta, 0)$  and  $\mathbf{c} = D(0, 0, 1)$ , where  $\gamma$  is the aspect ratio ( $\gamma = |\mathbf{b}|/|\mathbf{a}| = b/a$ ) and  $\theta$  is the angle between  $\mathbf{a}$  and  $\mathbf{b}$ . Furthermore, the  $n$  particles are distributed, not necessarily evenly, on  $m$  layers in the  $z$ -direction such that  $c = |\mathbf{c}|$  corresponds

---

<sup>4</sup>To remedy the divergence occurring with the first term of (3.6), a *two-dimensional* neutralizing background is introduced in the Lekner (or equivalently Ewald) sum. This neutralizing background (implicitly present in the Lekner and/or Ewald sum) has to be distinguished from the one that we use to model the counterions, which is smeared out over the whole *volume* of the slit.

to the distance between outermost layers (see also figure 3.1). Hereby we restrict ourselves to layered situations with an up-down inversion symmetry in the averaged occupancy reflecting the up-down symmetry of the confining slit. Under this sole restriction, we consider possible candidates with  $n = 1, \dots, 8$  and  $m = 1, \dots, 6$  up to symmetric six-layer structures with a basis of up to 8 particles. Furthermore, we also examine the stability of several asymmetric buckling phases, as predicted in [167]. For given  $\eta$ , the total potential energy per particle is minimized with respect to the particle coordinates of the basis and the cell geometry ( $\gamma$  and  $\theta$ ). The resulting stability phase diagrams are shown and discussed in the following sections.

### 3.3 Mono- and bilayer phase behavior

#### 3.3.1 Phase diagram

An increase of  $\eta$  within the mono- and bilayer regime reveals the existence of five stable crystalline mono- and bilayers:  $1\Delta$  (triangular),  $3\Delta$  (staggered triangular),  $2\Box$  (square),  $2R$  (rhombic) and  $2\Delta$  (staggered triangular). The integers indicate the number of layers. For increasing  $\eta$ , the stability cascade therefore reads:

$$1\Delta \rightarrow 3\Delta \rightarrow 2\Box \rightarrow 2R \rightarrow 2\Delta. \quad (3.8)$$

Most of these phases, corresponding to Wigner crystals predicted in earlier theoretical investigations [56, 153], are also found in experiments on charged colloidal suspensions [168, 169] as well as in Monte Carlo simulations of confined hard spheres [170]. The detailed phase diagram is reported in figure 3.2.

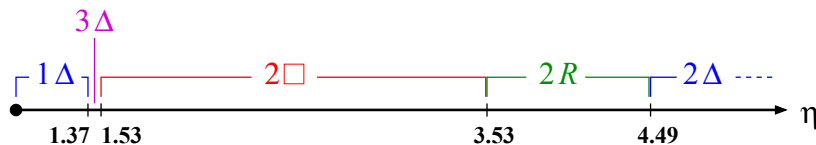


Figure 3.2: Stability phase diagram of crystalline mono- and bilayers. The five stable phases  $1\Delta$ ,  $3\Delta$ ,  $2\Box$ ,  $2R$  and  $2\Delta$  correspond to Wigner crystals, found in earlier investigations (see text for details). Note that the monolayer-trilayer transition occurs at  $\eta \approx 1.37$ .

We emphasize that the  $3\Delta$  phase (staggered in an  $ABC$  manner, see also table 3.1) intervenes between  $1\Delta$  and  $2\Box$  rather than a buckled phase which is present in a situation where the external potential has a vanishing curvature at the origin.

At small reduced densities  $\eta$ , particles tend to stay in the potential minimum (cf. figure 3.1) created by the counterion background. This is precisely the origin of the stability of monolayered Wigner crystals, which never occurs in purely unscreened

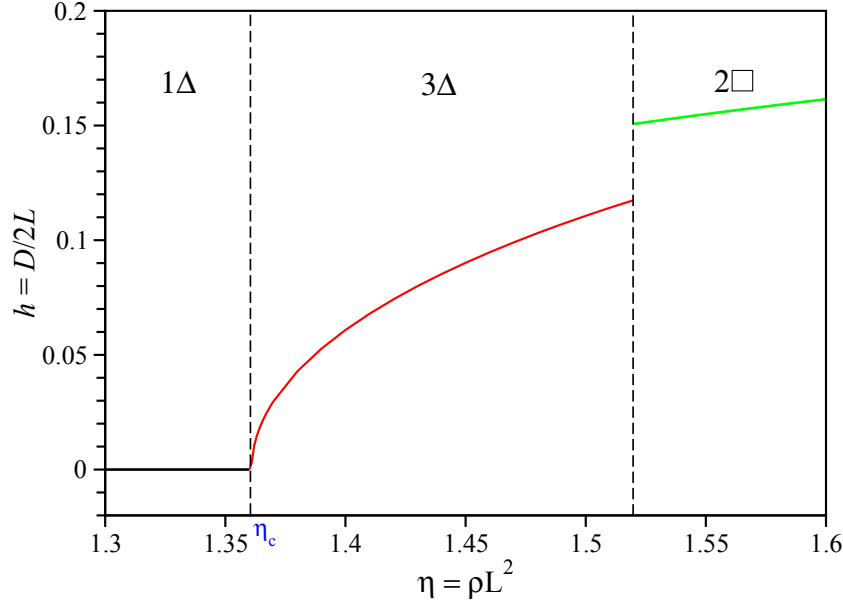


Figure 3.3: Order parameter  $h$  in the transition regime  $1\Delta$  to  $2\square$  via  $3\Delta$ . The monolayer  $1\Delta$  buckles at a critical density  $\eta_c \sim 1.360901$  to a trilayer.

Coulomb systems.<sup>5</sup> The triangular monolayer  $1\Delta$  is stable up to  $\eta = 1.37$ . At larger densities the mutual repulsive interparticle interactions, first term in equation (3.7), dominates the competition between the interparticle (macroion-macroion) repulsion and particle-background (macroion-counterion) attraction.

The structure with triangular base shape  $3\Delta$  appears as the first stable multilayer (see figure 3.3), interpolating between  $1\Delta$  and  $2\square$ . The associated order parameter, namely the reduced separation

$$h \equiv \frac{D}{2L} \quad (3.9)$$

between the mid-plane and the outer macroion layer (see also figure 3.1), is continuous at the transition  $1\Delta \rightarrow 3\Delta$  but discontinuous across the  $3\Delta \rightarrow 2\square$  transition, see figure 3.3 and [170].

By further increase of  $\eta$ , one recovers the rhombic phase  $2R$ , which is continuously achievable from the square phase  $2\square$  by changing  $\theta$ , as indicated in the inset of figure 3.4. The two geometrical order parameters  $h$  and  $\sin \theta$ , see figure 3.4, indicate thereby a continuous transition for  $2B \rightarrow 2\square$ . On the other hand, at larger values of  $\eta$ , the transition  $2R \rightarrow 2\Delta$  is of first order as signaled by the jumps of the two geometrical order parameters  $h$  and  $\sin \theta$ , see figure 3.4. The staggered triangular

<sup>5</sup>Indeed, we found that a rectangular bilayer with size ratio  $\gamma = \sqrt{3}$ , proposed as a stable structure for very small  $\eta$  in [153], is always energetically beaten by a buckled ( $2B$ ) bilayered phase. Seen from the top, this structure corresponds to the triangular lattice.

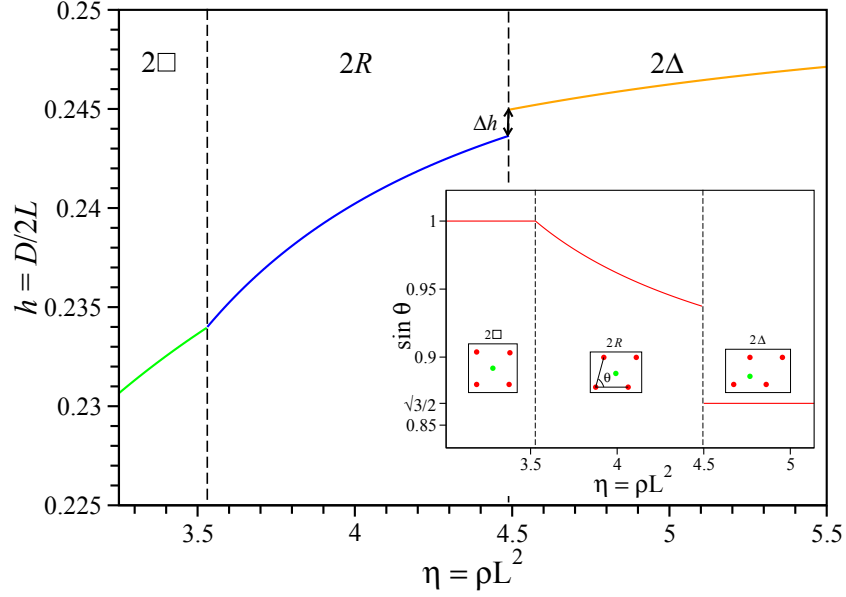


Figure 3.4: Order parameter  $h$  in the transition regime  $2\Box$  to  $2\Delta$  via  $2R$ . The discontinuity  $\Delta h$  in the developing of the layer-layer separation by the transition  $2R \rightarrow 2\Delta$  is also shown for clarity. In the inset one can regard how  $\theta$  changes in the same regime. Corresponding structures are also sketched in the inset. Different colors indicate different layers.

phase  $2\Delta$  corresponds to the ultimate stable structure in the high density regime of bilayers.

### 3.3.2 From monolayer to trilayer - An analytic approach

We now would like to address the transition  $1\Delta \rightarrow 3\Delta$  analytically. To do so, we apply a Taylor expansion to  $u(h)$  around  $h = D/2L = 0$ , see the Appendix 5 for details. The resulting asymptotic expression for small interlayer distances  $h$  reads

$$\frac{u(h)}{q^2/\epsilon L} = B_0\sqrt{\eta} + B_1\eta^{3/2}h^2 + B_2\eta^{5/2}h^4 + \frac{4}{3}\pi\eta h^2. \quad (3.10)$$

with

$$B_0 = -1.960516\dots, \quad B_1 = -3.590668\dots, \quad B_2 = 4.968827\dots \quad (3.11)$$

The profile of the reduced half layer-layer distance  $h(\eta)$  is obtained upon minimizing  $u$  with respect to  $h$ , i.e.  $\partial u/\partial h = 0$ , leading to

$$h^2(\eta) = -\frac{B_1\sqrt{\eta} + \frac{4}{3}\pi}{2B_2\eta^{3/2}}. \quad (3.12)$$

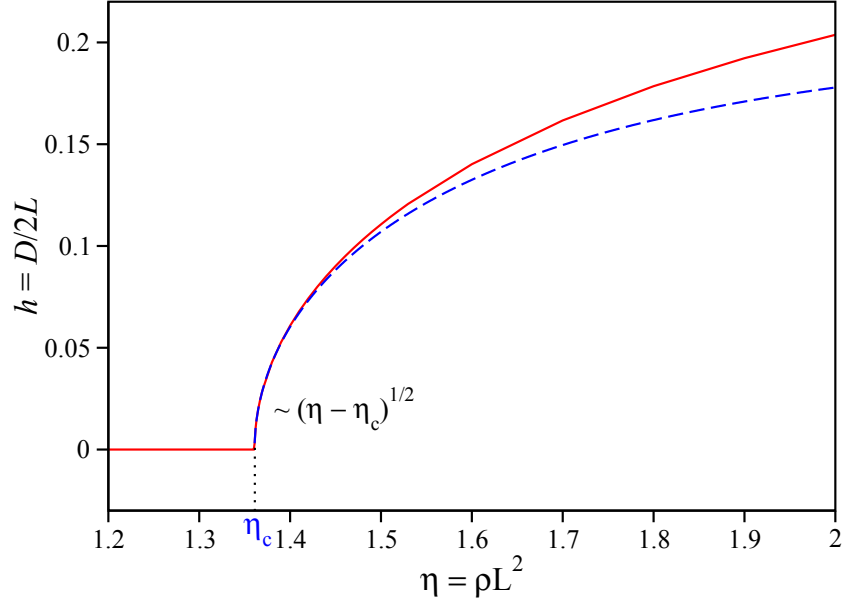


Figure 3.5: Plot of equation (3.14) (dashed line) and numerical calculations for finite  $h(\eta)$  (solid line) based on full lattice sum minimization near the monolayer-trilayer  $1\Delta \rightarrow 3\Delta$  transition.

It is now a simple matter to obtain the reduced density  $\eta_c$  at which the monolayer-trilayer transition ( $1\Delta \rightarrow 3\Delta$ ) takes place. The mathematical condition is thereby  $h(\eta = \eta_c) = 0$  yielding

$$\sqrt{\eta_c} = -\frac{4\pi}{3B_1} \Rightarrow \eta_c = 1.360901\dots, \quad (3.13)$$

which is in quantitative agreement with the lattice sum minimization results from previous section, see figure 3.5.

By inserting the expression (3.13) of  $\eta_c$  in (3.12) one obtains

$$h^2(\eta) = -\frac{B_1}{2B_2} \frac{\eta - \eta_c}{\eta^2 + \eta^{3/2}\sqrt{\eta_c}}. \quad (3.14)$$

Noticing that the last denominator in equation (3.14) can be approximated (valid in the relevant limit  $\eta \rightarrow \eta_c^+$ ) by  $2\eta^2$ , we obtain a square-root singularity:

$$\lim_{\eta \rightarrow \eta_c^+} h(\eta) = \sqrt{-\frac{B_1}{4B_2\eta_c^2}(\eta - \eta_c)^{1/2}} \sim (\eta - \eta_c)^{1/2}. \quad (3.15)$$

This theoretical prediction (3.14) is visualized in figure 3.5.

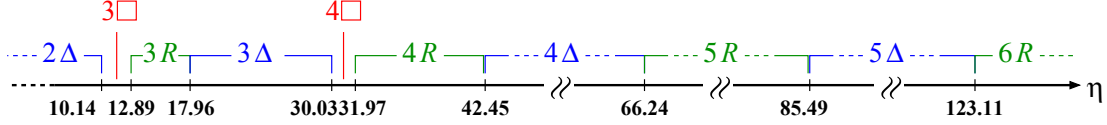


Figure 3.6: Stability phase diagram of crystalline multilayers in the presence of a neutralizing background.  $3\Box$ ,  $3R$ ,  $3\Delta$ ,  $4\Box$ ,  $4R$ ,  $4\Delta$ ,  $5R$ ,  $5\Delta$  and  $6R$  are obtained as stable in the analyzed  $\eta$ -regime. The corresponding structures are given in table 3.1.

## 3.4 Multilayers

The presence of the neutralizing background allows the formation of multilayers with  $m \geq 3$  for large enough densities  $\eta$ , which is forbidden in the absence of a background<sup>6</sup>. The physical origin of the stability of multilayers in the present system at large  $\eta$  is basically a balance between the mutual *unscreened* macroion-macroion repulsion and the attractive macroion-background interaction.

We shall now analyze in detail the high density regime up to  $\eta \approx 130$ . Beyond the bilayer regime, that is limited by  $2\Delta$ , the cascade found here upon increasing  $\eta$  reads:

$$\dots 3\Box \rightarrow 3R \rightarrow 3\Delta \rightarrow 4\Box \rightarrow 4R \rightarrow 4\Delta \rightarrow 5R \rightarrow 5\Delta \rightarrow 6R \dots, \quad (3.16)$$

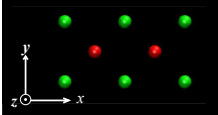
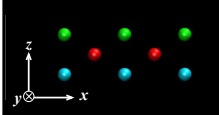
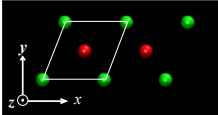
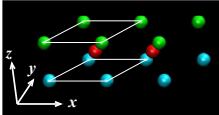
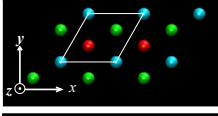
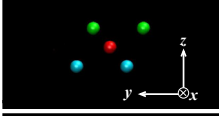
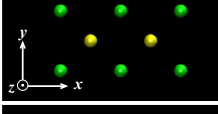
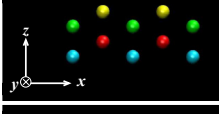
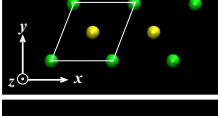
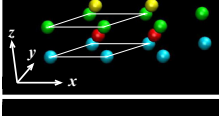
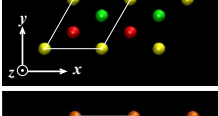
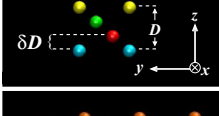
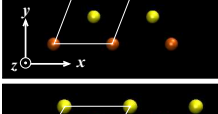
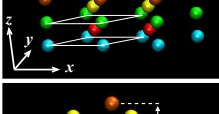
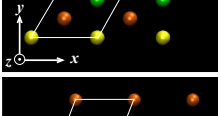
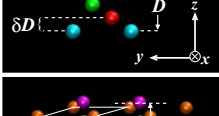
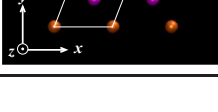
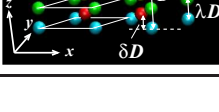
where rhombic phases  $3R$ ,  $4R$ ,  $5R$  and  $6R$  have the stacking sequence  $ABA$ ,  $ABAB$ ,  $ABABA$  and  $ABABAB$  while the triangular phases  $3\Delta$ ,  $4\Delta$  and  $5\Delta$  occur as  $ABC$ ,  $ABCA$  and  $ABCAB$ , respectively. More structural details are given in table 3.1. The corresponding phase diagram is depicted in figure 3.6.

The primitive cells of all stable phases found in this work consist of one particle per layer. Each constitutive layer possesses the same basis shape ( $\Delta$ ,  $\Box$  or  $R$ ). These layers are shifted to each other, see table 3.1. Note that (for  $m > 3$ ) the layers become equidistant only in the limit  $\eta \rightarrow \infty$ . A remarkable finding is the absence of prism phases (at  $m = 4$ ) that are encountered in hard sphere systems [148, 151] and Yukawa systems at finite screening [60].

A further overview of the full phase diagram ranging from triangular monolayer to rhombic hexalayer structures is shown in figure 3.7 where the profile of  $h(\eta)$  is also sketched. Empty circles indicate transitions of second order, while the full

<sup>6</sup>There is a simple and clear electrostatic argument to explain the exclusive stability of bilayers for charges confined between (charged or uncharged) hard walls without neutralizing *volume* background. One has to note that two equally charged walls do *not* generate any electric field within the slit, and consequently do not alter the stable structure obtained at any other surface charge (including neutral walls). Hence, if one considers the special case of two walls corresponding to *two-dimensional* neutralizing backgrounds where the ground-state is the  $2\Delta$  bilayer, we deduce from this that the ground state structure is *always* a bilayer.

Table 3.1: Structural details of the stable crystalline multilayers. The bottom layer located at  $z = -D/2$  corresponds to first layer (labeled as  $i = 1$ ), and the labels of the successive layers are incremented accordingly. For  $m > 3$ , the separation between the two first layers is characterized by  $\delta D$  with  $1/(m-1) \leq \delta < 0.5$ . The relative separation vector between two particles of a primitive cell belonging to two layers  $i$  and  $j$  is given by  $\mathbf{d}_{ij}$ . For six layers, the separation between the first and the third layers is specified by  $\lambda D$  with  $2/5 \leq \lambda < 0.5$ . In the top views of  $3\Delta$ ,  $4\Delta$ ,  $5\Delta$  and  $3R$ ,  $4R$ ,  $5R$ ,  $6R$  each basis shape is emphasized with white lines. The rhombic stripes of  $3R$ ,  $4R$ ,  $5R$  and  $6R$  are shown again in corresponding perspective views, for clarity. Particles from different layers are identified by different colors.

Phase	$\mathbf{b}/a$	$\mathbf{d}_{12}$	$\mathbf{d}_{13}$	$\mathbf{d}_{14}$	$\mathbf{d}_{15}$	$\mathbf{d}_{16}$	top view	side/persp. view
$3\Box$	$(0, 1)$	$\frac{\mathbf{a}+\mathbf{b}+\mathbf{c}}{2}$	$\mathbf{c}$	—	—	—		
$3R$	$(\cos \theta, \sin \theta)$	$\frac{\mathbf{a}+\mathbf{b}+\mathbf{c}}{2}$	$\mathbf{c}$	—	—	—		
$3\Delta$	$(1/2, \sqrt{3}/2)$	$\frac{\mathbf{a}+\mathbf{b}}{3} + \frac{\mathbf{c}}{2}$	$\frac{2(\mathbf{a}+\mathbf{b})}{3} + \mathbf{c}$	—	—	—		
$4\Box$	$(0, 1)$	$\frac{\mathbf{a}+\mathbf{b}}{2} + \mathbf{c}\delta$	$\mathbf{c}(1 - \delta)$	$\frac{\mathbf{a}+\mathbf{b}}{2} + \mathbf{c}$	—	—		
$4R$	$(\cos \theta, \sin \theta)$	$\frac{1}{2}(\mathbf{a} + \mathbf{b}) + \mathbf{c}\delta$	$\mathbf{c}(1 - \delta)$	$\frac{1}{2}(\mathbf{a} + \mathbf{b}) + \mathbf{c}$	—	—		
$4\Delta$	$(1/2, \sqrt{3}/2)$	$\frac{\mathbf{a}+\mathbf{b}}{3} + \mathbf{c}\delta$	$\frac{2(\mathbf{a}+\mathbf{b})}{3} + \mathbf{c}(1 - \delta)$	$\mathbf{c}$	—	—		
$5R$	$(\cos \theta, \sin \theta)$	$\frac{\mathbf{a}+\mathbf{b}}{2} + \mathbf{c}\delta$	$\frac{\mathbf{c}}{2}$	$\frac{\mathbf{a}+\mathbf{b}}{2} + \mathbf{c}(1 - \delta)$	$\mathbf{c}$	—		
$5\Delta$	$(1/2, \sqrt{3}/2)$	$\frac{\mathbf{a}+\mathbf{b}}{3} + \mathbf{c}\delta$	$\frac{2(\mathbf{a}+\mathbf{b})}{3} + \frac{\mathbf{c}}{2}$	$\mathbf{c}(1 - \delta)$	$\frac{\mathbf{a}+\mathbf{b}}{3} + \mathbf{c}$	—		
$6R$	$(\cos \theta, \sin \theta)$	$\frac{\mathbf{a}+\mathbf{b}}{2} + \mathbf{c}\delta$	$\mathbf{c}\lambda$	$\frac{\mathbf{a}+\mathbf{b}}{2} + \mathbf{c}(1 - \lambda)$	$\mathbf{c}(1 - \delta)$	$\frac{\mathbf{a}+\mathbf{b}}{2} + \mathbf{c}$		

ones denote transitions of first order. In detail, for 3- and 4-layers, the transitions  $3\Box \rightarrow 3R$  and  $4\Box \rightarrow 4R$  occur continuously by continuously changing the angle  $\theta$  between the two in plane basis vectors, in analogy to  $2\Box \rightarrow 2R$  (cf. figure 3.4), while all other transitions are discontinuous. Additionally, by the transitions  $3R \rightarrow 3\Delta$ ,  $4R \rightarrow 4\Delta$  and  $5R \rightarrow 5\Delta$ , and by the transitions changing the layer number at  $\eta = 1.53$  ( $3\Delta \rightarrow 2\Box$ ),  $\eta = 10.14$  ( $2\Delta \rightarrow 3\Box$ ),  $\eta = 30.03$  ( $3\Delta \rightarrow 4\Box$ ),  $\eta = 66.24$  ( $4\Delta \rightarrow 5R$ ) and  $\eta = 123.11$  ( $5\Delta \rightarrow 6R$ ) the distance between outermost layers exhibits a certain jump  $\Delta h$  (indicated by thick arrows in figure 3.7). In fact, there is here no continuous transition present between two unequal layered phases as in the case of hard spheres <sup>7</sup>.

Furthermore, for high densities, the concrete lattice evolves to a continuous such that effects due to the concreteness get negligible. This means, electrostatically, that each layer of a  $m$ -layered structure is completely compensated by a certain part of background as much as  $1/m$  of the whole.

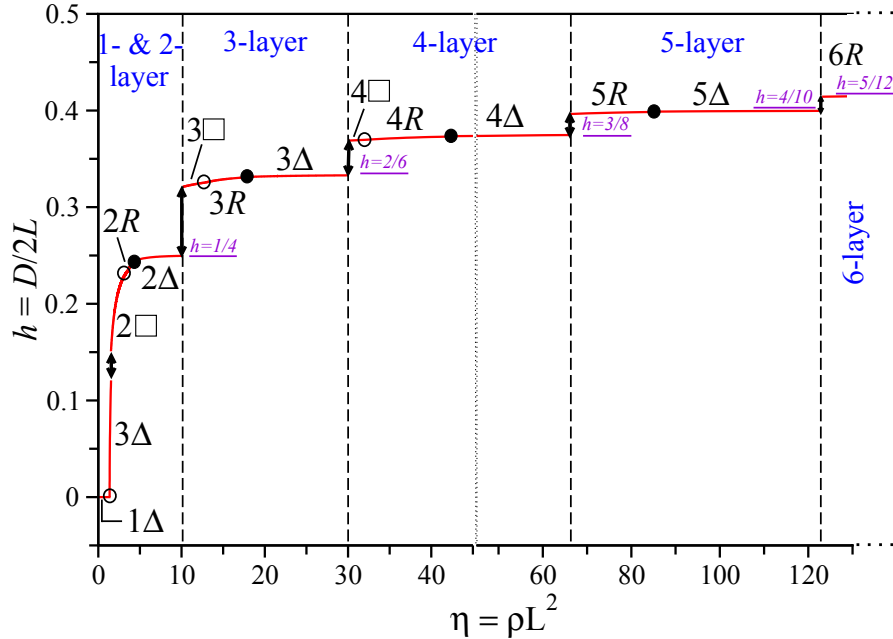


Figure 3.7: Order parameter  $h$  of all stable crystalline phases. Empty circles denote a continuous transition, while the full circles mark a discontinuous one. The transitions between different layer numbers, rendered as dashed lines, are also recorded as a first order transition except  $1\Delta \rightarrow 3\Delta$ . Apart of that, the underlined  $h$ -numbers give the limit  $h$ -value ( $\eta \rightarrow \infty$ ), for the case that no more phase transition to a higher layered structure occurs. The dotted line indicates a scale change in  $\eta$ -axis.

<sup>7</sup>In the case of bilayered hard spheres, one can achieve a continuous layer increase from  $2\Delta$  to four-layered hcp-like and hcp(100) phase [60, 149, 150].

In this chapter we have dealt with a system consisting of particles (*macroions*) interacting via the unscreened Coulomb potential and of particles of opposite charge (*counterions*), which are homogeneously smeared out over a hard slit of width  $L$ , compensating the charge of the macroions. To determine the stability diagram of crystalline phases, we have performed lattice sum calculations of a set of candidates. As possible candidates we have taken into account phases with up to six layers ( $m = 1, \dots, 6$ ) whose primitive cell contains up to eight particles ( $n = 1, \dots, 8$ ). Additionally, we considered the buckling phases from [167], too. We have analyzed a regime up to  $\eta \approx 130$  in our investigations. For small densities, we could trace the existence of the triangular monolayer  $1\Delta$ . Crossing a certain critical density  $\eta_c$  the system buckles and evolves to a trilayered structure. This transition density is also calculated analytically by applying a Taylor expansion to the lattice sum for small separations. Furthermore the evolving of the layer separation from monolayer to trilayer could be characterized as  $h(\eta) \sim (\eta - \eta_c)^{1/2}$ , qualitatively. Tuning the density upwards, we have noticed different stable bilayered structures, same as Wigner crystals. Beyond the bilayers, we could also find stable tri-, four-, five- and six-layers in square, rhombic and triangular bases. The final stability sequence for  $m > 4$  reads therefore:  $mR \rightarrow m\Delta \rightarrow (m+1)R$  with a remarkable vanish of square-based phases, where the sequence for  $m = 3$  and  $m = 4$  is  $m\Box \rightarrow mR \rightarrow m\Delta \rightarrow (m+1)\Box$ . While the stability domain of evenly layered phases gets larger with increasing  $m$ , the stability domain of square phases ( $\Box$ ) decreases for  $m > 2$  and disappears finally for  $m > 5$ . On the other hand the stability domain of rhombic ( $R$ ) and triangular ( $\Delta$ ) phases increases both with growing  $m > 2$ .

Apart of that, the transitions involved here are all of second order except  $mR \rightarrow m\Delta$  and  $m\Delta \rightarrow (m+1)\Box$ . The latter takes place discontinuously due to the order parameter  $\theta$  and particle positions (as in the case of  $nR \rightarrow n\Delta$ ) as well as with respect to  $h$  (cf. 3.7).

### 3.5 Conclusions

To summarize: For slit-confined ions in a smeared background, we have determined the ground state crystalline lattice as a function of the ion density up to the six-layer regime. A complex cascade with buckled, squared and triangular bi-, tri-, tetra-, penta- and hexalayers was found. The results are verifiable in systems with classical ions in a background including charged colloids, dusty plasmas and classical ions in a trap. One important conclusion is that the details of multilayered structures depend crucially on the particle-background interaction. More future work is needed to include wall charges, wall particle attractions and effects of finite temperature [65]. A detailed understanding of the stable crystalline structure as originating from the wall properties is desirable to construct filter devices [162] or optical band-gap crystals [171].

# Chapter 4

## Crystalline multilayers of charged colloids in soft confinement <sup>1</sup>

*We combine real-space experiments and lattice sum calculations to investigate the phase diagram of charged colloidal particles under soft confinement. In the experiments we explore the equilibrium phase diagram of charged colloidal spheres in aqueous suspensions confined between two parallel charged walls at low background salt concentrations. Motivated by the experiments, we perform lattice sum minimizations to predict the crystalline ground state of point-like Yukawa particles which are exposed to a soft confining wall potential. In the multilayered crystalline regime, we obtain good agreement between the experimental and numerical findings: upon increasing the density we recover the sequence  $2\Box \rightarrow 2\Delta \rightarrow 2\text{hcp}\perp \rightarrow 3\Box \rightarrow 3\Delta \rightarrow 3\text{hcp}\perp \rightarrow 4\Box$ .*

### 4.1 Introduction

The behavior of particles in confinement can be drastically different from that found in the bulk [17]. In particular, phase transitions like crystallization are strongly shifted or even changed in nature for strong confinement [16, 172, 173]. The type of confinement can be either topographical ("hard") or energetic ("soft"). The former case is typically modeled by hard system boundaries which influence the local packing or imprint a local substrate structure onto the system. One of the standard situations is confinement in a slit-geometry between two parallel hard plates. Soft confinement, on the other hand, results from a smooth external potential; a typical situation of which are particles confined in a harmonic well. The nature of

---

<sup>1</sup>This chapter was published in a very similar form by E. C. Oğuz, A. Reinmüller, H. J. Schöpe, T. Palberg, R. Messina, H. Löwen, *J. Phys.: Condens. Matter* **24**, (2012) 464123.

confinement needs to be distinguished from the interactions between the particles which can also be hard (as e.g. for hard spheres) or soft (as given for e.g. Yukawa-like pair interactions).

Colloidal suspensions have been used as model systems for various types of interactions and confinement [174] thanks to the tunability of their interactions [89] and the susceptibility of particles to external fields. Sterically-stabilized colloids are a realization of hard-sphere systems, while charged colloids are mainly described by Yukawa pair interactions [8,9,144]. Likewise hard and soft slit-geometry confinement can be realized by constraining the suspensions between plates. Uncharged plates provide a hard confinement while a large surface charge leads long-ranged repulsions resulting in a soft confinement. One big advantage of colloidal systems is that individual particle positions are observable directly (e.g. by video microscopy) [175] providing real-space access to crystallization phenomena [103,148,176–178]. Understanding crystallization phenomena in quasi-two-dimensional system is important not only for a fundamental understanding but also for applications like optical filters [38] and micro-sieves [39].

Regarding crystallization in slit geometry, hard confinement has been studied for both hard particles [45, 63, 64, 148–151, 170, 179–182] and soft particles [56, 58–62, 103, 152, 183–185]. More recently, also the case of hard particles in soft confinement has been addressed, see e.g. [186, 187]. Complex cascades of multilayered crystals were predicted and confirmed in colloidal experiments of which the details depend on the interparticle and particle-wall interactions. Detailed comparisons between experiment and theory were performed for hard [148, 151, 181] and soft [103] particles in hard confinement but for soft particles in soft confinement such a direct comparison is missing.

In this chapter, we close this gap and compare crystallization of soft particles in soft confinement, both by theory and experiment. In the experiments, charged colloidal spheres in a highly deionized solvent are confined between two charged glass plates. In theory, we consider point-like Yukawa interactions between the particles thereby interpolating between two known extreme limits of unscreened Coulomb particles [59, 67, 188] and hard spheres [187] in soft confinement. Focusing on multicrystalline layering, we combine both real-space studies of charged suspensions with lattice sum calculations of a Yukawa model at zero temperature in soft confinement. The comparison between the experimental data and a DLVO-type model for the interparticle and particle-wall interactions performs quantitatively well within the given uncertainties. In particular, we confirm the basic multilayer phase sequence  $2\Box \rightarrow 2\Delta \rightarrow 2\text{hcp}\perp \rightarrow 3\Box \rightarrow 3\Delta \rightarrow 3\text{hcp}\perp \rightarrow 4\Box$  if the system density increases.

This chapter is organized as follows: in section II, we discuss the experiments and present real-space data for multilayered crystals. The lattice sum calculations are briefly explained and the resulting ground state phase diagrams are compared to the experimental findings in section III and IV. We finish with concluding remarks in section V.

## 4.2 Experiments

### 4.2.1 Principles

We experimentally explored the equilibrium phase diagram of charged colloidal spheres in aqueous suspensions under spatial confinement in slit geometry at low background salt concentrations using a home-made setup. The suspensions were prepared in a closed tube system [189] including the microscopy cell, a mixed bed ion exchanger column and a syringe pump. The ion concentration was monitored using an integrated conductivity measurement cell. The arrangement of components in a circuit facilitated efficiently deionizing and homogenizing the suspensions *via* pumping. The measurement cell consisted of optically flat quartz substrates attached to piezo actuators for adjusting the confining geometry. The confined volume between the circular substrates had a lateral diameter of 25mm and was in contact with the surrounding bulk volume. A proper choice of materials of high ionic purity as well as carefully sealing the whole setup guaranteed sufficiently low contamination with salt ions. Optionally the whole setup could be enclosed into a glove bag providing a nitrogen atmosphere. Conditions were reasonably stable for more than 20 minutes each time after stopping the pump. Observations were made using a conventional inverted optical scientific microscope (Leica, DM-IRB, Germany). Two mono-disperse aqueous suspensions of negatively charged polystyrene spheres with diameters  $2a_1 = (5.19 \pm 0.08)\mu\text{m}$  and  $2a_2 = (2.59 \pm 0.04)\mu\text{m}$  (batch nos. PS/Q-F-B1036 and PS-F-B233 by Micro Particles Berlin GmbH, Germany; in the following those will be termed 'PS 5.2 $\mu\text{m}$ ' and 'PS 2.6 $\mu\text{m}$ ') were used. In order to suppress gravity the solvent mass density was matched to that of polystyrene by adding 20% vol. glycerol. Prior to the measurements the stock suspensions were in contact with mixed bed ion exchange resins for several weeks.

At constant chemical properties of both particle and substrate surfaces we investigated the equilibrium phase diagram in terms of the emerging crystal structures depending on the dimensionless parameters, namely the reduced area number density  $\eta$  and the reduced inverse screening length  $\lambda$ :

$$\eta = n_A d^2 = n_P d^3, \quad (4.1)$$

$$\lambda = \kappa d. \quad (4.2)$$

Herein  $n_A$  and  $n_P$  denote the area and volume particle number density respectively,  $d$  is the width of the confining slit, and  $\kappa$  is the inverse screening length of the assumed repulsive, screened Coulomb inter-particle potential. In our experiments these parameters could be varied and determined quantitatively.

The area number density  $n_A = N/A$  was evaluated by counting the number  $N$  of particles observed in the specified field of view  $A$  of an optical micrograph showing a well-defined phase. Counting was performed partly automated by using image analysis algorithms [190].

The separation  $d$  between the confining walls was *in situ* accessible via white light interferometry. To that end the quartz substrates were specifically coated with a beam splitting gold layer (10nm gold on 1.5nm chromium on quartz; optical transmission ca. 50%; sputtering was performed by Max Planck Institute for Polymer Research, Mainz, Germany). To induce a negative wall charge in contact with aqueous suspensions further coatings were produced in a dip procedure [191]: First the gold layer was coated with a cysteamine monolayer (Cysteamine hydrochloride by Sigma-Aldrich) that chemically bonded via a thiol group and that provided a positive surface charge. Subsequently a sodium-polystyrene sulfonate coating (Poly(sodium 4-styrenesulfonate) by Sigma-Aldrich) was produced. The latter polymeric layer provided a negative surface charge and bonded electrostatically to the cationic cysteamine layer. At wall separations below  $d \leq 50\mu\text{m}$  and at sufficiently low area number densities  $n_A$ , i.e. when the observed area  $A$  was not completely covered with particles but when there were free interstices visible between the particles, the transmitted spectrum of a white light illumination (e. g. the microscopy lamp) showed pronounced interference peaks and dips typical for Fabry-Pérot resonators. These interference patterns allowed quantitatively evaluating the local wall separation according to

$$d = \frac{c}{2n_r\Delta f} = \frac{1}{2n_r(\lambda_i^{-1} - \lambda_{i+1}^{-1})}, \quad (4.3)$$

where  $n_r$  denotes the refractive index of the suspension,  $\Delta f$  the frequency shift between two succeeding interference peaks and  $\lambda_i$  and  $\lambda_{i+1}$  the corresponding optical wave lengths.

Taking into account the particle counter ions and additional monovalent salt ions in the suspensions the bulk inverse screening length reads [189]:

$$\kappa = \sqrt{\frac{e^2}{\epsilon\epsilon_0 k_B T} (Z^* n_P + 2000 N_A c_S + 2000 N_A 10^{-7} \text{mol/l})}, \quad (4.4)$$

where  $e$  is the elementary charge,  $\epsilon\epsilon_0$  is the electrical permittivity,  $k_B T$  is the thermal energy,  $N_A$  is Avogadro's number,  $c_S$  is the salt concentration (in mol/l) and  $Z^*$  is a parameter representing an effective particle charge. The third term within the brackets describes the contribution due to autoprotolysis of water. The quantities  $c_S$  and  $Z^*$  were gathered from bulk conductivity measurements. The total conductivity  $\sigma$  reads [192]:

$$\sigma = n_P e Z^* (\mu_{H^+} + \mu_P) + 1000 N_A c_S e (\mu_{salt,+} + \mu_{salt,-}) + \sigma_{H_2O}, \quad (4.5)$$

where the first term on the right hand side describes the contribution of particles and particle counter ions, the second term describes the salt contribution and  $\sigma_{H_2O} = 0.055\mu\text{S/cm}$  (at 25°C) is the conductivity background due to autoprotolysis of water. We assume only contamination with airborne  $CO_2$  so that in this particular case, the salt cations and particle counter ions are both  $H^+$ . Otherwise, the complete

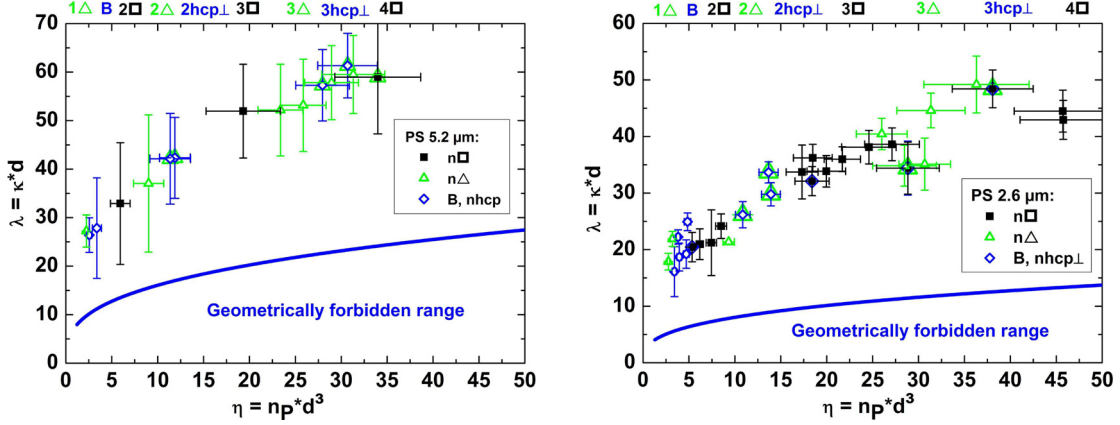


Figure 4.1: Experimentally observed crystalline equilibrium phases of charged colloidal spheres in slit confinement. (A: PS 5.2 $\mu\text{m}$ ; B: PS 2.6 $\mu\text{m}$ ; the tokens in the diagram label the data points.) See main text for further information.

formula by Hessinger et al. [192] would have to be used. The quantities  $\mu_{H^+} = 36.2 \times 10^{-8} \text{m}^2/\text{Vs}$  (in pure water at 25°C),  $\mu_P$ ,  $\mu_{\text{salt},+}$  and  $\mu_{\text{salt},-}$  are the ionic mobilities of hydrogen cations, particles, salt cations and salt anions respectively. We can identify  $\mu_{\text{salt},+} \approx \mu_{H^+}$  and  $\mu_{\text{salt},-} \approx \mu_{\text{HCO}_3^-}$  ( $= 4.6 \times 10^{-8} \text{m}^2/\text{Vs}$  in pure water at 25°C).

Laser Doppler velocimetry measurements [193] of electrophoretic particle mobilities of the PS 5.2 $\mu\text{m}$  particles revealed values in the range of  $\mu_P = 3.3 \times 10^{-8} \text{m}^2/\text{Vs} \approx 0.1 \mu_{H^+}$  for highly diluted suspensions in pure water under  $\text{CO}_2$ -saturated conditions. However, the glycerol within the suspension is expected to affect especially the mobilities  $\mu_{\text{HCO}_3^-}$  and  $\mu_P$ , which are assumed to depend inversely on the solutions viscosity. We therefore multiplied both  $\mu_{\text{HCO}_3^-}$  and  $\mu_P$  by a factor 0.56 taken from literature [194]. The parameter  $Z^*$  could be estimated from the bulk conductivity  $\sigma_0$  of the totally desalinated suspensions, i.e. when  $c_S = 0$ , under which conditions Eq. (4.5) simplifies to:

$$\sigma_0 = n p e Z^* (\mu_{H^+} + \mu_P) + \sigma_{\text{H}_2\text{O}}. \quad (4.6)$$

Under the assumption of generally small particle mobilities  $\mu_P \approx 0.05 \mu_{H^+}$ , Eq. 4.6 yields:

$$Z^* \approx \frac{\sigma_0 - \sigma_{\text{H}_2\text{O}}}{1.1 \mu_{H^+} n p e}. \quad (4.7)$$

At increased salt concentrations then from combining Eqs. (4.5) and (4.6) follows:

$$c_S = \frac{\sigma - \sigma_0}{1000 N_A e (\mu_{\text{salt},+} + \mu_{\text{salt},-})}. \quad (4.8)$$

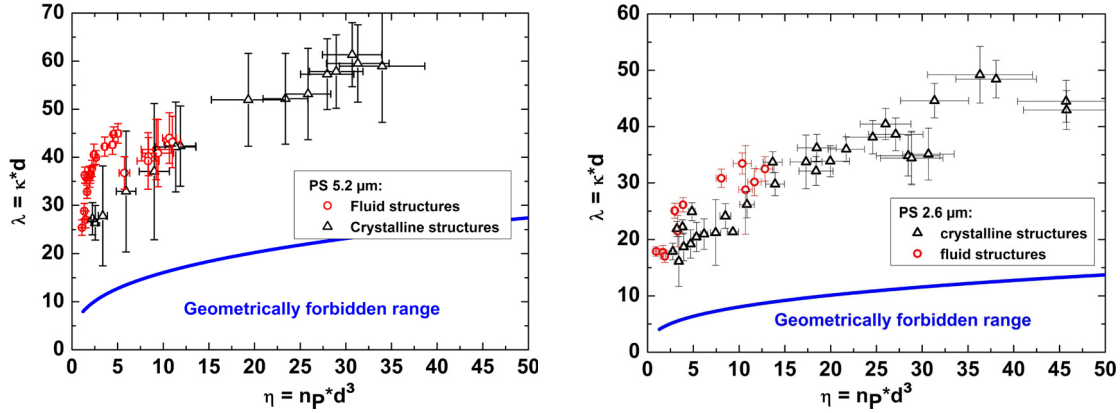


Figure 4.2: Selected data points corresponding to fluid structures (red circles) and crystalline structures (black triangles) (A: PS  $5.2\mu\text{m}$ ; B: PS  $2.6\mu\text{m}$ ).

### 4.2.2 Observations

We performed several measurement series exploring crystalline phases at salt concentrations between  $c_S \approx 0.02\mu\text{mol/l}$  and  $c_S \approx 0.3\mu\text{mol/l}$  and at volume fractions in the confined volume between  $\phi \approx 8\%$  and  $\phi \approx 10.5\%$  for the larger PS  $5.2\mu\text{m}$  particles and between  $\phi \approx 2.4\%$  and  $\phi \approx 3.6\%$  for the smaller PS  $2.6\mu\text{m}$  particles. The experiments were made at room temperature. After stopping the pump and adjusting the confining geometry both optical micrographs and transmission spectra from the local field of view were recorded at different wall separations or at different spatial positions. The wall separation was varied in a range between  $d \approx 10\mu\text{m}$  and  $d \approx 30\mu\text{m}$ . Sudden changes of  $d$  induced strong fluid currents that shear melted the existing colloidal structures. Re-formation of colloidal structures happened within typically one minute. Measurements were usually performed during time periods of less than 20min before deionizing and homogenizing the suspension was started again. Within this time period the conductivity typically increased by  $\Delta\sigma \leq 0.05\mu\text{S/cm}$  which corresponds to an increase of salt concentration of  $\Delta c_S \leq 0.15\mu\text{mol/l}$ .

In the chosen range of parameters we reproducibly observe crystalline but also a fluid phase for both species of particles. Typical in-plane nearest neighbor distances were  $d_{NN} \approx 9\mu\text{m}$  for the larger PS  $5.2\mu\text{m}$  particles and  $d_{NN} \approx 6.5\mu\text{m}$  for the smaller PS  $2.6\mu\text{m}$  particles. Phase diagrams indicating the measured crystalline data points are shown in Fig. 4.1, while additional diagrams displaying also fluid data points are given in Fig. 4.2. A selection of optical micrographs showing exemplary crystalline structures for both species of particles is given in Figs. 4.3 and 4.4.

We clearly observe a sequence of crystalline structures depending on the parameters  $\lambda$  and  $\eta$  (cf. Fig. 4.1). Basically layered structures of triangular symmetry ( $n\Delta$ )

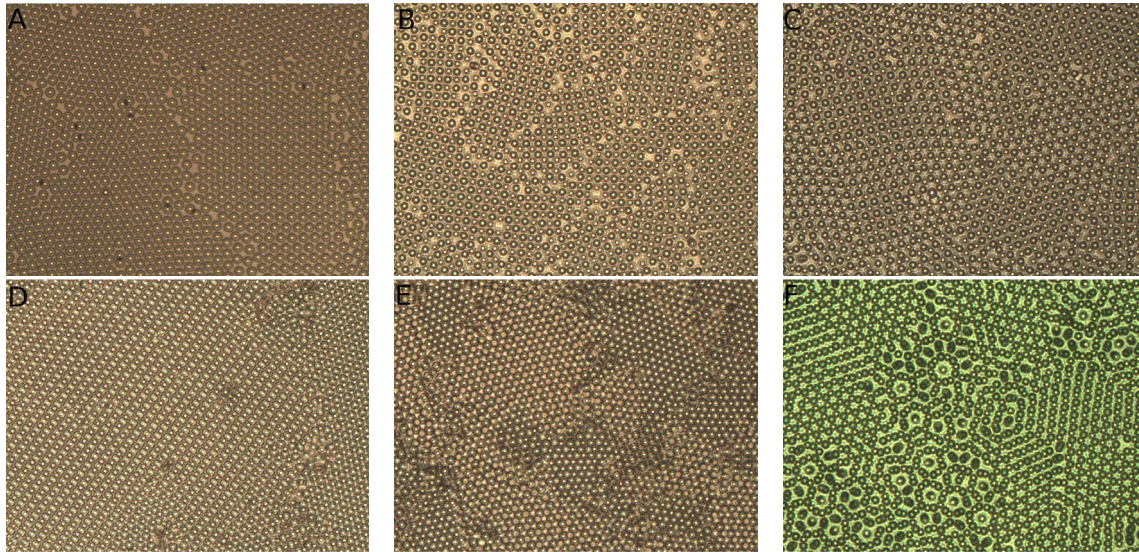


Figure 4.3: Examples of crystalline structures observed in our experiments with the larger PS  $5.2\mu\text{m}$  particles:  $1\Delta$  (A),  $2\square$  (B), coexistence of  $2\square$  and  $2\Delta$  (C),  $2\text{hcp}\perp$  (central large domain) in coexistence with  $2\Delta$  (grain at the right margin, D),  $3\Delta$  with different appearances of  $\text{fcc}(111)$  and  $\text{hcp}(001)$  faces (E) and Moiré rosettes in coexistence with  $2\text{hcp}\perp$  and  $2\Delta$  (F). (Field of view:  $280 \times 210\mu\text{m}^2$ )

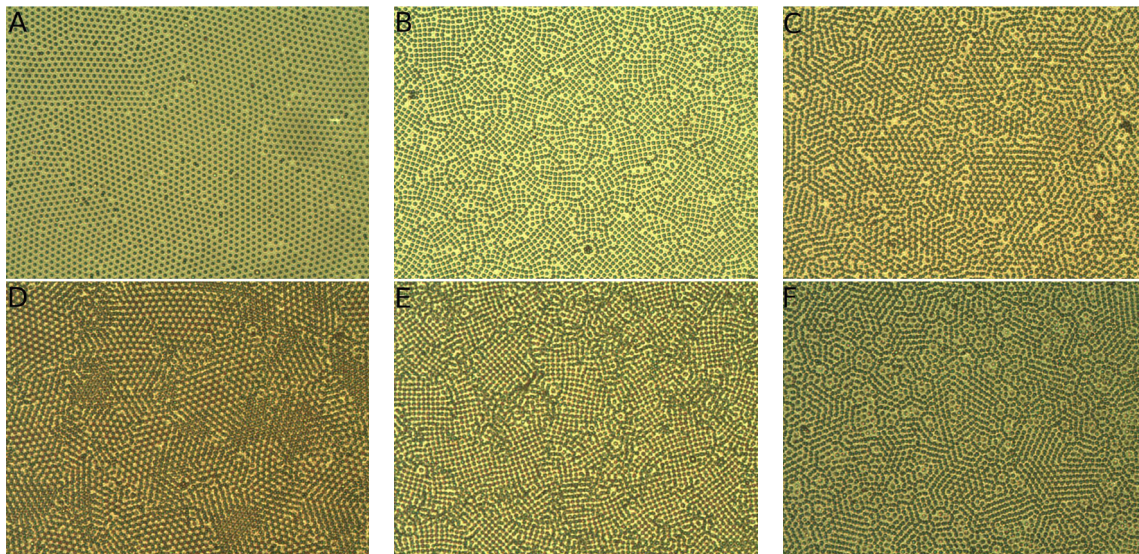


Figure 4.4: Examples of crystalline structures observed in our experiments with the smaller PS  $2.6\mu\text{m}$  particles:  $1\Delta$  (A),  $2\square$  (B),  $2\Delta$  (C),  $3\Delta$  with different appearances of  $\text{fcc}(111)$  and  $\text{hcp}(001)$  faces (D),  $4\square$  (E) and Moiré rosettes in coexistence with  $2\text{hcp}\perp$  and  $2\Delta$  (F). (Field of view:  $350 \times 265\mu\text{m}^2$ )

and square symmetry ( $n\square$ ) alternate with increasing  $d$ :

$$\dots \rightarrow n\Delta \rightarrow (n+1)\square \rightarrow (n+1)\Delta \rightarrow \dots, \quad (4.9)$$

where  $n$  denotes the number of layers. The structures  $n\Delta$  correspond to fcc-(111) or hcp-(001) faces aligned parallel to the confining walls, while the structures  $n\square$  correspond to fcc-(100) faces respectively.

Different transition structures are superimposed on the basic sequence according to Eq. (4.9). First, the buckling transition [170,180]  $B$  was frequently observed. More or less pronounced line buckling occurred, but no unconventional types of buckling [167] were evident. Secondly, structures of vertically aligned triangular layers ( $n\text{hcp}\perp$ ) [150] equivalent to hcp-(110) faces were observed. Further, coexisting with  $2\Delta$  and  $2\text{hcp}\perp$  some specific structures featuring pronounced rosette-shaped particle arrangements were observed. Those have recently been identified to be meta-stable Moiré rotation patterns consisting of two unconventionally stacked triangular monolayers [62]. These structures formally correspond to  $1 \times 1R\alpha$  superstructures, where  $\alpha$  denotes discrete rotation angles. In summary the whole observed experimental sequence reads (without the transient Moiré-patterns):

$$1\Delta \rightarrow B \rightarrow 2\square \rightarrow 2\Delta \rightarrow 2\text{hcp}\perp \rightarrow 3\square \rightarrow 3\Delta \rightarrow 3\text{hcp}\perp \rightarrow 4\square. \quad (4.10)$$

The range containing the observed crystalline phases is bordered by a geometrically forbidden range, where particle number densities exceed the maximum packing limit, and the region of fluid structures (cf. Fig. 4.2). The borderline (blue lines) of the geometrically forbidden range was estimated assuming a constant maximum volume fraction of  $\phi = 60\%$  in the confining slit and a minimum total ion concentration  $c = 2 \times 10^{-7} \text{ mol/l}$  neglecting particle counter ions and salt ions. Reasonably, fluid structures were observed at larger  $\lambda$ , i.e. at weaker particle interactions, with respect to crystalline structures.

Fluid structures in the regime of more than two layers as well as crystalline phases with more than 4 layers were not evaluated quantitatively. Too large area number densities  $n_A$  did not allow measurements of the wall separation  $d$  nor of the locally observed particle numbers  $N$  due to too many visually overlapping particles. Further, particle fluctuations made structures more difficult to identify, and sufficiently large crystalline grains did not form within a reasonable time period.

The formation of monolayer and bi-layer crystals typically occurred quasi-instantaneously within 10s, while systems with more layers required longer times to emerge. On timescales of about 5min slow changes of morphology were observed that did not affect the crystalline structures. Defects were annealed as well as grain boundaries slowly vanished by diffusive particle rearrangement. Further long-term relaxation processes of the system were observed on time-scales of 20min. A slow decrease of the local particle number density  $n_P$  in the confined suspension occurred which induced an increase of crystal lattice constants and even led to melting of

crystalline structures. This temporary loss of particles during measurements is presumably due to a difference between the chemical potentials of confined and bulk suspensions. This was the main obstacle to long time measurements. The original values  $n_P$  could afterwards be restored *via* homogenizing.

Major error sources in our experiments are inexact particle counting, weak interferometric contrast in estimating  $d$ , salt contaminations and thermal effects. The former two are considerable especially for more than two particle layers, when many particles are visually overlapping due to the large particle diameter  $2a$  with respect to their typical distance  $d_{NN} \approx 1.5 - 2.5 \times 2a$ . Salt contaminations are always present and more significant for lower overall salt concentrations. Further uncertainty arises from the fact, that conductivity could not be measured in situ, but only apart from the confinement cell in bulk. Local ion sources, like e. g. tiny fragments of ion exchange resins [195], cannot generally be excluded. But it is also not *a priori* clear, how wall counter ions affect the local ion concentration and thus the local inter-particle interactions. This might give rise to systematic errors that were not further considered. Thermal effects, e.g. induced by the microscopy illumination, might appear as local thermal gradients. Thermogradients may influence particle concentrations by thermophoresis. Of more interest probably would be local changes of the particle interaction. The dependence is complex but can be assumed small [196]. Carefully estimated error bars are indicated in Figs. 4.1 and 4.2.

## 4.3 Theory

### 4.3.1 The model

We consider  $N$  point-like particles interacting *via* a Yukawa pair-potential

$$V(r) = V_0 \frac{\exp(-\kappa r)}{\kappa r}, \quad (4.11)$$

where  $r$  is the interparticle distance and  $V_0$  denotes an energy amplitude. For charged suspensions, this interaction amplitude is given within DLVO theory [11, 12] as

$$V_0 = \frac{Z^{*2} e^2 \kappa}{4\pi\epsilon_0\epsilon} \left( \frac{\exp(\kappa a)}{1 + \kappa a} \right)^2 \quad (4.12)$$

where  $a$  denotes the physical hard core radius of the particles and  $\epsilon$  is the dielectric permittivity of the solvent. We further invoke linear screening theory to describe the wall-particle interaction by the confining potential [197]

$$V_c(z) = W_0 \cosh(\kappa z), \quad (4.13)$$

with  $z$  denoting the direction perpendicular to the plates. The amplitude  $W_0$  is given by (see e.g. [8, 57, 58, 197, 198])

$$W_0 = \frac{2Z^* e^2}{\epsilon_0\epsilon} \sigma_w \frac{\exp(\kappa a)}{\kappa(1 + \kappa a)} \exp(-\lambda/2), \quad (4.14)$$

Using the interaction potentials above, we performed lattice sum minimizations to obtain the stability phase diagram at zero-temperature, as explained and discussed in the following.

### 4.3.2 Lattice Sum Minimization

We performed lattice sum minimizations for a broad set of candidates of crystalline lattices. Here, we focus on the nontrivial multilayer regime beyond the stability of the squared bilayer  $2\Box$  phase. For fixed  $\lambda$ , a sufficient increase of the reduced density yields the squared tetralayer structure  $4\Box$ . The precise goal of our work is to figure out the corresponding regime between  $2\Box$  and  $4\Box$  by investigating the stability of intervening crystalline multilayers.

For our lattice sum minimization problem the possible candidates are three-dimensional crystals with two-dimensional periodicity in  $x$ - and  $y$ -direction and a finite extension in the  $z$ -direction. The primitive cell of these candidates is a parallelepiped containing  $k$  particles and its  $xy$ -basis (which is a parallelogram) is spanned by the two lattice vectors  $\mathbf{a} = a(1, 0)$  and  $\mathbf{b} = a\gamma(\cos \theta, \sin \theta)$ , where  $\gamma$  is the aspect ratio ( $\gamma = |\mathbf{b}|/|\mathbf{a}| = b/a$ ) and  $\theta$  is the angle between  $\mathbf{a}$  and  $\mathbf{b}$ . Furthermore the  $k$  particles are distributed, not necessarily evenly, on  $n$  layers in the  $xy$ -plane. Hereby we restrict ourselves to layered situations with an up-down inversion symmetry in the averaged occupancy reflecting the up-down symmetry of the confining external field. Under this restriction, we consider possible candidates with  $k = 2, \dots, 6$  and  $n = 1, \dots, 6$  (up to symmetric six-layer structures with a basis of up to 6 particles). At prescribed system parameters, the total potential energy per particle is minimized with respect to the particles' coordinates of the cell and its geometry ( $\gamma$  and  $\theta$ ).

### 4.3.3 Matching the model parameters to the experiments

This chapter aims at a direct comparison between the theoretical results and the experimental ones so that a quantitative analysis naturally requires the knowledge of the two intrinsic energy scales  $V_0$  and  $W_0$  of the system. Hence, the phase behaviour depends not only on the system density but also on the ratio  $W_0/V_0$ . Therefore we introduce the surface charge ratio  $v = \sigma_w/\sigma_p = \sigma_w/(Z^*/4\pi a^2)$  ( $v > 0$ ), between the wall and the spheres. In order to implement experimental conditions into our lattice sum calculations, we need to consider the following parameters:  $Z^*, \epsilon, \kappa, a, v, d, n_P, T$ . In fact, the effective charge  $Z^*$  of the colloid-colloid interaction as well as the solvent permittivity  $\epsilon$  scale out at zero temperature ( $T = 0$ ) for the colloids. Hence, at prescribed  $\lambda = \kappa d$  and  $\eta = n_P d^3$  the only relevant parameters are  $\kappa, a$  and  $v$ .

Our primary goal is to predict the theoretical phase diagrams for large ( $a = 2.6\mu\text{m}$ ) and small ( $a = 1.3\mu\text{m}$ ) particles. Thereby with  $\kappa \approx 1.5 - 3.0/\mu\text{m}$  we use averaged values of  $\kappa$  resulting in  $\kappa a = 6$  ( $\kappa a = 3$ ) for PS  $5.2\mu\text{m}$  (PS  $2.6\mu\text{m}$ ) particles.

Next we estimate the surface charge ratio  $v$  which enters into the particle-wall interaction (4.14). One has to keep in mind that, though the bare wall surface charge density is pretty high, the colloidal particles feel the wall only at large distances where most of the wall charge has been nonlinearly screened and the linear-screening-regime has been reached. Actually what enters into Eq. (4.14) is not the bare surface charge density but an *effective* surface charge density [8]. The latter can be brought into relation to the bare charge density via the exact Gouy-Chapman solution of the nonlinear Poisson-Boltzmann equation as worked out by von Grünberg and coworkers [199]. Using the procedure described in Ref. [199] a strong reduction of the bare wall charge to an effective wall charge is achieved.

In detail, the bare wall charge density can be estimated by the assumption that the polyelectrolytes form a dense monolayer on the walls with a molecular area density of  $\sim 1/\pi r_g^2$  where the radius of gyration  $r_g$  is taken to be that in the concentrated solution used at coating. Under experimental conditions, the polyelectrolyte molecules will stretch to yield a bare charge density on the order of the molecular density. For the experimentally used polyelectrolyte-coating we therefore estimate the real charge density of the walls as  $(4 \pm 1) \times 10^{-3}/\text{nm}^2$ . Following the procedure given in Ref. [199], the effective wall charge density is reduced towards  $0,7 - 1,2 \times 10^{-3}/\text{nm}^2$ . On the other hand, the effective surface charge density on the colloidal spheres is typically about  $2,4 \times 10^{-3}/\text{nm}^2$  ( $2,0 \times 10^{-3}/\text{nm}^2$ ) for  $5,2\mu\text{m}$  ( $2,6\mu\text{m}$ ) particles such that  $v$  becomes roughly  $0,3 \leq v \leq 0,5$  ( $0,4 \leq v \leq 0,6$ ) for  $5,2\mu\text{m}$  ( $2,6\mu\text{m}$ ) particles. In the following we have chosen  $v = 0,4$  which leads to a good agreement between theory and experiments. Moreover, as our theoretical analysis shows, a different choice of  $v$  in the range  $0,1 < v < 0,5$  does not significantly change the theoretical data such that the comparison is fortunately quite insensitive to the actual choice of  $v$ .

#### 4.3.4 Ground state phase diagrams and comparison to experiments

At zero temperature, for a given reduced density  $\eta$ , the system will minimize its total potential energy, and the resulting optimal ground state structure will solely depend on the reduced inverse screening length  $\lambda = \kappa d$ . Under consideration of the system at hand, the calculations have been performed for  $5,2\mu\text{m}$  and  $2,6\mu\text{m}$  particles and the corresponding phase diagrams are drawn in Figs. 4.5 and 4.6.

We explore the stability phase diagram for  $0 < \lambda \leq 70$  and  $0 < \eta \leq 50$  and we investigate the structural transitions between the phases  $2\Box$  and  $4\Box$ . Thereby, we obtain several multilayered crystalline phases with rhombic ( $R$ ), triangular ( $\Delta$ ), quadratic ( $\Box$ ) and rectangular (hcp – like, hcp $\perp$ ) symmetry. In the transition regime  $2\Box \rightarrow 4\Box$  there are not only bilayered ( $2R$ ,  $2\Delta$ ) and trilayered ( $3\Box$ ,  $3R$ ,  $3\Delta$ ) phases evident, even we further notice the stability of tetralayered (2hcp – like,

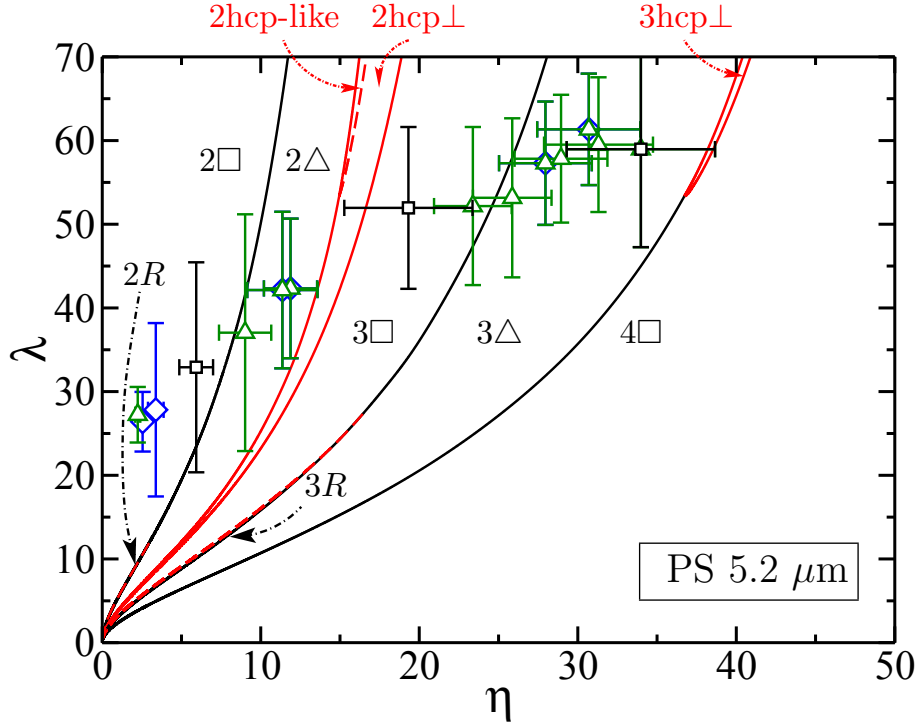


Figure 4.5: Comparison of the theoretical prediction (dashed and full lines) for the multilayer stability phase diagram at zero temperature to the experimental data (tokens) taken from the phase diagram for PS  $5.2\mu\text{m}$  particles in Fig. 4.1A. Here, we use  $\kappa a = 6$  and  $v = 0.4$ . Please note that symbols for experimental data are as in Fig. 4.1. See main text for further information.

$2\text{hcp}\perp$ ) as well as a hexalayered ( $3\text{hcp}\perp$ ) phase.

Both the rhombic phases  $2R$  and  $3R$  display a tiny stability regime, which are indicated by the red dashed lines in Figs. 4.5 and 4.6 and which vanish above a certain threshold of  $\lambda$ . The phases  $\text{hcp}$  – like,  $\text{hcp}\perp$  and  $3\text{hcp}\perp$ , which become stable for  $\lambda \gtrsim 51.9$  ( $\lambda \gtrsim 59.6$ ) for PS  $5.2\mu\text{m}$  (PS  $2.6\mu\text{m}$ ) particles, are derivable from the  $\text{hcp}$  lattice as recently discussed in [149, 150]. We further remark that the stacking sequence of  $3R$  ( $3\Delta$ ) consists of the  $ABA$  ( $ABC$ ) one. In all resulting structures the size ratio of the lattice vectors equals unity ( $\gamma = 1$ ) except for  $2\text{hcp}$  – like,  $2\text{hcp}\perp$  and  $3\text{hcp}\perp$ . In this case,  $\gamma$  is larger than 1 due to its rectangular basis shape.

Clearly, for relatively small  $\lambda$ , the phase diagram reveals the following phase cascade interpolating between  $2\Box$  and  $4\Box$ :

$$2\Box \rightarrow 2R \rightarrow 2\Delta \rightarrow 2\text{hcp}\perp \rightarrow 3\Box \rightarrow 3R \rightarrow 3\Delta \rightarrow 4\Box. \quad (4.15)$$

However, for relatively large reduced inverse screening length we notice the stability of rhombic phases  $2R$  and  $3R$  to vanish and the stability of  $2\text{hcp}$  – like and  $3\text{hcp}\perp$  to arise yielding the following stability sequence

$$2\Box \rightarrow 2\Delta \rightarrow 2\text{hcp}\text{ – like} \rightarrow 2\text{hcp}\perp \rightarrow 3\Box \rightarrow 3\Delta \rightarrow 3\text{hcp}\perp \rightarrow 4\Box. \quad (4.16)$$

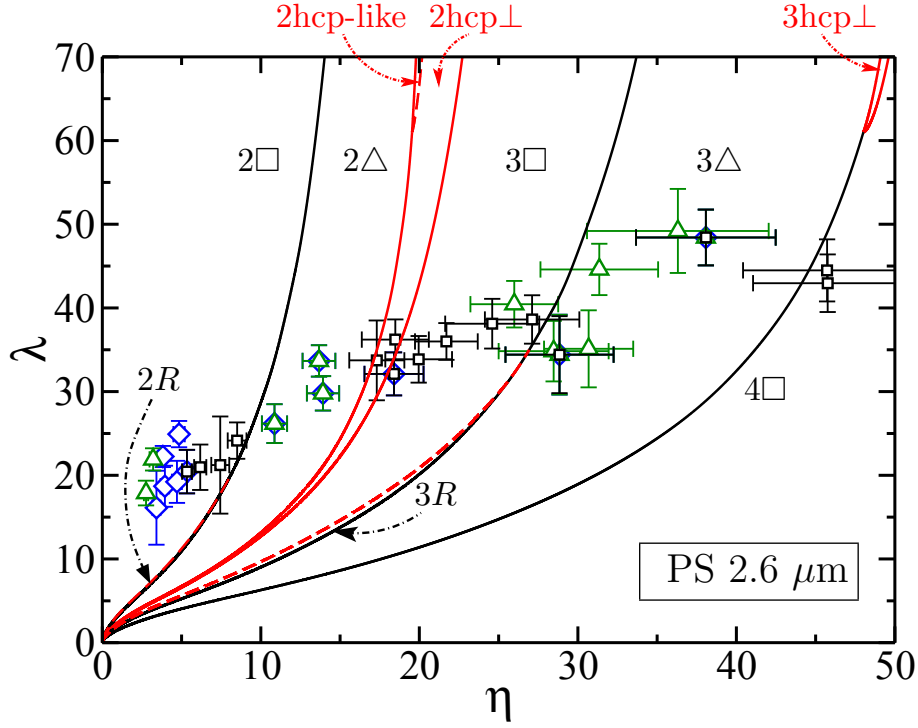


Figure 4.6: Same as in Fig. 4.5 for PS  $2.6\mu\text{m}$  particles (with  $\kappa a = 3$  and  $v = 0.4$ ).

Regarding the order of the transitions, both, first- and second-order transitions occur and are indicated by solid and dashed transition lines in Figs. 4.5 and 4.6, respectively. Second-order transitions are  $n\Box \rightarrow nR$  for  $n = 2, 3$  and  $2\text{hcp-like} \rightarrow 2\text{hcp}\perp$ , whereas all remaining transitions exhibit discontinuous paths in at least one of the order parameters  $\theta$  and/or  $\gamma$ .

## 4.4 Discussion

The charged walls in the experiments lead to a soft exponentially screened wall-particle interaction which we implicitly considered by the effective external field given by the Eq. 4.12 in our theoretical model. However, we did not take the hard-core part of the walls into account explicitly there. This can be justified by the wall charge density which was high enough to keep particles well separated from the walls and prevent a sticking to those. Besides, the experiments being realized in the low screening regime, the particles are not touching each other so that the pair potential from Eq. 4.11 without explicit hard-core interaction is reasonable for the effective colloid-colloid interaction.

We achieve a good quantitative agreement between the theoretical and experimental phase diagrams (cf. Figs. 4.5 and 4.6). The stability domains of the experimentally found phase structures coincide well with the corresponding phase

boundaries obtained by lattice sum calculations. However, the stability domains of  $nhcp\perp$  phases might be slightly off the theoretically predicted ones (especially for large particles and  $3hcp\perp$ ).

The phase diagrams for both the PS  $5.2\mu\text{m}$  and the PS  $2.6\mu\text{m}$  particles (cf. Figs. 4.1A,B) are in qualitative agreement, but they do not match quantitatively. For the larger particles the fluid region is located at significantly larger values  $\lambda$  at given  $\eta$ , while crystalline structures are also shifted to smaller values  $\eta$ . These discrepancies might be attributed to the experimental non-zero particle size.

Comparing our results with those from similar experiments performed previously by van Winkle and Murray [200] shows qualitative agreement in the basic sequence of crystal structures with increasing  $d$  (cf. Eq. 4.9) together with the buckling transition  $B$ . However, particle interactions have not been specified there. Their phase diagram is rather determined by geometric parameters only.

Comparison of our experimental results under strongly deionized conditions with those from wedge confinement experiments in the strongly screened limit [103, 179] also shows agreement in the basic sequence (cf. Eq. 4.9) together with the transition phases  $B$  and  $nhcp\perp$ . But we here do not observe crystalline prism phases [148, 151] ( $nP$ ) nor do we have clear evidence of rhombic phases [59, 170, 180] ( $nR$ ). Theory [60] suggests that prism phases are predominantly stable in strongly screened suspensions, but not at weak screening as it is the case here. In fact, prism phases have frequently been observed experimentally in the strongly screened limit [103, 148]. The prism phases apparently possess more particles in the outer layers than in the inner ones [60, 148, 151]. Since the outer particles cause energy loss due to the external field, absence of the prism phases is not surprising. Even for higher densities  $\eta$ , we expect the multilayering scenario to favor phases that have more or comparable weights in the inner layers as in the outer ones.

Theory further predicts that rhombic phases should especially occur in the transitions

$$n\Box \rightarrow nR \rightarrow n\Delta \tag{4.17}$$

for  $n = 2, 3, 4$  [59]. The absence of clear evidence of rhombic phases in the experiments might be explained by ground state stability arguments (cf. the theoretical phase diagrams in Figs. 4.5 and 4.6): The stability domains each of  $2R$  and  $3R$  are too tiny. In these transition regions we rather observe coexisting  $n\Box$  and  $n\Delta$  structures in the experiments. Interestingly, for  $n = 2$  crystallites of  $2\Box$  and  $2\Delta$  favor commensurate instead of disordered grain boundaries (cf. Fig. 4.3C). Hence, lattice distortions occur in order to reduce grain boundary energy, which give rise to regions of rhombically ordered particles. But it remains unclear whether those are equilibrium structures or morphologically induced, meta-stable structures. Further discrepancies between the experimental phase diagrams (Figs. 4.1, 4.2) and theoretical ground state phase diagrams (Figs. 4.5, 4.6) might be attributed to finite temperature effects.

## 4.5 Conclusions

In conclusion, we have compared real-space data for the crystallization of charged colloids in soft confinement with zero-temperature lattice-sum calculations of a Yukawa system in a soft wall potential as predicted by linear screening theory. We found quantitative agreement and have confirmed the basic multilayer phase sequence

$$2\Box \rightarrow 2\Delta \rightarrow 2\text{hcp}\perp \rightarrow 3\Box \rightarrow 3\Delta \rightarrow 3\text{hcp}\perp \rightarrow 4\Box$$

as the system density increases. As one of the essential input parameters, the quantitative comparison needed the surface charge density ratio  $v$  of the walls and the particles. This ratio was chosen to be smaller than unity implying that the walls are effectively less charged than the colloidal particles. The good comparison shows that the linearized theory is applicable to confined charged colloids and that most of the physics is contained in an effective pairwise potential model with soft interactions.

We further obtained first- and second-order phase transitions in the ground state phase diagrams (Figs. 4.5 and 4.6) which are shown by solid and dashed transition lines in Figs. 4.5 and 4.6, respectively.

In future work, more subtle effects should be considered on the theoretical side which could improve the comparison. Possibilities include a finite excluded-volume core of the colloids, finite temperature of the particles [76], charge polydispersity of the suspensions [201], as well as image charges resulting from the jump in the dielectric permittivity from the aqueous solution to the wall [57]. On the experimental side, to overcome the above described restrictions of small accessible layer numbers and small accessible ranges of  $n_P$  new experiments can be performed with suspensions providing  $d_{NN}/2a \gg 2$ , e. g. using suspensions of comparably interacting, but smaller particles. Also confocal microscopy can be used to provide a better three-dimensional structure analysis in similar experiments.

We expect further interesting new physics of a multicrystalline layer that is sheared. Shear flow would promote alignment effects and could lead to novel reentrant behaviour [76, 202–205]. It would further be interesting to study a patterned or curved wall which would introduce a new length scale to the confined crystalline layer leading to novel elastic response of the crystalline sheet as pointed out in various recent investigations [206–208].



# Chapter 5

## Packing confined hard spheres denser with adaptive prism phases 1

*We show that hard spheres confined between two parallel hard plates pack denser with periodic adaptive prismatic structures which are composed of alternating prisms of spheres. The internal structure of the prisms adapts to the slit height which results in close packings for a range of plate separations, just above the distance where three intersecting square layers fit exactly between the plates. The adaptive prism phases are also observed in real-space experiments on confined sterically stabilized colloids and in Monte Carlo simulations at finite pressure.*

How to pack the largest number of hard objects in a given volume is a classic optimization problem in pure geometry [209]. The close-packed structures obtained from such optimizations are also pivotal in understanding the basic physical mechanisms behind freezing [210, 211] and glass formation [212]. Moreover, close-packed structures are highly relevant to numerous applications ranging from packaging macroscopic bodies and granulates [213] to the self-assembly of colloidal [214] and biological [215, 216] soft matter. For the case of hard spheres, Kepler conjectured that the highest-packing density should be that of a periodic face-centered-cubic (fcc) lattice composed of stacked hexagonal layers; it took until 2005 for a strict mathematical proof [217]. More recent studies on close packing concern either non-spherical hard objects [218] such as ellipsoids [219, 220], convex polyhedra [221, 222] (in particular tetrahedra [223]), and irregular non-convex bodies [224] or hard spheres confined in

---

<sup>1</sup>This chapter was published in a very similar form by E. C. Oğuz, M. Marechal, F. Ramiro-Manzano, I. Rodriguez, R. Messina, F. J. Meseguer, H. Löwen, *Phys. Rev. Lett.* **109**, (2012) 218301.

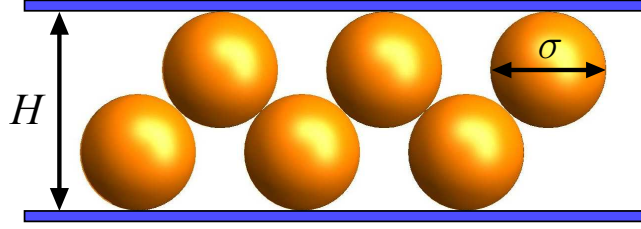


Figure 5.1: Schematic illustration of hard spheres of diameter  $\sigma$  confined between two parallel hard plates of separation  $H$ .

hard containers [45, 225, 226] or other complex environments.

If hard spheres of diameter  $\sigma$  are confined between two hard parallel plates of distance  $H$ , as schematically illustrated in Fig. 5.1, the close-packed volume fraction  $\phi$  and its associated structure depend on the ratio  $H/\sigma$ . Typically, the complexity of the observed phases increases tremendously on confining the system. Parallel slices from the fcc bulk crystal are only close-packed for certain values of  $H/\sigma$ : A stack of  $n$  hexagonal (square) layers aligned with the walls, denoted by  $n\Delta$  ( $n\square$ ), is best-packed at the plate separation  $H_{n\Delta}$  ( $H_{n\square}$ ) where the layers exactly fit between the walls. Clearly, for the minimal plate distance  $H \equiv H_{1\Delta} = \sigma$ , packing by a hexagonal monolayer is optimal. Increasing  $H/\sigma$  up to  $H_{2\Delta}$ , a buckled monolayer [179] and then a rhombic bilayer [170, 180] become close-packed. However, for  $H_{2\Delta} < H < H_{4\Delta}$ , the close-packed structures are much more complex and still debated. Both, prism phases with alternating parallel prism-like arrays composed of hexagonal and square base [148, 151] and morphologies derived from the hexagonal-close-packed (hcp) structure [149, 150] were proposed as possible candidates.

For confined hard spheres, the knowledge and control over the close-packed configuration is of central relevance for at least two reasons: First, the hard sphere system away from close-packing is of fundamental interest as a quasi-two-dimensional statistical mechanics model. At low densities, a hard sphere gas is stable, which will crystallize as the density is increased beyond some threshold value. As such, the model represents a classical route to understand freezing between two and three spatial dimensions [227]. The associated fluid–solid transition will be strongly affected by the close-packed structure. Second, the confined hard sphere model is almost perfectly realized in nature by mesoscopic sterically-stabilized colloidal suspensions [148, 181] which can be confined between glass plates providing a slit-like confinement. At high imposed pressures, colloids will self-assemble into the close-packed structures. It has been shown that this is the key for the controlled fabrication of nano-sieves and of membranes with desired morphology [39].

In this chapter, we explore the close-packed structures of confined hard spheres by combining numerical optimization, experiments and computer simulation. Using

a systematic penalty optimization method, we find the whole cascade of close-packed structures in the range of plate distances  $H_{1\Delta} < H < H_{4\Delta}$ . As an important building block for close-packing, an *adaptive* prism is identified which adjusts its internal structure flexibly to the slit height  $H/\sigma$ . This prism has a base with a rhombic symmetry and neighboring prismatic arrays are shifted relative to each other. The resulting adaptive structure maximizes the packing fraction in the regime beyond  $H_{3\Box}$ . We also propose a further close-packing prism phase of square symmetry that packs densest in the regime just beyond  $H_{4\Box}$  and shows a two-dimensional relative lateral shift between the prisms. We confirm the stability of the new adaptive prismatic structures both in real-space experiments on confined sterically stabilized colloids and in Monte Carlo simulations at finite pressure. In the following, we first describe the results from the penalty method, then discuss real-space data for confined colloidal samples and subsequently turn to Monte Carlo simulation results.

In our numerical calculations, we considered a broad set of candidates of crystalline lattices thereby covering all hitherto proposed structures. For confined hard spheres, the possible candidates are three-dimensional crystals with two-dimensional periodicity in the plane parallel to the confining plates. We assumed the primitive cell of these candidates to be a parallelepiped containing  $k$  particles which are distributed, not necessarily evenly, on  $n$  layers. For  $k > 4$ , we restricted ourselves to layered situations with an up-down inversion symmetry in the averaged occupancy reflecting the up-down symmetry of the confining walls. Under this sole restriction we took into account possible candidates with  $k = 1, \dots, 8$  and  $n = 1, \dots, 6$ . In addition, we included the unusual asymmetric buckling phases as reported in [167, 228, 229] into our candidate set, which break the up-down symmetry of the confining slit. To maximize the packing fraction  $\phi$ , we optimized the cell shape and the particle coordinates of these structures. However, investigating the dense-packing of hard spheres accommodates a constrained optimization: the free volume must be minimized under the constraint of non-overlapping spheres. To circumvent the discontinuous, constrained optimization, we employed the *penalty method* [230] in our numerical calculations. By adding a penalty term in case the spheres intersect which depends continuously on the overlap volume, we obtained a continuous and unconstrained penalty function which can be minimized in the classic way to predict the optimal particle coordinates<sup>2</sup>. For higher layer and particle numbers,  $n \geq 6$  and  $k > 8$ , however, the optimization process offered difficulties due to large number of involved parameters. Hence, we fixed the particles within the prisms and we optimized their basis symmetry. Additionally, we adjusted the relative positions of the prisms and the vectors that span the unit cell for the prism phases with  $k = 12$ . Please also note that denser packed structures could occur with larger unit cells. However, the number of particles in each unit cell are sufficiently

---

<sup>2</sup>The penalty method offers the flexibility to use a relatively broad range of candidate crystalline lattices and has recently been shown to allow a very efficient handling of packing problems [231].

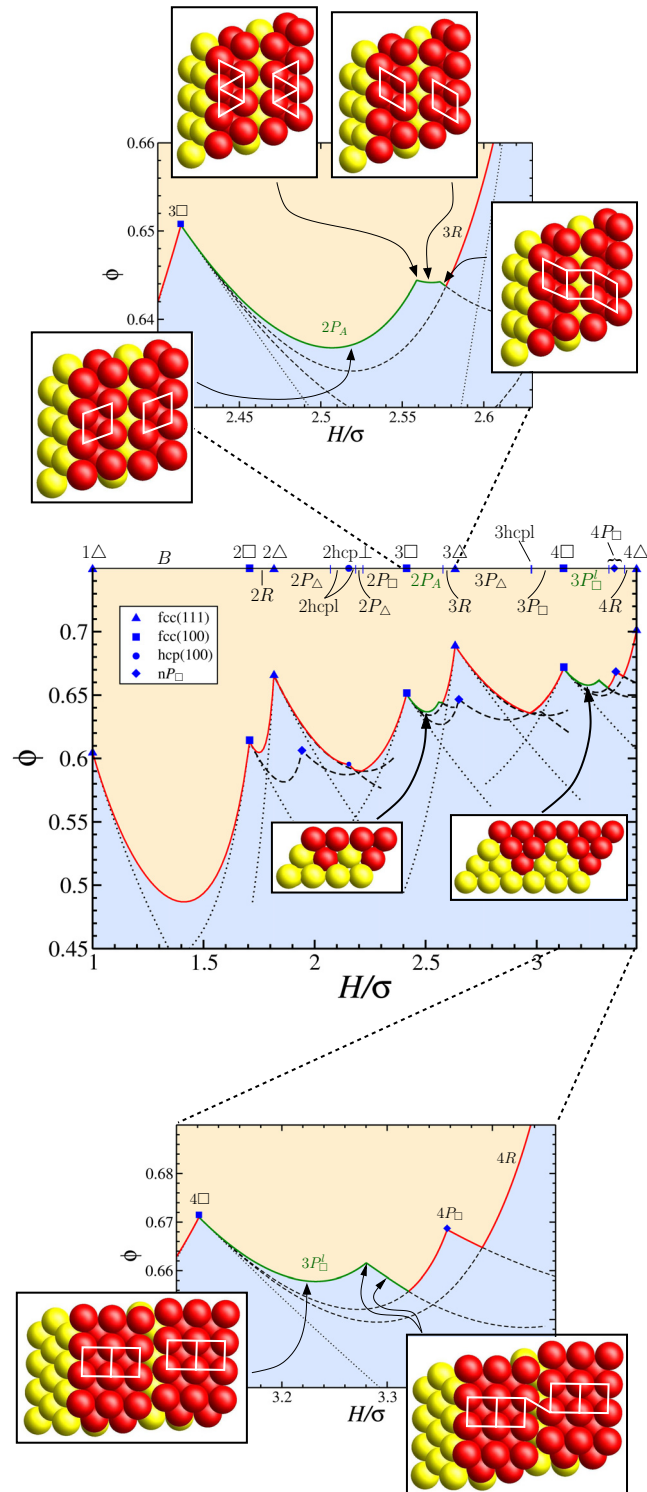


Figure 5.2: Packing fraction  $\phi$  versus dimensionless height  $H/\sigma$ . The best-packing phases are indicated by symbols on the top axis of the middle panel and their packing fractions are shown as the full lines. For clarity, the regions below and above the best packing are colored differently. The new prism phases are denoted by green lines. Dashed and dotted lines denote the non-close packed  $n\Box$  [fcc(100)],  $n\Delta$  [fcc(111)],  $nhcpl$ ,  $nP_\Delta$  and  $nP_\Box$ . The top and bottom panel show enlargements of the regions where the new prism phases were found. Side views (middle panel) and top views (top and bottom panels) show the structure of these phases, where white lines denote bonds between touching particles.

large to obtain all hitherto proposed structures.

The resulting volume fractions of the densest packed phases are shown in Fig. 5.2 as a function of  $H/\sigma$  in the regime between the hexagonal monolayer  $1\Delta$  ( $H/\sigma = 1$ ) and the triangular tetralayer  $4\Delta$  ( $H/\sigma = \sqrt{6} + 1$ ). For  $H_{1\Delta} < H < H_{2\Delta}$  the classic sequence [61, 170, 179, 180]  $1\Delta \rightarrow B \rightarrow 2\Box \rightarrow 2R \rightarrow 2\Delta$  is confirmed. Here,  $B$  is a buckled hexagonal layer with rectangular symmetry and the  $2R$  crystal consist of two staggered rhombic layers.

For  $H_{2\Delta} < H < H_{4\Delta}$ , there is a much more complex cascade of close-packed structures. In the transition regime  $n\Delta \rightarrow (n + 1)\Box$  for  $n = 2, 3$ , on the one hand, we recover all of the phases found previously. Here, we obtain the sequence  $2\Delta \rightarrow 2P_\Delta \rightarrow 2\text{hcp}\perp \rightarrow 2\text{hcp}\perp \rightarrow 2\text{hcp}\perp \rightarrow 2P_\Box \rightarrow 3\Box$  and  $3\Delta \rightarrow 3P_\Delta \rightarrow 3\text{hcp}\perp \rightarrow 2P_\Box \rightarrow 3\Box$ , where the following phases are encountered: The  $2n$ -layered phases  $nP_\Delta$  and  $nP_\Box$  consist of alternating prism-like dense-packed  $n$ -layered arrays of spheres with triangular ( $\Delta$ ) and square ( $\Box$ ) basis shapes ([148, 151, 181]). Moreover, the  $2n$ -layered phases  $n\text{hcp}\perp$ <sup>3</sup> and  $n\text{hcp}$ -like with rectangular symmetry (see [149, 150]) are found. For  $n = 3$ , however, the  $n\text{hcp}$ -like phase is only close-packed in a tiny regime, whereas  $n\text{hcp}\perp$  is not found at all (see Fig. 5.2).

In the range  $3\Box \rightarrow 3\Delta$ , the new adaptive prism phase  $2P_A$  is predicted to be close-packed. Representative intra-layer touching bonds are indicated by white lines in Fig. 5.2 (upper and lower panel) to underline the symmetry of the corresponding prismatic structure. The  $2P_A$  phase adapts its internal structure flexibly to an increase of the slit width  $H$ . In fact, the symmetry of its prism blocks is rhombic which spans the whole range between the square symmetry of the underlying phase  $3\Box$  and the triangular base (see white lines in Fig. 5.2, upper panel). Likewise, we noticed the stability of the  $3P_\Box^l$  prism phase with square basis shape (cf. Fig. 5.2, lower panel) in the transition regime  $4\Box \rightarrow 4\Delta$  whose prisms exhibit a longitudinal shift (ie. in the lengthwise direction of the prisms) in addition to the usual shift perpendicular to the lengthwise direction of the prisms. Finally, the other densest packed phases are multilayered rhombic phases  $3R$  and  $4R$  as well as a square prism phase  $4P_\Box$  see Fig. 5.2.

To verify our theoretical results, we performed real-space experiments with nanometer-sized colloids. We employed Polystyrene particles with diameters  $\sigma$  in the range from 245 nm to 800 nm (Ikerlat Polymers) to study a certain of  $H/\sigma$  values. We created a confining wedge cell with a very small opening angle ( $10^{-4}$  rad) and slit height  $H < 6\mu\text{m}$ . The varying slight height inherent to the wedge geometry allows many transitions between different crystals in the same cell. In our wedge cell, we used hydrophilic treated glass as substrate (3 cm large) and hydrophobic polystyrene as covering plate. We attached a 6  $\mu\text{m}$  thick Mylar film along just one rim of the slides to separate the plates of the wedge cell. We tightened the cells with several binder

---

<sup>3</sup>This phase structure corresponds to the (100) plane of the hexagonal close-packed solid and, therefore, it is referred to as  $n\text{hcp}(100)$  in Ref. [149]

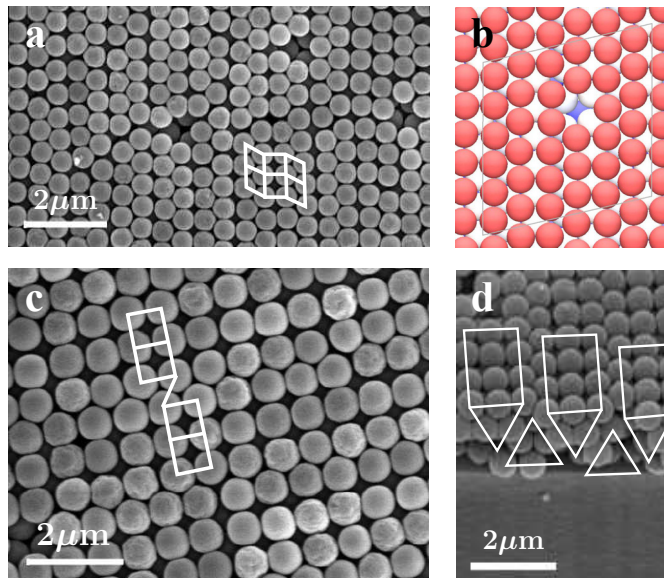


Figure 5.3: SEM micrographs of the prism phase found in this work:  $2P_A$  (a) and  $3P^l_{\square}$  (c,d). A few particles were removed from the top layer upon detachment of the covering plate allowing access to the structure in the layer below. A simulation snapshot, where a particle was also removed (after the simulation), is shown in (b). White lines indicate the symmetry of each phase (a,c) as well as the structure of the prism arrays in the side view of  $3P^l_{\square}$  (d).

clips. We employed Polystyrene particles of different sizes ranging from 245 nm up to 800 nm in diameter (Ikerlat Polymers) in different experiments. We washed and rinsed the particles several times with deionized water (18.2 M $\Omega$ cm). We put several drops of 1% (w/w) aqueous suspension of particles into a 2-cm-high glass tube attached to the covering plate of the cells, where the particles entered from the tube to the cells by capillarity forces through a small hole drilled on the covering plate. The water evaporation concentrated the particles and after several days the system condensed into several facets. Finally, after the sample was dried, we detached the Polystyrene covering plate. Some particles stuck to the covering plate during its removal resulting in holes in the top layer of particles, which allowed us to study the structure in the layers below. We recorded Scanning Electron Microscope (SEM) images from the top facets and side edges by cleaving the samples or by Focused Ion Beam milling following the crystal planes.

Concentrating on the regime  $3\square \rightarrow 3\Delta$ , we found evidence of the adaptive  $2P_A$  phase. Also, the  $3P^l_{\square}$  phase has been observed for larger plate separation distances. As an example, SEM images of  $2P_A$  and  $3P^l_{\square}$  are shown in Fig. 5.3 along with a simulation snapshot for comparison.

Experiments on colloidal systems, such as ours, are necessarily performed at fi-

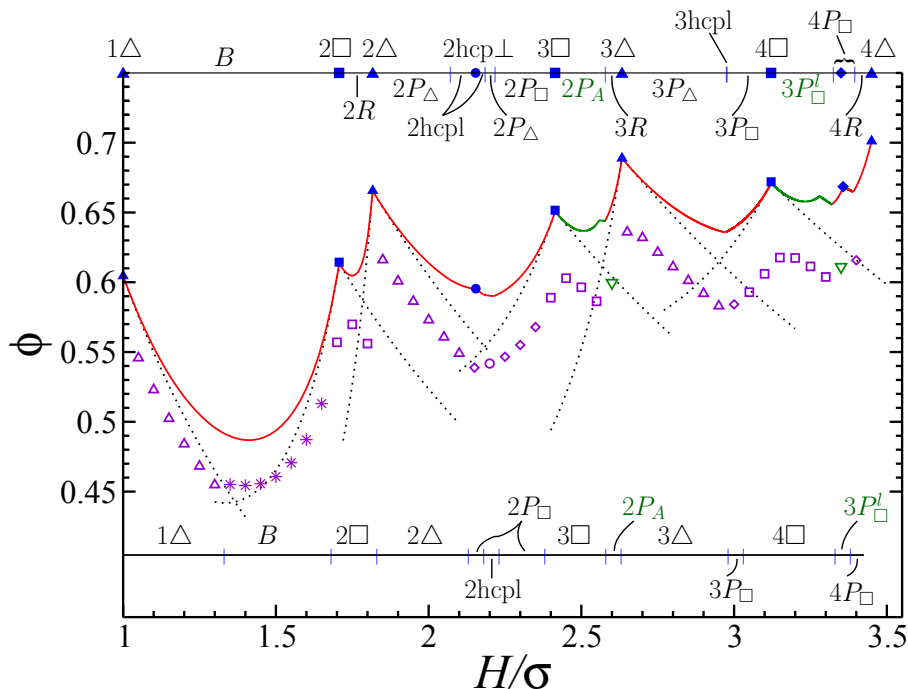


Figure 5.4: Isobaric packing fractions  $\phi$ , as measured in simulations at fixed lateral pressure  $P_l\sigma^3/k_B T = 40$  for confined hard spheres, versus dimensionless separation  $H/\sigma$  (empty symbols) compared to the theoretical results of Fig. 5.2 (lines). Each type of empty symbol denotes a different phase. The observed phases are indicated by the symbols on the horizontal lines at the top (theory) and bottom (simulation) of the graph.

nite pressure. In order to investigate the stability of the new prism phases away from close packing, we performed Monte Carlo simulations at a fixed lateral pressure  $P_l = -H^{-1}\partial F/\partial A$ , where  $F$  is the free energy and  $A$  denotes the area of the system. This definition of pressure is such that it approaches the bulk pressure as  $H$  increases. The discovery of new crystal phases in this and previous theoretical works at infinite pressure after the previous simulation work that addressed the stability at finite pressure begs the question how stable these phases are at a high, but finite pressure [232]. We simulated the system at a high pressure  $P_l\sigma^3/k_B T = 40$ , for which the system would equilibrate within a reasonable time (for comparison the bulk crystallization pressure is  $P\sigma^3/k_B T = 11.56$  [233]). The success of cell

theory—effectively a single-particle theory—at high densities indicates that phase behavior at high pressures can be accurately modeled using relatively small systems. Our variable-shape simulation box contained  $m \times m \times n$  particles, where  $n$  is the number of layers and  $4 \leq m \leq 8$ . The horizontal cross-section of the simulation box was allowed to deform to a general parallelogram [234], for instance, upon a

crystal–crystal transition. Nevertheless, transitions between square symmetry and hexagonal symmetry phases were not observed for some values of  $H$ , so both square and hexagonal layers were used as initial conditions: An fcc (100) or (111) crystal was expanded horizontally/vertically to allow an overlap-free initial condition that just fits in the slit. The number of layers  $n$  was adjusted to obtain the maximum density. We performed five separate runs for each initial configuration and, if these in total 10 runs did not all result in the same final structure, we chose the maximum density configuration, which is justified by the high pressure. In Fig. 5.4,

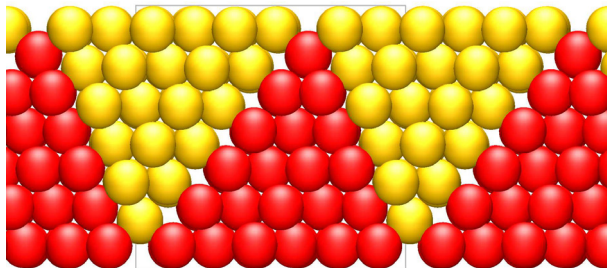


Figure 5.5: The  $6P_{\Delta}$  phase found for  $5.73(3) \lesssim H/\sigma \lesssim 5.88(3)$  from Monte Carlo simulations. (The snapshot is periodically repeated; the original simulation box is indicated by the gray rectangle.)

we compare finite-pressure simulation data to theoretical results at infinite pressure. We clearly see that the packing fractions in both cases feature a qualitatively similar course. However, some phases vanish for finite pressure as this regime is dominated by broadened stability regimes of  $n\Delta$  and  $n\Box$  phases. In detail, the  $2R$ ,  $3R$ ,  $2\text{hcp}_{\perp}$ ,  $3\text{hcp}_{\perp}$ ,  $2P_{\Delta}$  and  $3P_{\Delta}$  phases are not found for the finite pressure and accuracy  $H/\sigma \pm 0.025$  chosen in the simulations. As can be further seen, the adaptive prism phase  $2P_A$  and  $3P_{\Box}^l$  found in this work are stable at this pressure and, therefore, also at all higher pressures.

These simulations help explain the absence of the triangular prism phase in the experiments (see [181]). We also performed simulations with the triangular prism phases as initial configuration. At the values for  $H$  where the triangular prism phase has the highest density of all possible phases, the  $nP_{\Delta}$  phase appears to consist of  $n$  only slightly distorted hexagonal layers. At finite pressure, the small distortions can quickly disappear and a regular triangular crystal can be formed. This is a typical scenario for crystal–crystal transitions for hard particles, where the close packed crystal phase transforms into a higher–symmetry crystal with a slightly lower density, but a greater entropy, as the pressure is decreased sufficiently. At larger values of  $H$  than those investigated here, the triangular prisms are significantly enhanced and do not transform so easily to triangular crystals (cf. [151]). Preliminary simulations show that indeed stable triangular prism phases can be found for larger values

for  $H$  (see 5.5).

Furthermore, recent simulation work [151] and theoretical [170, 180] investigations show that the buckling phase  $2B$  as well as the bilayered rhombic phase  $2R$  are highly degenerated as there exists linear and zig-zag ordering of the unit cells in the corresponding phase structures. Likewise, we studied the phase behavior of rhombic phases  $nR$  for  $n = 3, 4$  closer. As a result, we notice that higher layered rhombic phases are degenerated in the same way: we found zig-zag rhombic in addition to the linear one. The corresponding structures are illustrated in Fig. 5.6.

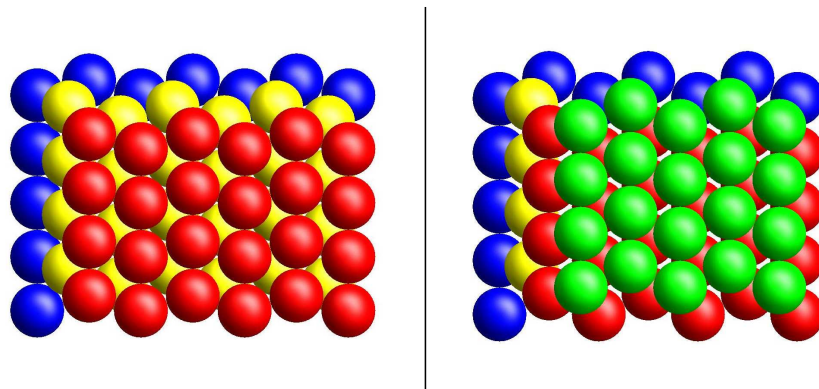


Figure 5.6: Zig-zag orderings in the phase structures  $3R$  (left) and  $4R$  (right). In addition to linear ordering of the unit cells of these phases, we also found close-packed zig-zag ordering yielding a degeneracy in the packing fraction. Different colors correspond to different layers parallel to confining walls.

In conclusion, we explored the close-packed structures of hard spheres confined between hard plates in a broad range of plate separations by combining theory, experiment and simulation. We identified adaptive prism phases with rhombic symmetry which pack densest in certain ranges of the slit width. An adaptive prism phase optimizes packing by adjusting its base symmetry flexibly to the slit width. Also, we showed a high persistence of these adaptive prism phases at finite, but large pressure using experiments and simulations. We anticipate that adaptive prism phase will play a key role for even higher plate distances,  $H/\sigma > 3.5$ , as ideal interpolating close-packed building blocks.

The adaptive prism phases found here offer new opportunities for several applications. For example, the reported structures possess pronounced symmetry directions whose alignment can be internally controlled by the slit height instead of using external fields (eg. electric fields, cf. [235]). As a consequence, these phases can serve as switchable materials. Furthermore, we expect an unusual and anisotropic dynamical response of the multilayered prism phases upon shear [236] with possibly

molten grain boundaries which can be exploited to tune the rheological properties of thin crystalline sheets. Finally, by varying  $H$ , it is possible to tune the whole complex cascade of close-packed structures. This may be of importance to fabricate nano-sieves or porous membranes [39] in a controlled way.

# Appendix

## Appendix I: Taylor expansion of Lekner sums for unscreened Coulomb system

The total interaction energy per unit cell of a crystalline unscreened Coulomb system can be written as

$$U_C = U_C^s + U_C^c, \quad (5.1)$$

where the unit cell consists of  $n$  particles of charge  $q$  located at  $\mathbf{r}_i$ . The self energy  $U_C^s$  in equation (5.1) stems from the interaction between a particle of the unit cell and its own periodically repeated images. The term  $U_C^c$  in equation (5.1), is due to the interaction between a particle of the unit cell and all other remaining  $n - 1$  particles of the cell including their own images. The convergence involved in these sums is guaranteed by the inclusion of a *surface* neutralizing background for each layer. Following the route of Bródka and Grzybowski (see equations (16a), (16b) and (17) of reference [165]),  $U_C^s$  and  $U_C^c$  are given below. Therefore  $U_C^s$  reads

$$U_C^s = \frac{1}{|a_x|} n \frac{q^2}{\epsilon} \left\{ 4 \left( \sum_{m,k=1}^{\infty} \cos \left( 2\pi k \frac{b_x}{a_x} m \right) K_0 \left( 2\pi k \left| \frac{b_y}{a_x} \right| m \right) \right) + \gamma_e - \ln \left( 4\pi \left| \frac{a_x}{b_y} \right| \right) \right\}, \quad (5.2)$$

with  $\gamma_e = 0.577215665$  denoting the Euler-Mascheroni constant,  $K_0(x)$  the modified Bessel function of the second kind [237] and  $a_x$ ,  $b_x$  and  $b_y$  the corresponding  $x$ - and  $y$ -components of the lattice vectors  $\mathbf{a}$  and  $\mathbf{b}$ . Using the components  $x_{ij} = x_i - x_j$ ,  $y_{ij} = y_i - y_j$  and  $z_{ij} = z_i - z_j$  of the relative separation vector  $\mathbf{r}_{ij}$  between cell

particles  $i$  and  $j$ ,  $U_C^c$  can be written as

$$\begin{aligned}
U_C^c &= \frac{1}{|a_x|} \sum_{i=1}^n \sum_{\substack{j=1 \\ j>i}}^n \frac{q^2}{\epsilon} \\
&\times \left\{ 4 \sum_{m,k=1}^{\infty} \left[ \cos \left( 2\pi k \frac{x_{ij} + b_x m}{a_x} \right) K_0 \left( 2\pi k \left[ \frac{(y_{ij} + b_y m)^2 + z_{ij}^2}{a_x^2} \right]^{1/2} \right) \right. \right. \\
&\quad \left. \left. + \cos \left( 2\pi k \frac{x_{ij} - b_x m}{a_x} \right) K_0 \left( 2\pi k \left[ \frac{(y_{ij} - b_y m)^2 + z_{ij}^2}{a_x^2} \right]^{1/2} \right) \right] \right. \\
&\quad \left. + 4 \sum_{k=1}^{\infty} \cos \left( 2\pi k \frac{x_{ij}}{a_x} \right) K_0 \left( 2\pi k \left[ \frac{y_{ij}^2 + z_{ij}^2}{a_x^2} \right]^{1/2} \right) \right. \\
&\quad \left. - \ln \left[ \cosh \left( 2\pi \left| \frac{z_{ij}}{b_y} \right| \right) - \cos \left( 2\pi \frac{y_{ij}}{b_y} \right) \right] - \ln 2 \right\} \quad (5.3)
\end{aligned}$$

for  $(y_{ij}, z_{ij}) \neq (0, 0)$  and

$$\begin{aligned}
U_C^c &= \frac{1}{|a_x|} \sum_{i=1}^n \sum_{\substack{j=1 \\ j>i}}^n \frac{q^2}{\epsilon} \left\{ 4 \sum_{m=1}^{\infty} \sum_{k=1}^{\infty} \left[ \cos \left( 2\pi k \frac{x_{ij} + b_x m}{a_x} \right) K_0 \left( 2\pi k \left| \frac{b_y m}{a_x} \right| \right) \right. \right. \\
&\quad \left. \left. + \cos \left( 2\pi k \frac{x_{ij} - b_x m}{a_x} \right) K_0 \left( 2\pi k \left| \frac{b_y m}{a_x} \right| \right) \right] \right. \\
&\quad \left. - 2\psi \left( \left| \frac{x_{ij}}{a_x} \right| \right) - \pi \cot \left( \pi \left| \frac{x_{ij}}{a_x} \right| \right) - 2 \ln \left( 4\pi \left| \frac{a_x}{b_y} \right| \right) \right\} \quad (5.4)
\end{aligned}$$

for  $(y_{ij}, z_{ij}) = (0, 0)$ , where  $\psi(x)$  is the digamma function [237].

Being interested in the transition from mono- to trilayers, we take as input the structure characteristics of the triangular phase  $1\Delta$  into the lattice sums (5.2)-(5.4):  $\theta = \pi/3$ ,  $b_x/a_x = 0.5$ ,  $b_y/a_x = \sqrt{3}/2$ ,  $\gamma = 1$ ,  $x_{12}/a_x = 0.5 = x_{23}/a_x$ ,  $y_{12}/b_y = 1/3 = y_{23}/b_y$ ,  $x_{13}/a_x = 1$ ,  $y_{13}/b_y = 2/3$ ,  $\rho = N/A = \frac{3}{a_x b_y} = \frac{2\sqrt{3}}{a_x^2}$  and therefore  $a_x^2 = \frac{2\sqrt{3}}{\rho} = \frac{2\sqrt{3}L^2}{\eta}$ . Here we consider for  $1\Delta$  a multicell ( $n = 3$ ) consisting of three primitive cells, containing each 1 particle. Thus, for a given  $\eta$ , the energy function  $U_C$  depends now only on  $z_{12} = hL = z_{23}$ . Taking this feature into account, the self energy and the cross energy finally read

$$U_C^s = \frac{1}{|a_x|} 3 \frac{q^2}{\epsilon} \left\{ 4 \sum_{m,k=1}^{\infty} \cos(\pi km) K_0(\pi km \sqrt{3}) + \gamma_e - \ln \left( \frac{8\pi}{\sqrt{3}} \right) \right\} \quad (5.5)$$

and

$$\begin{aligned}
U_C^c(h) &= \frac{1}{|a_x|} \sum_{i=1}^3 \sum_{\substack{j=1 \\ j>i}}^3 \frac{q^2}{\epsilon} \\
&\times \left\{ 4 \sum_{m,k=1}^{\infty} \left[ \cos \left( 2\pi k \frac{x_{ij} + b_x m}{a_x} \right) K_0 \left( 2\pi k \left[ \lambda_{ij}^{+2} + \beta_{ij}^2 h^2 \right]^{1/2} \right) \right. \right. \\
&\quad \left. \left. + \cos \left( 2\pi k \frac{x_{ij} - b_x m}{a_x} \right) K_0 \left( 2\pi k \left[ \lambda_{ij}^{-2} + \beta_{ij}^2 h^2 \right]^{1/2} \right) \right] \right. \\
&\quad \left. + 4 \sum_{k=1}^{\infty} \cos \left( 2\pi k \frac{x_{ij}}{a_x} \right) K_0 \left( 2\pi k \left[ \frac{y_{ij}^2}{a_x^2} + \beta_{ij}^2 h^2 \right]^{1/2} \right) \right. \\
&\quad \left. - \ln \left[ \cosh (2\pi |\phi_{ij}| h) - \cos \left( 2\pi \frac{y_{ij}}{b_y} \right) \right] - \ln 2 \right\}, \quad (5.6)
\end{aligned}$$

where  $\lambda_{12}^{\pm} = \sqrt{(y_{12} \pm b_y m)^2 / a_x^2} = \sqrt{3/4}(1/3 \pm m) = \lambda_{23}^{\pm}$ ,  $\lambda_{13}^{\pm} = \sqrt{(y_{13} \pm b_y m)^2 / a_x^2} = \sqrt{3/4}(2/3 \pm m)$ ,  $\beta_{12} = L/a_x = \beta_{23}$ ,  $\beta_{13} = 2L/a_x$ ,  $\phi_{12} = \sqrt{2\eta/3\sqrt{3}} = \phi_{23}$  and  $\phi_{13} = 2\sqrt{2\eta/3\sqrt{3}}$ . Before expanding the energy function at  $h = 0$ , we first define

$$f(h)^{\pm} = K_0 \left( 2\pi k \left[ \lambda^{\pm 2} + \beta^2 h^2 \right]^{1/2} \right), \quad (5.7)$$

where the first four derivatives of  $f(h)$  at  $h = 0$  are given as follows:

$$f(0)^{\pm} = K_0 (2\pi k \lambda^{\pm}), \quad (5.8)$$

$$f'(0)^{\pm} = 0, \quad (5.9)$$

$$f''(0)^{\pm} = -K_1 (2\pi k \lambda^{\pm}) \frac{2\pi k \beta^2}{\lambda^{\pm}}, \quad (5.10)$$

$$f'''(0)^{\pm} = 0, \quad (5.11)$$

$$f''''(0)^{\pm} = [K_0 (2\pi k \lambda^{\pm}) 2\pi k \lambda^{\pm} + 2K_1 (2\pi k \lambda^{\pm})] \frac{3\beta^4 2\pi k}{\lambda^{\pm 3}}. \quad (5.12)$$

Here,  $K_1(x)$  is a modified Bessel function of the second kind [237], too. Using a Taylor series and (5.8)-(5.12), we now expand  $U_C(h)$  from (5.1) at  $h = 0$  and achieve the final form of the energy:

$$\frac{\epsilon u(h)}{q^2 \sqrt{\rho}} = -1.960516 - \underbrace{3.590668\eta h^2 + 4.968827\eta^2 h^4}_{\frac{U_C(h)\epsilon}{3q^2 \sqrt{\rho}}} + \frac{4}{3}\pi h^2 \sqrt{\eta}. \quad (5.13)$$

The last term stems from (3.5), due to interactions with the background, respectively. The coefficient  $-1.960516$  corresponds to the static energy per particle of the triangular lattice, which was already calculated in [35].

## Appendix II: Theory of Crystal Growth Behavior

Here, we furthermore develop a simple theory to characterize the crystal growth behavior. We model the system with a coarse-grained one-particle density fluid  $\rho(r, t)$  around the origin of the trap where the initial condition  $\rho(r, t = 0) = \rho_f$  is imposed. Due to the external trap force we assume a crystallite of radius  $R_c(t)$  to be formed at a density  $\rho_c > \rho_f$  around the origin. According to the repulsive inter-particle force and the decay of the trap force with distance, the growth is supposed to stop after a while. The size of the crystallite can be predicted by applying the continuity equation at the boundary of the crystallite. We here consider the crystallite as a hemisphere (3d) located at the seed. For the number of crystalline particles in the crystallite,  $N_c(t)$ , we have:

$$\dot{N}_c = \rho_c \frac{d}{dt} \left( \frac{2}{3} \pi R_c^3(t) \right) = 2\pi \rho_c R_c^2(t) \dot{R}_c(t). \quad (5.14)$$

On the other hand, this must be balanced by the flux of incoming particles,  $j(R_c(t)) = \rho_f \frac{F(R_c(t))}{\gamma}$ , leading to

$$\dot{N}_c = -2\pi R_c^2(t) \rho_f \frac{F(R_c(t))}{\gamma}, \quad (5.15)$$

where  $F(r)$  is the total force acting on the particles

$$F(r) = F_0(r) + F_1(r), \quad (5.16)$$

which stems from *i*) the attractive force from the external trap ( $F_0 = |\mathbf{F}_0|$ , cf. Eq. 2.6) and *ii*) the repulsive force from the inner crystallite particles  $F_1$ . The latter can be approximated in the mean-field theory leading to a distance independent force. Detailed calculations with a cutoff  $a = \rho_f^{-1/3}$  in the interaction range lead to

$$F_1 = \pi V_0 (\rho_c - \rho_f) \frac{1}{2\kappa^2} e^{-\kappa a} (2 + \kappa a), \quad (5.17)$$

Equating Eqns. (5.14) and (5.15) yields

$$\dot{R}_c = \frac{\rho_f}{\rho_c} \left( \frac{A}{R_c^2(t)} - \frac{F_1}{\gamma} \right). \quad (5.18)$$

For  $t \rightarrow \infty$ ,  $R_c$  will approach its equilibrium (static) value

$$R_\infty = R_c(t \rightarrow \infty) = \left( \frac{A\gamma}{F_1} \right)^{1/2}. \quad (5.19)$$

For large time, Eq. (5.18) can be linearized to yield

$$\frac{d}{dt} (R_\infty - R_c(t)) = (R_\infty - R_c(t)) \frac{2A\rho_f}{R_\infty^3 \rho_c} \quad (5.20)$$

with the solution

$$R_\infty - R_c(t) = \bar{R}e^{-\lambda t}, \quad (5.21)$$

where  $\bar{R}$  denotes a fit parameter and  $\tau = 1/\lambda = R_\infty^3 \rho_c / 2A\rho_f$  the associated decay time. Eq. (5.21) implies that the approach towards  $R_\infty$  is exponential in time as found in the experiment and simulation, see Fig. 2.5(b) and 2.7(b). The saturation radius has been calculated with Eq. (5.19) to  $\kappa R_\infty \approx 330$  that shows a good agreement between the theory and simulation, too.



# Bibliography

- [1] R. A. L. Jones, *Soft Condensed Matter* (Oxford University Press, Oxford, 2002).
- [2] P. N. Pusey and W. van Meegen, *Nature* **320**, 340 (1986).
- [3] W. M. Stanley, *Science* **81**, 644 (1935).
- [4] R. C. Williams and K. M. Smith, *Nature* **179**, 119 (1957).
- [5] P. Pieranski, *Contemp. Phys.* **24**, 25 (1983).
- [6] A. Ivlev, H. Löwen, G. Morfill, and C. P. Royall, in *Complex Plasmas and Colloidal Dispersions: Particle-resolved Studies of Classical Liquids and Solids*, edited by D. Andelman and G. Reiter (World Scientific, Singapore, 2012).
- [7] G. Bryant *et al.*, *Phys. Rev. E* **66**, 060501 (2002).
- [8] J.-P. Hansen and H. Löwen, *Ann. Rev. Phys. Chem.* **51**, 209 (2000).
- [9] E. Allahyarov, I. D'Amico, and H. Löwen, *Phys. Rev. E* **90**, 3199 (1999).
- [10] R. Messina, *J. Phys.: Condens. Matter* **21**, 113102 (2009).
- [11] E. J. W. Verwey and J. T. G. MacDonald, *Theory of stability of lyophobic colloids* (Elsevier, Amsterdam, 1948).
- [12] B. V. Derjaguin and L. Landau, *Acta Physicochim. (USSR)* **14**, 633 (1941).
- [13] J. C. Crocker and D. G. Grier, *J. Colloid Interface Sci.* **179**, 298 (1996).
- [14] S. M. Woodley and R. Catlow, *Nature Mat.* **7**, 937 (2008).
- [15] D. Turnbull and J. C. Fischer, *J. Chem. Phys.* **17**, 71 (1949).
- [16] S. Dietrich and A. Haase, *Phys. Rep.* **260**, 1 (1995).
- [17] J. M. Drake and J. Klafter, *Phys. Today* **43**, 46 (1990).
- [18] K. Morishige and K. Kawano, *J. Chem. Phys.* **110**, 4867 (1999).

- 
- [19] A. Schreiber, I. Ketelsen, and G. Findenegg, *Phys. Chem. Chem. Phys.* **3**, 1185 (2001).
- [20] K. Watanabe, T. Kawasaki, and H. Tanaka, *Nature Mat.* **10**, 512 (2011).
- [21] S. Auer and D. Frenkel, *Phys. Rev. Lett.* **91**, 015703 (2003).
- [22] N. D. Mermin and H. Wagner, *Phys. Rev. Lett.* **17**, 1133 (1966).
- [23] N. D. Mermin, *Phys. Rev.* **176**, 250 (1968).
- [24] J. Fröhlich and C. Pfister, *Communications in Mathematical Physics* **81**, 277 (1981).
- [25] J. M. Kosterlitz and D. J. Thouless, *Solid State Phys.* **6**, 1181 (1973).
- [26] D. R. Nelson and B. I. Halperin, *Phys. Rev. B* **19**, 2457 (1979).
- [27] A. P. Young, *Phys. Rev. B* **19**, 1855 (1979).
- [28] K. Z. R. Lenke and G. Maret, *Phys. Rev. Lett.* **82**, 2721 (1999).
- [29] K. Zahn and G. Maret, *Phys. Rev. Lett.* **85**, 3656 (2000).
- [30] H. Löwen, *Phys. Rep.* **237**, 249 (1994).
- [31] F. A. Lindemann, *Phys. Z* **14**, 609 (1910).
- [32] J. P. Hansen, *Phys. Rev. A* **8**, 3096 (1973).
- [33] M. O. Robbins, K. Kremer, and G. S. Grest, *J. Chem. Phys.* **88**, 3286 (1988).
- [34] S. Prestipino, F. Saija, and G. Malescio, *Soft Matter* **5**, 2795 (2009).
- [35] L. Bonsall and A. A. Maradudin, *Phys. Rev. B* **15**, 1959 (1977).
- [36] A. R. Denton and H. Löwen, *Phys. Rev. Lett.* **81**, 469 (1998).
- [37] Y. Peng *et al.*, *Phys. Rev. Lett.* **104**, 205703 (2010).
- [38] H. S. Park and Y. Xia, *Langmuir* **15**, 266 (1999).
- [39] W. A. Goedel and F. Yan, *Nano Lett.* **4**, 1193 (2004).
- [40] J. D. Watson and F. H. C. Crick, *Nature* **171**, 737 (1953).
- [41] Y. Snir and R. D. Kamien, *Science* **307**, 1067 (2005).
- [42] R. O. Erickson, *Science* **181**, 4101 (1973).
- [43] M. Tymczenko *et al.*, *Adv. Mat.* **20**, 2315 (2008).

- 
- [44] M. A. Lohr *et al.*, Phys. Rev. E **81**, 040401 (2010).
- [45] G. T. Pickett, M. Gross, and H. Okuyama, Phys. Rev. Lett. **85**, 3652 (2000).
- [46] D. Zerrouki *et al.*, Nature **455**, 380 (2008).
- [47] M. Hodak and L. A. Girifalco, Phys. Rev. B **67**, 075419 (2003).
- [48] W. Mickelson *et al.*, Science **300**, 467 (2003).
- [49] A. N. Khlobystov, D. A. Britz, A. Ardavan, and G. A. Briggs, Phys. Rev. Lett. **92**, 245507 (2004).
- [50] P. Dobriyal *et al.*, Macromol. **42**, 9082 (2009).
- [51] M. Peterca *et al.*, J. Am. Chem. Soc. **130**, 14840 (2008).
- [52] J. P. Lindner *et al.*, Angewandte Chemie - International Edition **48**, 8874 (2009).
- [53] P. R. Bandaru, C. Daraio, K. Yang, and A. M. Rao, J. Appl. Phys. **101**, 094307 (2007).
- [54] S. M. Yang *et al.*, Adv. Materials **11**, (1999).
- [55] H. H. Wensink and G. Jackson, J. Chem. Phys. **130**, 234911 (2009).
- [56] R. Messina and H. Löwen, Phys. Rev. Lett. **91**, 146101 (2003).
- [57] R. Messina, J. Phys.: Condens. Matter **21**, 113102 (2009).
- [58] H. Löwen *et al.*, J. Phys.: Condens. Matter **20**, 404221 (2008).
- [59] E. C. Oğuz, R. Messina, and H. Löwen, J. Phys.: Cond. Matter **21**, 424110 (2009).
- [60] E. C. Oğuz, R. Messina, and H. Löwen, EPL **86**, 28002 (2009).
- [61] S. Grandner and S. H. L. Klapp, Europhys. Lett. **90**, 68004 (2010).
- [62] A. Reinmüller, H. J. Schöpe, and T. Palberg, Soft Matter **6**, 5312 (2010).
- [63] H. B. Eral *et al.*, Langmuir **26**, 16722 (2010).
- [64] H. B. Eral, D. van den Ende, F. Mugele, and M. H. G. Duits, Phys. Rev. E **80**, 061403 (2009).
- [65] Z. Dónko, G. J. Kalman, and P. Hartmann, J. Phys.: Condens. Matter **20**, 413101 (2008).

- 
- [66] G. E. Morfill and A. V. Ivlev, *Rev. Mod. Phys.* **81**, 1353 (2009).
- [67] G. Piacente, G. Q. Hai, and F. M. Peeters, *Phys. Rev. B* **81**, 024108 (2010).
- [68] T. Torimoto, T. Tsuda, K. Okazaki, and S. Kuwabata, *Advanced Materials* **22**, 1196 (2010).
- [69] H. T. Zhang *et al.*, *Eur. J. Inorganic Chem.* 3532 (2006).
- [70] J. Dzubiella, R. J. Allen, and J. P. Hansen, *J. Chem. Phys.* **120**, 5001 (2004).
- [71] P. Bolhuis, M. Hagen, and D. Frenkel, *Phys. Rev. E* **50**, 4880 (1994).
- [72] C. N. Likos, Z. T. Németh, and H. Löwen, *J. Phys.: Cond. Matter* **6**, 10965 (1994).
- [73] P. Bolhuis and D. Frenkel, *J. Phys.: Cond. Matter* **9**, 381 (1997).
- [74] L. van Hove, *Physica* **16**, 137 (1950).
- [75] J. A. Cuesta and A. Sánchez, *J. Stat. Phys.* **115**, 869 (2004).
- [76] R. Messina and H. Löwen, *Phys. Rev. E* **73**, 011405 (2006).
- [77] W. P. Ferreira, G. A. Farias, and F. M. Peeters, *J. Phys.: Condens. Matter* **22**, 285103 (2010).
- [78] D. Kashchiev, *Nucleation* (Butterworth-Heinemann, Oxford, 2000).
- [79] A. N. Kolmogorov, *Izv. Akad. Nauk SSSR, Ser. Matem.* **1**, 355 (1937).
- [80] W. A. Johnson and R. F. Mehl, *Trans. Am. Inst. Min. Metall. Eng.* **135**, 416 (1939).
- [81] M. Avrami, *J. Chem. Phys.* **7**, 1103 (1939).
- [82] M. Avrami, *J. Chem. Phys.* **8**, 212 (1940).
- [83] M. Avrami, *J. Chem. Phys.* **9**, 177 (1941).
- [84] C. D. van Sicle, *Phys. Rev. B* **54**, 11845 (1996).
- [85] V. J. Anderson and H. N. W. Lekkerkerker, *Nature* **416**, 811 (2002).
- [86] J. L. Harland and W. van Meegen, *Phys. Rev. E* **55**, 3054 (1997).
- [87] T. Palberg, *J. Phys.: Condens. Matter* **11**, R323 (1999).

- 
- [88] K. F. Kelton and A. L. Greer, *Nucleation in Condensed Matter: Applications in Materials and Biology* (Pergamon, Elsevier, 2010), pergamon Materials Series.
- [89] A. Yethiraj, *Soft Matter* **3**, 1099 (2007).
- [90] U. Gasser, *J. Phys.: Cond. Matt.* **21**, 203101 (2009).
- [91] M. Sullivan *et al.*, *J. Phys.: Condens. Matter* **15**, S11 (2003).
- [92] H. Löwen, *J. Phys.: Condens. Matter* **13**, R415 (2001).
- [93] A. van Blaaderen, *MRS Bulletin* **29**, 85 (2004).
- [94] H. J. Schöpe, *J. Phys.: Condens. Matter* **15**, L533 (2003).
- [95] T. Gong, D. T. Wu, and D. W. M. Marr, *Langmuir* **19**, 5967 (2003).
- [96] Y. Solomentsev, M. Böhmer, and J. L. Anderson, *Langmuir* **13**, 6058 (1997).
- [97] M. Böhmer, *Langmuir* **12**, 5747 (1996).
- [98] T. Gong and D. W. M. Marr, *Appl. Phys. Lett.* **85**, 3760 (2004).
- [99] J. P. Hoogenboom *et al.*, *Appl. Phys. Lett.* **80**, 4828 (2002).
- [100] A. Stipp *et al.*, *J. Phys.: Condens. Matter* **16**, S3885 (2004).
- [101] Y. Tang *et al.*, *J. Phys. A: Math. Gen.* **20**, L189 (1987).
- [102] J. P. Hoogenboom, A. K. van Langen-Suurling, J. Romijn, and A. van Blaaderen, *Phys. Rev. E* **69**, 051602 (2004).
- [103] A. B. Fontecha *et al.*, *J. Phys.: Condens. Matter* **17**, S2779 (2005).
- [104] J. M. Kosterlitz and D. J. Thouless, *J. Phys. C: Solid State Physics* **6**, 1181 (1973).
- [105] D. R. Nelson and B. I. Halperin, *Phys. Rev. B* **19**, 2457 (1979).
- [106] A. P. Young, *Phys. Rev. B* **19**, 1855 (1979).
- [107] T. Palberg, W. Mönch, J. Schwarz, and P. Leiderer, *J. Chem. Phys.* **102**, 5082 (1995).
- [108] M. Franke, A. Lederer, and H. J. Schöpe, *Soft Matter* **7**, 11267 (2011).
- [109] A. Engelbrecht, R. Meneses, and H. Schöpe, *Soft Matter* **7**, 5685 (2011).
- [110] B. J. Ackerson and N. A. Clark, *Physica A* **118**, 221 (1983).

- 
- [111] J. L. Anderson and D. C. Prieve, Separation and Purification Methods **13**, 67 (1984).
- [112] D. C. Prieve, J. L. Anderson, J. P. Ebel, and M. E. Lowell, J. Fluid Mech. **148**, 247 (1984).
- [113] J. L. Anderson, Ann. Rev. Fluid Mech. **21**, 61 (1989).
- [114] M. Ibele, T. E. Mallouk, and A. Sen, Angew. Chem.-Intl. Ed. **48**, 3308 (2009).
- [115] P. Wette, H. J. Schöpe, R. Biehl, and T. Palberg, J. Chem. Phys. **114**, 7556 (2001).
- [116] L. Assoud *et al.*, Phys. Rev. Lett. **102**, 238301 (2009).
- [117] H. Löwen, J. Phys.: Cond. Matt. **4**, 10105 (1992).
- [118] E. Chang and D. Hone, EPL **5**, 635 (1988).
- [119] E. J. Stamhuis, Aquatic Ecology **40**, 463 (2006).
- [120] R. D. Keane and R. J. Adrian, Applied Scientific Research **49**, 191 (1992).
- [121] A. Kose *et al.*, Journal of Colloid and Interface Science **44**, 330 (1973).
- [122] B. V. R. Tata, M. Rajalakshmi, and A. K. Arora, Phys. Rev. Lett. **69**, 3778 (1992).
- [123] T. Palberg and M. Würth, Phys. Rev. Lett. **72**, 786 (1994).
- [124] B. V. R. Tata and A. K. Arora, Phys. Rev. Lett. **72**, 787 (1994).
- [125] Y. Levin, Reports on Progress in Physics **65**, 1577 (2002).
- [126] H. Löwen, P. A. Madden, and J. P. Hansen, Phys. Rev. Lett. **68**, 1081 (1992).
- [127] H. Löwen, J. P. Hansen, and P. A. Madden, J. Chem. Phys. **98**, 3275 (1993).
- [128] H. Löwen, J. Chem. Phys. **100**, 6738 (1994).
- [129] Y. Levin and J. J. Arenzon, J. Phys. A - Math. Gen. **36**, 5857 (2003).
- [130] G. Orkoulas, A. Z. Panagiotopoulos, and M. E. Fisher, Phys. Rev. E **61**, 5930 (2000).
- [131] Y. Levin, J. Phys.: Condens. Matter **14**, 2303 (2002).
- [132] E. Allahyarov, I. D'Amico, and H. Löwen, Phys. Rev. Lett. **81**, 1334 (1998).
- [133] E. Allahyarov, G. Gompper, and H. Löwen, Phys. Rev. E **69**, 041904 (2004).

- 
- [134] E. Allahyarov *et al.*, Europhys. Lett. **78**, 38002 (2007).
- [135] M. E. Leunissen *et al.*, Nature **437**, 235 (2005).
- [136] A. P. Hynninen *et al.*, Phys. Rev. Lett. **96**, 138308 (2006).
- [137] C. A. Murray and D. G. Grier, Annu. Rev. Phys. Chem. **47**, 421 (1996).
- [138] B. A. Klumov and G. E. Morfill, Journal of Experimental and Theoretical Phys. **107**, 908 (2008).
- [139] A. B. Fontecha and H. J. Schöpe, Phys. Rev. E **77**, 061401 (2008).
- [140] I. Cohen, T. G. Mason, and D. A. Weitz, Phys. Rev. Lett. **93**, 046001 (2004).
- [141] S. H. L. Klapp, Y. Zeng, D. Qu, and R. von Klitzing, Phys. Rev. Lett. **100**, 118303 (2008).
- [142] V. Lobaskin, M. Brunner, C. Bechinger, and H. H. von Grünberg, J. Phys.: Condens. Matter **15**, 6693 (2003).
- [143] H. Löwen and G. Kramposthuber, Europhys. Lett. **23**, 673 (1993).
- [144] H. Löwen and E. Allahyarov, J. Phys.: Condens. Matter **10**, 4147 (1998).
- [145] C. Russ, H. H. von Grünberg, M. Dijkstra, and R. van Roij, Phys. Rev. E **66**, 011402 (2002).
- [146] C. Russ, M. Brunner, C. Bechinger, and H. H. von Grünberg, Europhys. Lett. **69**, 468 (2005).
- [147] J. Dobnikar, R. Castaneda-Priego, H. H. von Grünberg, and E. Trizac, New Journal of Physics **8**, 277 (2006).
- [148] S. Nesper, C. Bechinger, P. Leiderer, and T. Palberg, Phys. Rev. Lett. **79**, 2348 (1997).
- [149] F. Ramiro-Manzano, E. Bonet, I. Rodriguez, and F. Meseguer, Phys. Rev. E **76**, 050401(R) (2007).
- [150] A. B. Fontecha, T. Palberg, and H. J. Schöpe, Phys. Rev. E **76**, 050402(R) (2007).
- [151] A. Fortini and M. Dijkstra, J. Phys.: Condens. Matter **18**, 371 (2006).
- [152] S. Grandner and S. H. L. Klapp, J. Chem. Phys. **129**, 244703 (2008).
- [153] G. Goldoni and F. M. Peeters, Phys. Rev. B **53**, 4591 (1995).

- 
- [154] S. W. S. Apolinario, B. Partoens, and F. M. Peeters, *New Journal of Phys.* **9**, 283 (2007).
- [155] Y. G. Cornelissens, B. Partoens, and F. M. Peeters, *Physica E* **8**, 314 (2000).
- [156] J. A. Drocco, C. J. O. Reichhardt, C. Reichhardt, and B. Janko, *Phys. Rev. E* **68**, 060401 (2003).
- [157] H. Totsuji, T. Kishimoto, and C. Totsuji, *Phys. Rev. Lett.* **78**, 3113 (1997).
- [158] A. Rahman and J. P. Schiffer, *Phys. Rev. Lett.* **57**, 1133 (1986).
- [159] H. Totsuji and J.-L. Barrat, *Phys. Rev. Lett.* **60**, 2484 (1988).
- [160] J. P. Schiffer, *Phys. Rev. Lett.* **61**, 1843 (1988).
- [161] C. I. Ren and Y. Q. Ma, *Journal of American Chemical Society* **128**, 2733 (2006).
- [162] F. Yan and W. A. Goedel, *Chem. Mater.* **16**, 1622 (2004).
- [163] R. Messina, *J. Chem. Phys.* **117**, 11062 (2002).
- [164] J. Lekner, *Physica A* **176**, 485 (1991).
- [165] A. Bródka and A. Grzybowski, *Mol. Phys.* **100**, 1017 (2002).
- [166] M. Mazars, *Europhys. Lett.* **84**, 55002 (2008).
- [167] T. Chou and D. R. Nelson, *Phys. Rev. E* **48**, 4611 (1993).
- [168] B. Pansu, P. Pieranski, and P. Pieranski, *J. Physics (Paris)* **45**, 331 (1984).
- [169] S. Naser, P. Leiderer, and T. Palberg, *Prog. Colloid Polym. Sci.* **102**, 194 (1997).
- [170] M. Schmidt and H. Löwen, *Phys. Rev. Lett.* **76**, 4552 (1996).
- [171] V. N. Manoharan, T. Elsesser, and D. J. Pine, *Science* **301**, 483 (2003).
- [172] C. Alba-Simionesco *et al.*, *J. Phys.: Condens. Matter* **18**, R15 (2006).
- [173] H. Löwen, E. C. Oğuz, L. Assoud, and R. Messina, *Advances in Chemical Physics* **148**, 225 (2012).
- [174] H. Löwen, *J. Phys.: Condens. Matter* **13**, R412 (2001).
- [175] Scattering provides an alternative method in Fourier space, see e.g.: D. K. Satapathy *et al* *Europhys. Lett.* **87**, 34001 (2009).

- [176] Y. Peng *et al.*, Phys. Rev. Lett. **104**, 205703 (2010).
- [177] Y. Peng *et al.*, Phys. Rev. E **83**, 011404 (2011).
- [178] For a review, see: H. Löwen, Soft Matter **6**, 3133 (2010).
- [179] P. Pieranski, L. Strzelecki, and B. Pansu, Phys. Rev. Lett. **50**, 900 (1983).
- [180] M. Schmidt and H. Löwen, Phys. Rev. E **55**, 7228 (1997).
- [181] F. R. Manzano, E. Bonet, I. Rodriguez, and F. Meseguer, Soft Matter **5**, 4279 (2009).
- [182] H. B. Eral, F. Mugele, and D. H. G, Langmuir **27**, 12297 (2011).
- [183] E. C. Oğuz, R. Messina, and H. Löwen, EPL **94**, 28005 (2011).
- [184] M. Kahn, J.-J. Weis, and G. Kahl, J. Chem. Phys. **133**, 224504 (2010).
- [185] T. Kaneko, T. Mima, and K. Yasuoka, Chem. Phys. Lett. **490**, 165 (2010).
- [186] D. Deb *et al.*, J. Chem. Phys. **134**, 214706 (2011).
- [187] T. Curk *et al.*, Phys. Rev. E **85**, 021502 (2012).
- [188] G. Goldoni and F. M. Peeters, Phys. Rev. B **53**, 4591 (1996).
- [189] M. Evers, N. Garbow, D. Hessinger, and T. Palberg, Phys. Rev. E **57**, 6774 (1998).
- [190] E.g. by use of ImageJ (open source program currently available under <http://rsbweb.nih.gov/ij/>).
- [191] S. Patricio *et al.*, Langmuir **26**, 10842 (2010).
- [192] D. Hessinger, M. Evers, and T. Palberg, Phys. Rev. E **61**, 5493 (2000).
- [193] M. Medebach, L. Shapran, and T. Palberg, Colloids and Surfaces B: Biointerfaces **56**, 210 (2007).
- [194] D. R. Lide and H. P. R. Frederikse, *Handbook of Chemistry and Physics* (Elsevier, Amsterdam, 1994).
- [195] A. Reinmüller *et al.*, J. Chem. Phys. **136**, 164505 (2012).
- [196] M. Medebach *et al.*, J. Chem. Phys. **123**, 104903 (2005).
- [197] D. Andelman, in *Handbook of Biological Physics*, edited by R. Lipowsky and E. Sackmann (Elsevier, Amsterdam, 1995).

- [198] T. M. Squires and M. P. Brenner, Phys. Rev. Lett. **85**, 4976 (2000).
- [199] H. H. von Grünberg, L. Helden, P. Leiderer, and C. Bechinger, J. Chem. Phys. **114**, 10094 (2001).
- [200] D. H. van Winkle and C. A. Murray, Phys. Rev. A **34**, 562 (1986).
- [201] H. Löwen, J. N. Roux, and J. P. Hansen, J. Phys.: Condens. Matter **3**, 997 (1991).
- [202] Y. L. Wu, D. Derks, A. van Blaaderen, and A. Imhof, PNAS **106**, 10564 (2009).
- [203] L. T. Shereda, R. G. Larson, and M. J. Solomon, Phys. Rev. Lett. **105**, 228302 (2010).
- [204] E. Villanova-Vidal, T. Palberg, H.-J. Schöpe, and H. Löwen, Phil. Mag. **89**, 1695 (2009).
- [205] A. Stipp *et al.*, J. Phys.: Condens. Matter **16**, S3885 (2004).
- [206] K. Franzrahe *et al.*, J. Phys.: Condens. Matter **20**, 404218 (2008).
- [207] K. Franzrahe, P. Nielaba, and S. Sengupta, Phys. Rev. E **82**, 016112 (2010).
- [208] W. T. M. Irvine, V. Vitelli, and P. M. Chaikin, Nature **468**, 947 (2010).
- [209] T. C. Hales, Discrete Comput. Geom. **36**, 5 (2006).
- [210] J. D. Bernal, Nature **185**, 68 (1960).
- [211] F. H. Stillinger, E. A. DiMarzio, and R. L. Kornegay, J. Chem. Phys. **40**, 1564 (1964).
- [212] R. Zallen, *The Physics of Amorphous Solids* (Wiley, New York, 1983).
- [213] S. F. Edwards, *Granular Matter* (Springer-Verlag, New York, 1994).
- [214] W. B. Russel, D. A. Saville, and W. R. Schowalter, *Colloidal Dispersions* (Cambridge University Press, Cambridge, UK, 1989).
- [215] J. Liang and K. A. Dill, Biophys. J. **81**, 751 (2001).
- [216] P. K. Purohit, J. Kondev, and R. Phillips, Proc. Natl. Acad. Sci. USA **100**, 3173 (2003).
- [217] T. C. Hales, Ann. of Math. **162**, 1065 (2005).
- [218] For a recent review, see e.g. S. Torquato and F. H. Stillinger, Rev. Mod. Phys. **82**, 2633 (2010).

- [219] A. Donev, F. H. Stillinger, P. M. Chaikin, and S. Torquato, *Phys. Rev. Lett.* **92**, 255506 (2004).
- [220] S. Sacanna, L. Rossi, A. Wouterse, and A. P. Philipse, *J. Phys.: Cond. Matter* **19**, 376108 (2007).
- [221] P. F. Damasceno, M. Engel, and S. C. Glotzer, *Science* **337**, 453 (2012).
- [222] S. Torquato, *Nature* **460**, 876 (2009).
- [223] A. Haji-Akbari *et al.*, *Nature* **462**, 773 (2009).
- [224] J. de Graaf, R. van Roij, and M. Dijkstra, *Phys. Rev. Lett.* **107**, 155501 (2011).
- [225] A. Mughal, H. K. Chan, and D. Weaire, *Phys. Rev. Lett.* **106**, 115704 (2011).
- [226] R. P. A. Dullens, D. G. A. L. Aarts, W. K. Kegel, and H. N. W. Lekkerkerker, *Mol. Phys.* **103**, 3195 (2005).
- [227] Y. Peng *et al.*, *Phys. Rev. E* **83**, 011404 (2011).
- [228] H. Löwen, *Soft Matter* **7**, 8050 (2010).
- [229] H. Bock, K. E. Gubbins, and K. G. Ayappa, *J. Chem. Phys.* **122**, 094709 (2005).
- [230] A. V. Fiacco and G. P. McCormick, *Nonlinear Programming: Sequential Unconstrained Minimization Techniques* (Wiley, New York, 1968).
- [231] L. Assoud and R. Messina, *Phys. Rev. E* **83**, 036113 (2011).
- [232] K. Franzrahe and P. Nielaba, *Phys. Rev. E* **79**, 051505 (2009).
- [233] T. Zykova-Timan, J. Horbach, and K. Binder, *J. Chem. Phys.* **133**, 014705 (2010).
- [234] R. Najafabadi and S. Yip, *Scripta Metall.* **17**, 1199 (1983).
- [235] A. P. Bartlett, A. K. Agarwal, and A. Yethiraj, *Langmuir* **27**, 4313 (2011).
- [236] I. Cohen, T. G. Mason, and D. A. Weitz, *Phys. Rev. Lett.* **93**, 046001 (2004).
- [237] M. Abramowitz and I. A. Stegun, *Handbook of Mathematical Functions* (Dover Publications, Inc., New York, 1965).